Structure Determination, Mechanistic Study, and Safe Delivery of an Anti-Cancer Peptide

by

Jing Yu

B.S., Southeast University, 2010
M.S., Kanazawa University, 2013

AN ABSTRACT OF A DISSERTATION

submitted in partial fulfillment of the requirements for the degree

DOCTOR OF PHILOSOPHY

Department of Chemistry
College of Arts and Sciences

KANSAS STATE UNIVERSITY
Manhattan, Kansas

2018

Abstract

The therapeutic peptide sequence D-K_6L_9: LKLLKKLLKKLLKLL-NH_2 was developed for treating bacterial infections and solid tumors. It is effective against both conditions, because it is capable of targeting negatively charged surface domains due to its positive charge and the presence of hydrophobic units. Here, the peptide was modified with two extra amino acids (Serine and Alanine) at both, C and N terminals, resulting in SA-D-K_6L_9-AS. The sequence and structure of the modified peptide were determined by means of 2D ^1H-^1H -COSY, NOESY, and TOCSY-NMR spectroscopy. The 3D structure of the peptide in the solution phase was generated by CNS software utilizing data generated by NOE spectroscopy. This peptide was tested on the following mouse cancer cell lines: GL 26 (glioma), 4T1 (metastasizing breast cancer), NSC (neural stem cells), and pig monocytes. The LC50 values of the modified peptide were found to be 5- 10 times more active than of the original D-K_6L_9. To gain insight into its biochemical mode of action, SA-D-K_6L_9-AS tagged with a Rhodamine dye was incubated with GL 26 cancer cells. Sequential confocal imaging (every 30 seconds) revealed that the peptide interacts with cell membranes according to the carpet mechanism, and then becomes internalized into the cytoplasm in less than 5 min. and localizes in the mitochondria. This peptide is found to be toxic to neuronal stem cells and monocytes as well, showing the same mechanisms of interaction. To avoid the non-specific toxicity of the peptide for *in-vivo* applications, highly mesoporous silica nanoparticles (MSN) were synthesized, which served as a "container" for drug delivery. The peptide was then loaded into the MSN. MSN were further coated with a polysilazane as "gift wrap" (gatekeeper) after loading the peptide. This gatekeeper forms a shell that contains the peptide inside the MSN. While inside the MSN, the peptide shows no toxicity at 24 hours and subsequent slow release of its payload into the cytoplasm within 72 hours. This technology could

be very useful for in-vivo cancer therapy by means of targeted delivery to the cancer site with appropriate surface modification of MSNs.

Structure Determination, Mechanistic Study, and Safe Delivery of an Anti-Cancer Peptide

by

Jing Yu

B.S., Southeast University, 2010
M.S., Kanazawa University, 2013

A DISSERTATION

submitted in partial fulfillment of the requirements for the degree

DOCTOR OF PHILOSOPHY

Department of Chemistry
College of Arts and Sciences

KANSAS STATE UNIVERSITY
Manhattan, Kansas

2018

Approved by:

Major Professor
Prof. Dr. Stefan H. Bossmann

Copyright

Abstract

The therapeutic peptide sequence D-K_6L_9: LKLLKKLLKKLLKLL-NH_2 was developed for treating bacterial infections and solid tumors. It is effective against both conditions, because it is capable of targeting negatively charged surface domains due to its positive charge and the presence of hydrophobic units. Here, the peptide was modified with two extra amino acids (Serine and Alanine) at both, C and N terminals, resulting in SA-D-K_6L_9-AS. The sequence and structure of the modified peptide were determined by means of 2D ^1H-^1H -COSY, NOESY, and TOCSY-NMR spectroscopy. The 3D structure of the peptide in the solution phase was generated by CNS software utilizing data generated by NOE spectroscopy. This peptide was tested on the following mouse cancer cell lines: GL 26 (glioma), 4T1 (metastasizing breast cancer), NSC (neural stem cells), and pig monocytes. The LC50 values of the modified peptide were found to be 5- 10 times more active than of the original D-K_6L_9. To gain insight into its biochemical mode of action, SA-D-K_6L_9-AS tagged with a Rhodamine dye was incubated with GL 26 cancer cells. Sequential confocal imaging (every 30 seconds) revealed that the peptide interacts with cell membranes according to the carpet mechanism, and then becomes internalized into the cytoplasm in less than 5 min. and localizes in the mitochondria. This peptide is found to be toxic to neuronal stem cells and monocytes as well, showing the same mechanisms of interaction. To avoid the non-specific toxicity of the peptide for *in-vivo* applications, highly mesoporous silica nanoparticles (MSN) were synthesized, which served as a "container" for drug delivery. The peptide was then loaded into the MSN. MSN were further coated with a polysilazane as "gift wrap" (gatekeeper) after loading the peptide. This gatekeeper forms a shell that contains the peptide inside the MSN. While inside the MSN, the peptide shows no toxicity at 24 hours and subsequent slow release of its payload into the cytoplasm within 72 hours. This technology could

be very useful for in-vivo cancer therapy by means of targeted delivery to the cancer site with appropriate surface modification of MSNs.

Table of Contents

List of Figures

List of Tables

Acknowledgements

I would like to acknowledge my advisor Dr. Stefan H. Bossmann for all his support and help in the last five years. It is my great honor and luck to join his group. From him, I learned not only various techniques, but also how to research with critical thinking. Dr. Bossmann always encouraged me in every aspect and every improvement. He taught me “be yourself” and helped me build my confidence towards challenges. I will benefit from these all my life no matter what my career will be. Whenever I encountered any difficulty, I went to him because I know he is willing and able to give his full support to help me through those difficulties. Without him, I can never make this achievement. I would also like to thank his beautiful wife, Mrs. Katharine Bossmann. She is a very talented and elegant lady. She always supports and helps me whenever and whatever I need her. I appreciated that she helped review and correct my manuscripts numerous times, encouraged us to fight for our rights. Mrs. Bossmann and Dr. Bossmann treat our group members as families.

I would like to thank all my committee members, Dr. Deryl Troyer, Dr. Paul Smith, Dr. Emily McLaurin, and outside chair Dr. Jianfa Bai for their time and dedication during my Ph.D. study.

I also would like to thank all of my collaborators in the Troyer group, Dr. Tej B. Shrestha, and Marla Pyle for their help during my working in their lab. I would especially like to thank Dr. Tej B. Shrestha for his guidance and effort.

I also would like to thank Dr. Om Prakash and Dr. Alvaro Herrera, Department of Biochemistry and Molecular Biophysics at Kansas State University for their guidance and support concerning NMR structure elucidation, Dr. Ping Li and Kaimin Jia, Department of

Chemistry, for recording mass spectra, and Shu Jia, Department of Chemistry, for supporting my HPLC analysis.

I also would like to thank all the current and past group members in the Bossmann group, for their friendship and support. I would especially like to thank Dr. Hongwang Wang for sharing his knowledge and chemicals in the project of the MSN delivery system.

Finally, I would like to thank Kansas State University's Department of Chemistry for financial support during the last five years. I would also like to thank Dr. Leila Maurmann, Dr. Simon Sham, Mr. James Hodgson, Mr. Tobe Eggers, and Mr. Ron Jackson for their technical support.

Dedication

This work has been dedicated to my daughter, Mia, as she brings me endless happiness and courage to face the everyday challenge. I want to especially thank my beloved husband, Dr. Bo Wang, for everything he has done for me. I am extremely proud of him for everything that he has accomplished. I also want to thank my parents, Mr. Shudong Yu and Mrs. Congmei Sun, for everything they have taught me and have given me. They are the ones who always stand by my side and encourage me all the time. Sincere thanks to all my friends inside and outside of the United States for their support and friendship.

Chapter 1 - Introduction

1.1 The State-of-the-Art of Cancer Therapy in the United States

Cancer, also called malignant neoplasm, is currently the second most dangerous disease in the United States, with respect to human lives lost each year.[1-2] The overall cancer mortalities are rapidly rising, in spite of some recent treatment successes.[2] This is mainly due to the aging population in the US. It is expected that cancer mortalities will exceed the deaths because of heart disease, and become the leading cause of death in the next few years in America.[2] According to the National Cancer Institute (NCI), cancer is not just one type of disease, it is 'a collection of related diseases, which are associated with abnormally dividing and virtually immortal cells, that are capable of invading parts of the human body they did not originate in.[3]

For 2018, the estimated new cancer cases in United States are projected to be 1,735,350.[2] The estimated deaths are about 609,640. Among them, breast cancer, lung and bronchus cancer, and prostate cancer are the top three categories (Table 1.1). Lung and bronchus cancer cause approximately 25% of those deaths. And the following three types of cancers, colon cancer, pancreas cancer, and breast cancer lead to another one fourth of projected cancer mortalities (Table 1.2).[2]

Selected Cancer	Breast	Kidney & renal pelvis	Colon & Rectum	Uterine Corpus	Leukemia
Cases	268670	65340	140250	63230	60300
Percentage	15%	4%	8%	4%	3%
Selected Cancer	Lung & Bronchus	Melanoma of the Skin	Lymphoma	Prostate	Urinary Bladder
Cases	234030	91270	83180	164,690	81190

Percentage	14%	5%	5%	10%	5%

Table 1.1, Estimated new cases for selected cancers, 2018.

Selected Cancer	Brain & Other Nervous System	Breast	Colon	Leukemia	Liver & Intrahepatic Bile Duct
Deaths	16830	41400	50630	24370	30200
Percentage	2.8%	6.8%	8.3%	4.0%	5.0%
Selected Cancer	Lung & Bronchus	Lymphoma	Ovary	Pancreas	Prostate
Deaths	154050	20960	14070	44330	29430
Percentage	25.3%	3.4%	2.3%	7.3%	4.8%

Table 1.2, Estimated deaths for selected cancers, 2018.

The biochemical characteristics of cancer have been extensively studied. The latest updated hallmarks of cancer summarized by Douglas Hanahan and Robert A. Weinberg include six capabilities of cancer cells. They are "sustaining proliferative signaling, evading growth suppressors, resisting cell death, enabling replicative immortality, inducing angiogenesis, and activating invasion and metastasis."[4-5] A seventh characteristic is the dampening of the immune-response to cancer by means of defensive and stem cells that are recruited into the tumor microenvironment.[5]

Despite the horrendous number of deaths caused by cancer, advanced medical treatment can cure or control many types of tumors and metastases. It is well known that cancer can be divided in stages 0, I, II, III, IV[6], and the earlier the cancer is detected, the higher the probability of curing is.[7] Currently, surgery, chemotherapy, radiation therapy, immunotherapy, and targeted therapy are the standard of care in cancer treatment. Other methods are becoming available, such as hyperthermia[8], photodynamic/photothermal therapy[9-10], and immunotherapy[11].

The era of chemotherapy began in the early 1900's. Although surgery and radiation therapy were more common at that time, researchers found that combination of these methods with chemotherapy can increase patients' survival and delay the progression of terminal disease[12]. One of the particular advantages of chemotherapy is that it can treat micrometastases. Nowadays, more than half of cancer patients are treated by some forms of chemotherapy[3].

There are several types of chemotherapy drugs in clinical use. The majority of them are cytotoxic drugs, which can kill cancer cells or interfere with their reproduction[12]. However, chemotherapeutic drugs can act on healthy cells too, leading to many collateral effects. Therefore, improving the specificity of chemotherapy drugs and reducing their toxicity for healthy cells is of great importance.

1.2 The Cancer-Immunity Cycle[13-16]

One of the hallmarks of cancer is the accumulation of genetic alterations and the loss of normal cellular regulatory processes. These genetic alterations cause the expression of multiple antigens, which bind to major histocompatibility class I molecules (MHCI). These MHCI complexes on the surface of cancer cells can be, principally, recognized by CD8+ T cells (cytotoxic CD8+ T-lymphocytes). However, these events rarely result in an efficient immune response to cancer. Constant "immune editing", the permanent deletion of cancer cells expressing suitable T-cell targets, was recognized in 2002 as a mechanism of immune evasion by cancer cells.[17] However, it is important to recognize that factors in the tumor microenvironment can either activate or deactivate the T-cell response to tumors. From a biochemical standpoint, the immune response in cancer consists of a series of regulated events involving numerous cytokines/chemokines, signaling and receptor functions, as well as enzymatic activity (e.g. arginase).

My thesis is concerned with the first step of the Cancer-Immunity Cycle[16], the release of cancer cell neoantigens, which have to be captured by dendritic cells (DCs) for processing and subsequent antigen presentation to T cells. Without efficient mechanisms of necrotic cell killing, the concentration of neoantigens that are released, is too small to efficiently start the cancer immunity cycle. Necrotic cell death leads to inflammation, which can cause severe complications when treating tumors. However, the processes occurring during necrotic (= proinflammatory) cell death can play a crucial role in the generation of a T cell-mediated adaptive immune response to cancer.[18] Contrary to the groups of initiator (caspase-2, -8, -9, and -10) and effector caspases (caspases-3, -6, -7), which lead to apoptosis (programmed cell death), the group of caspases that are related to caspase-1 (caspases -1, -4, -5, -13, and -14) are mainly responsible for cytokine processing, leading to pro-inflammatory cell death, in which cell contents including potential neoantigens are released.[19] Therefore, therapeutic peptides causing necrosis are potentially superior to anticancer drugs that cause apoptosis, because they can facilitate an adaptive immune response to cancer.[18] It should be noted that during the last decades the focus of anticancer drug development was mainly on inducing apoptosis[20] to overcome cellular immortalization[21]. This paradigm has to be reversed to facilitate an effective immune response to cancer. Based on this discussion, my thesis research is centered on the peptide K_6L_9[22-26] that is known to cause necrotic cell death. My studies were designed to enhance the efficacy of K_6L_9 derivatives and to devise a method for safely delivering a K_6L_9 derivative to tumor tissue while minimizing collateral effects.

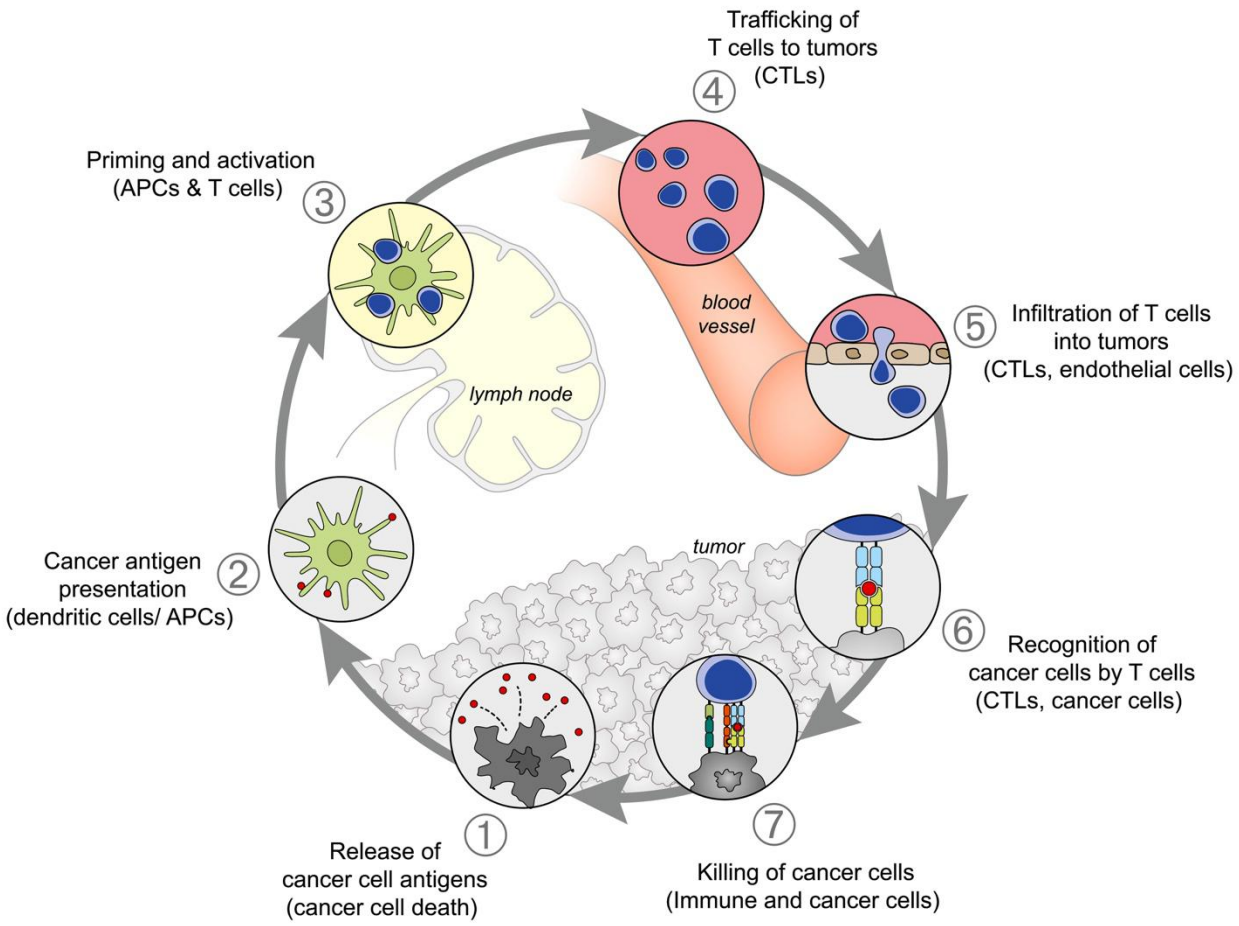

Figure 1.1, The Cancer-Immunity Cycle.[16]

"The generation of immunity to cancer is a cyclic process that can be self-propagating, leading to an accumulation of immune-stimulatory factors that in principle should amplify and broaden T cell responses. The cycle is also characterized by inhibitory factors that lead to immune regulatory feedback mechanisms, which can halt the development or limit the immunity. This cycle can be divided into seven major steps, starting with the release of antigens from the cancer cell and ending with the killing of cancer cells. Each step is described above, with the primary cell types involved and the anatomic location of the activity listed. Abbreviations are as follows: APCs, antigen presenting cells; CTLs, cytotoxic T lymphocytes."[16] Therapeutic agents that can cause necrotic cell death are required to start the cancer-immunity cycle.

1.3 The Evolution of the Oligopeptide K_6L_9

1.3.1 The therapeutic peptide K_6L_9 was originally developed as an antibiotic.

K_6L_9 (LKLLKKLLKKLLKLL-NH_2) is an amphipathic peptide sequence that is composed of six polar lysine and nine hydrophobic leucine units.[22] It was originally designed as

a peptide antibiotic to kill bacteria. The bacterial cell envelopes in both, gram-negative and gram-positive bacteria have complex multilayered architectures.[27] Both cell envelope structures contain long anionic polymers, called teichoic acids. Together with the phospholipids of the actual cell membranes, teichoic acids are mainly responsible to the negative surface charges of virtually all bacteria.[27] Therefore, antibiotic peptides feature positive charges, we all as hydrophobic segments that facilitate interaction with bacterial cell envelopes.

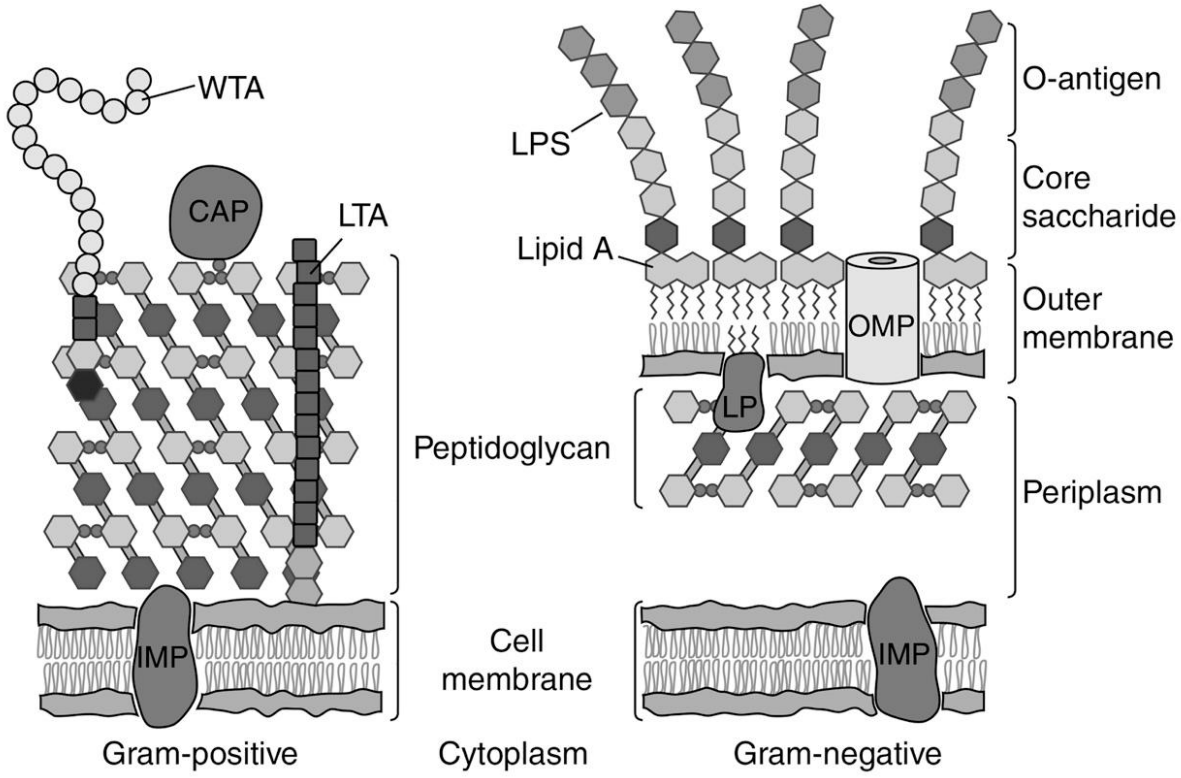

Figure 1.2, Depiction of Gram-positive and Gram-negative cell envelopes.[27]

"CAP, covalently attached protein; IMP, integral membrane protein; LP, lipoprotein; LPS, lipopolysaccharide; LTA, lipoteichoic acid; OMP, outer membrane protein; WTA, wall teichoic acid."[27]

Transmembrane potential depolarization experiments using K_6L_9 diastereomers, in which some of the L-amino acids were replaced by D-amino acids, showed that all investigated peptides were capable of killing bacteria by means of membrane perturbation. However, whereas

L-K_6L_9 was not virtually inactive in serum, because it was quickly hydrolyzed by Trypsin and Proteinase K, several K_6L_9 diastereomers were less of virtually not affected by proteolytic cleavage.[22] D-K_6L_9 (LK*L*LK*K*L*LK*KLL*K*LL-NH_2) was the best K_6L_9 diastereomer, based on its stability in the presence of Trypsin and Proteinase K, as well as on its activity against a panel of four gram-negative and four gram-positive bacteria in serum. D-K_6L_9 showed significant activity against *Pseudomonas aeruginosa* and Gentamicin-resistant *Acinetobacter Baumannii* in mice.[23] Y. Shai et al. observed that D-K_6L_9 depolarized the transmembrane potential of the bacteria, which occurred at the same time scale than the on-set of bactericidal action. Similar kinetics were observed on both, resistant and non-resistant bacteria.[23] Based on these findings they concluded that D-K_6L_9 mainly targets the bacterial plasma membrane and not particular bacterial targets.[23] This observation opened the door to using D-K_6L_9 against cancer cells.

1.3.2 The use of D-K_6L_9 to target the negative surfaces of cancer cells

Positively charged therapeutic peptides are able to target cancer cells, because, in contrast to healthy mammalian cells, they exhibit negative surface charges.[28-29] Two major reasons for the occurrence of negative surface charges of cancer cells are discussed in the literature: enrichment of phosphatidylserine in the outer membrane leaflet[28], and secretion of lactate anions because of the Warburg effect.[29-30] Eukaryotic cells are characterized by an symmetric distribution of phospholipids. Whereare phosphatidylcholine and sphingomyelin are predominately located within the outer membrane leaflet, phosphatidylserine and phosphatidylethanolamine are significantly enriched in the inner membrane leaflet. Eukaryotic cells have developed ATP-dependent lipid transporters to maintain this asymmetic distribution. Numerous physiological and especially pathological conditions are known, in which this asymmetry partially collapses. Tumor cells utilize the non-immunogenic properties of

phosphatidylserine, which is normally found at cell surfaces at the onset of apoptosis[28], to escape immune detection and to generate a local immunosuppresive environment. Furthermore, they excrete exosomes containing phosphatidylserine, which cause both a local and a systemic depression of the immune response to cancer.[28] Furthermore, phosphatidylserine levels increase in response to chemo- and radiotherapy.[28] The metabolism of cancer cells is characterized by elevated glycolysis.[29] It has been established that both, glucose uptake and lactate secretion are upregulated in a wide variety of cancer cell lines.[29] The enhanced secretion of lactate contributes to the negative surface charge on cancer cells, which enables to target them by using positively charged therapeutic peptides.

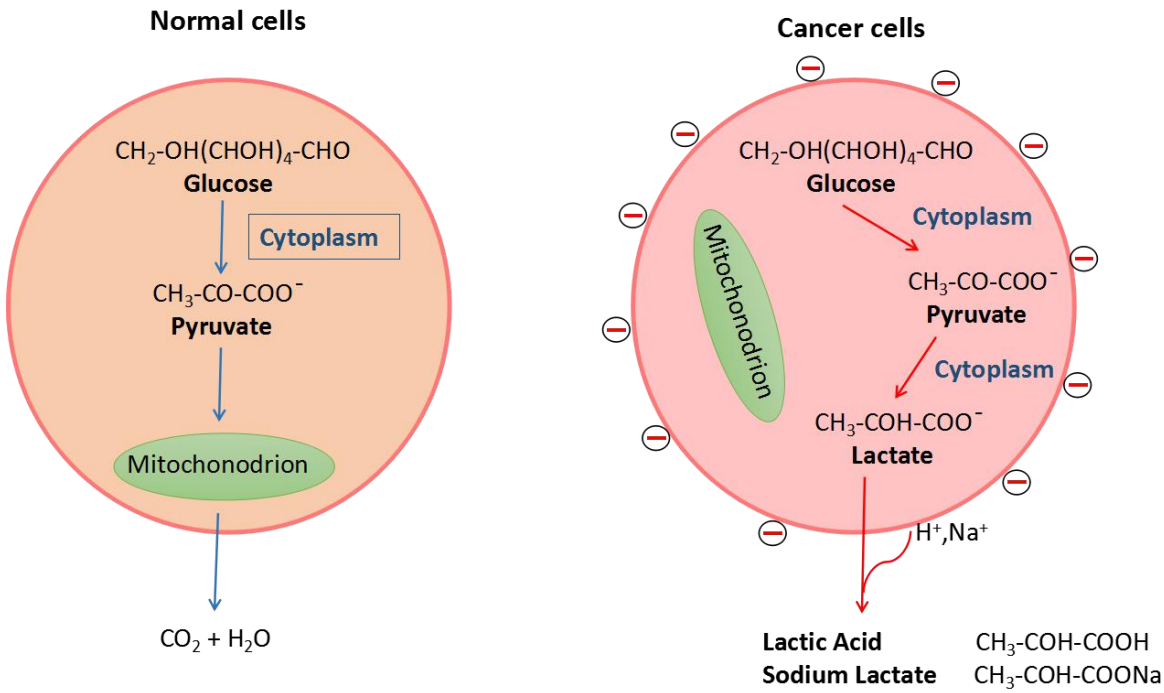

Figure 1.3, Schematic diagram showing secretion of lactate anions leading to a loss of cations from cancer cell surface and leaving behind the negative charges.[29]

(A) Glucose metabolism via glycolysis and oxidative phosphorylation in normal cells. (B) Glucose metabolism via highly elevated glycolysis and suppressed oxidative phosphorylation in cancer cells.[29]

Shai et al. were the first to establish the use of D-K_6L_9 against human androgen-independent and androgen-dependent prostate carcinoma cancer cell lines (CL1, 22RV1, and LNCaP).[24-25] These results were confirmed by means of *in-vivo* experiments utilizing a 22RV1 xenograft mouse model.[25] Whereas the first proof-of-concept experiments were performed by intratumoral injection of D-K_6L_9, later successful studies in pancreatic and breast xenograft models relied on systemic inoculation.[24] However, D-K_6L_9 showed significant systemic toxicity, because the therapeutic peptide sequence was unable to differentiate between tumor cells and apparently healthy cells, which caused severe complications.[24]

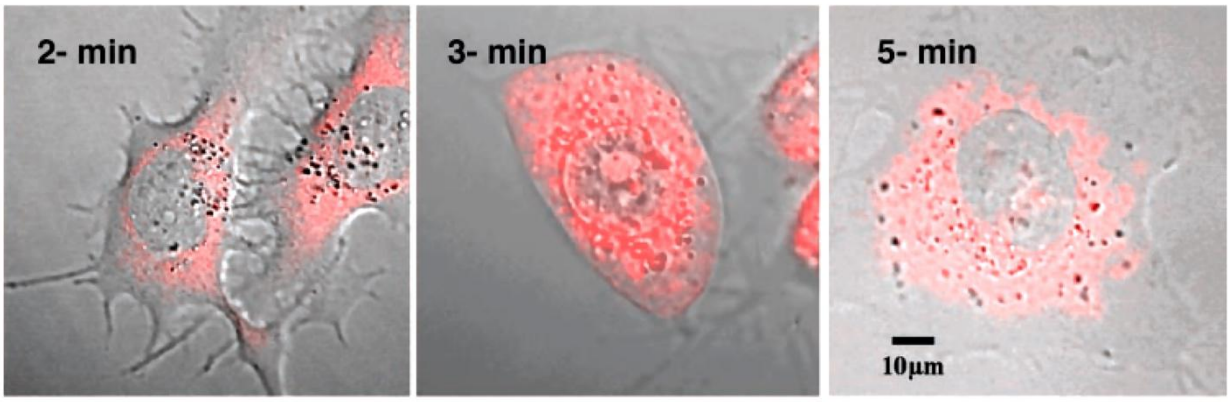

Figure 1.4, Confocal microscopy images of CL1 pancreatic cancer cells after 2 min., 3 min., and 5 min. of incubation with rhodamine-labeled LK*L*LK*K*L*LK*KLL*K*LL-NH_2.

Shai et al. have performed fluorescent confocal studies of D-K_6L_9 with CL1 pancreatic cancer cells.[25] It is clearly discernible from Figure 1.4 that D-K_6L_9 is targeting the cell membranes. According to the authors, evidence for targeting of other cell organelles could not be obtained from confocal laser scanning microscopy.[25] The authors have established a necrotic mechanism of cell death based on data from histopathology and cell permeability studies. D-K_6L_9 was able to depolarize the transmembrane potential and to release a cell encapsulated dye through induced ruptures in the phospholipid membrane. Furthermore, thresholds of D-K_6L_9 in the micromolar range were required for successful cell killing, depending on the cell type.[25]

1.3.3 Interactions of peptides with cell membranes

The current literature discusses four principal mechanisms of bilayer membrane disruption by peptides that are depicted in Figure 1.5.[31] Upon reaching the required threshold concentration, the peptides either insert into the bilayer membrane structure and form either barrel stave pores[32], toroidal pores[33], or disordered toroidal pores[34].

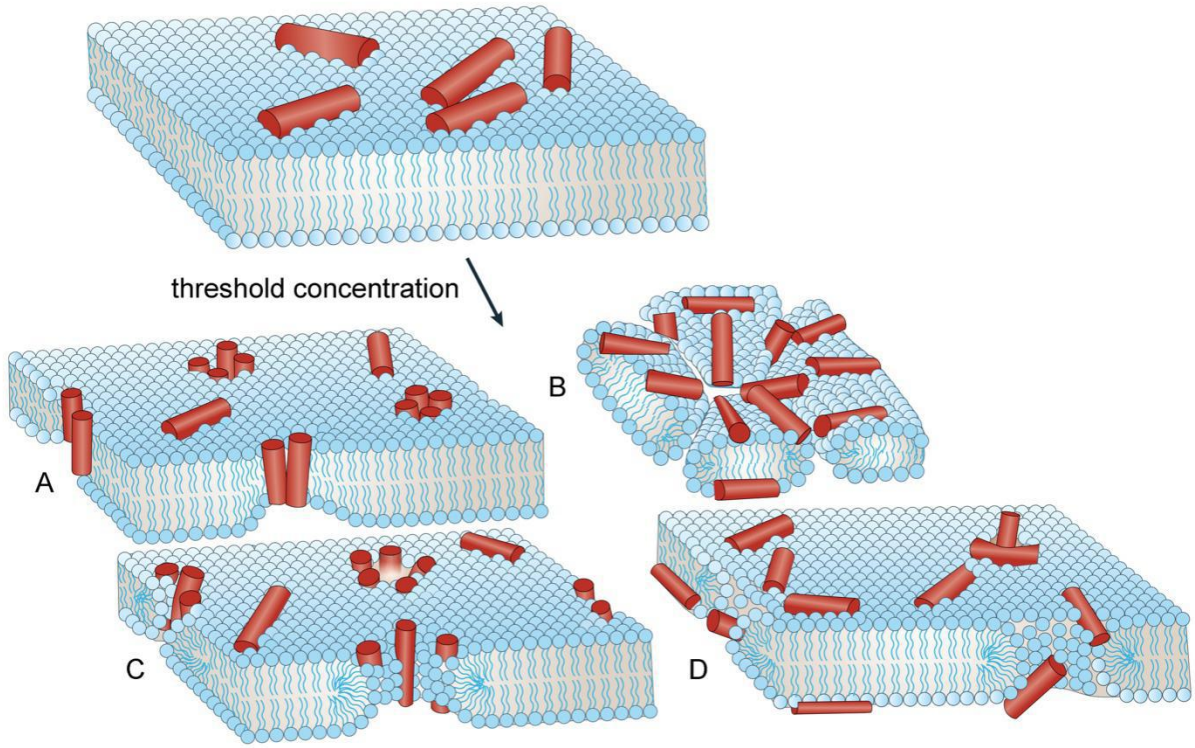

Figure 1.5, Proposed mechanisms of peptide-mediated membrane disruption. [31]

"A: Barrel-stave pore. [32] Peptides insert perpendicularly in the bilayer, associate and form a pore. B: Carpet mechanism[35]. Peptides adsorb parallel to the bilayer and, after reaching sufficient coverage, produce a detergent-like effect that disintegrates the membrane. C: Toroidal pore[33]. Peptides insert perpendicularly in the bilayer, but instead of packing parallel to the phospholipid chains, induce a local membrane curvature. D: Disordered toroidal pore[34]. A recent modification to the toroidal pore proposes that less-rigid peptide conformations and orientations are formed; the pore lumen is lined by the phospholipid head groups."

For barrel stave and toroidal pores, it is required that the lengths of the peptide sequence after assuming its 3D structure is long enough to span the entire diameter of the bilayer membrane.[31] If that is not possible, disordered toroidal pores can be formed.[34] One important

alternative to pore-forming mechanisms is the carpet mechanism[35], in which the therapeutic peptides adsorb parallel to the bilayer. Upon reaching the threshold concentration, micellization of membrane components and entire membrane sections can be observed. These processes can disintegrate bilayer membranes very efficiently.[31]

1.4 Thesis Research

In my thesis research, I have designed an improved therapeutic peptide sequence SA-D-K_6L_9-AS, capable of killing cells with greater efficacy, as well as a novel drug delivery system, which has the potential of affecting cancer cells without major collateral effects on normal tissue. A nanoscopic drug carrier material, mesoporous silica nanoparticles (MSN)[36-37], was employed, together with a silazane polymer layer of variable thickness to facilitate timed release of SA-D-K_6L_9-AS. This polymeric gate-keeper was designed for using neural stem cells as carriers for the nanomaterials[38], because these cells will slowly biocorrode the silazane layer and undergo cell death once they have arrived in the tumor region. This approach enables the use of these cancer homing cells to deliver the cytotoxic payload to the tumor, because neural stem cells follow cytokine gradients and actively migrate into tumors and metastases[38].

Chapter 2 - Design, Synthesis, Characterization and Cell-Tests of the Anticancer Peptide SA-D-K_6L_9-AS

The research summarized in this chapter was conducted in collaboration with Prof. Dr. Om Prakash and Dr. Alvaro Herrera (Department of Biochemistry and Molecular Biophysics), who recorded the 2D-NMR spectra of SA-D-K_6L_9-AS, as well as Dr. Tej. B. Shrestha (Department of Anatomy & Physiology), who performed the laser scanning confocal microscopy experiments together with me. I would like to sincerely thank all of my collaborators.

2.1 Background

The therapeutic peptide sequence D-K_6L_9: LK*L*LK*K*L*LK*KLL*K*LL-NH_2 was developed by Shai et al. for treating bacterial infections[22-23] and solid tumors.[24-25] D-K_6L_9 is effective against both diseases, because it is capable of targeting negatively charged surface domains because of its positive charge. Molecular modelling indicated that D-K_6L_9 assumes a somewhat distorted helical structure. Laser scanning confocal microscopy and transmembrane potential measurements have provided evidence that D-K_6L_9 kills cancer cells by means of membrane disintegration once a threshold concentration in the micromolar range is reached.[25] Histopathology studies have provided further evidence that D-K_6L_9 causes necrotic cell death.[25]

Recent findings have established that a necrotic killing mode is advantageous with respect to effectively presenting cancer neoantigens to dendritic cells, which is required to develop an effective immune response to cancer.[4, 16, 18]. The disadvantages that are reported for D-K_6L_9 are that it requires concentrations above 10 micromoles per liter to be effective against human cancer cell lines[25] and that it showed significant collateral toxicity in *in-vivo* experiments.[23-25]

We have adopted the strategy of adding the two amino acids serine and alanine to each end of D-K_6L_9, resulting in SA-D-K_6L_9-AS (SALK*l*LK*k*L*lk*KLL*k*LLAS) mainly for three reasons: 1) The addition of the water-soluble amino acid serine to both ends of the peptide sequence facilitates enhanced solubility in aqueous buffers, possible resulting in the ability to target cell organelles. The use of highly water-soluble serine does not interfere with the six positive charges of SA-D-K_6L_9-AS (pI (pH of zero charge) = 10.70[39]) in aqueous buffers, which are required for interaction with cancer cell membranes.[28-29] The availability of multiple targets often enhances the toxicity of therapeutic peptide sequences.[31] According to this paradigm, SA-D-K_6L_9-AS should be more toxic than D-K_6L_9. 2) Molecular modelling (see Figure 2.1) indicates that SA-D-K_6L_9-AS retains the alpha-helical structure, which is anticipated for L-K_6L_9, albeit it is distorted in both, D-K_6L_9 and SA-D-K_6L_9-AS according to molecular simulation.[40] The strategic advantage of adding SA and AS to D-K_6L_9 is that the NMR-elucidation of the 3D structure of SA-D-K_6L_9-AS becomes attainable. This has been impossible for all K_6L_9 derivatives, because of the high abundance of K and L, resulting in the inability to distinguish between backbone and sidechain signals from the various lysine and leucine sites within the oligopeptide. 3) The underlying paradigm of adding two serine and two alanine units to D-K_6L_9 is to enhance, not to decrease its cytotoxicity. Previous studies have indicated that there is only a limit potential of decreasing the systemic toxicity of D-K_6L_9. Shai et al. have exchanged either three or six lysines with histidines. This approach resulted in therapeutic peptides with decreased pI's (10.30 for D-$H_3K_3L_9$ and 6.99 for D-H_6L_9)[26], which showed decreased killing efficacies towards cancer cells, as well as somewhat decreased systemic toxicities. Especially D-H_6L_9 is only protonated during endosomal uptake and, therefore, pH-activatable. However, endosomal uptake occurs in cancer cells and healthy cells alike, thus limiting the targeting efficacy of tumors *in-vivo*. Both

peptides performed well in xenograft models.[26] However, systemic administration in fully immunocapable animal models is most likely not an option, because innate-like lytic peptides potentially could overstimulate the immune system, resulting in systemic inflammation and inflammatory diseases.[41] A safer alternative, which will be pursued here, is to develop a "container" for SA-D-K_6L_9-AS that can be taken up by either defensive cells or stem cells, which can be used as "cargo ships" for transporting the therapeutic peptide sequences to the cancer sites. Both cell types are known to follow cytokine/chemokine gradients and to actively migrate to tumors where they associate with either the tumor or the stromal tissue.[38, 42-44] A further advantage of this approach is that the total amount of SA-D-K_6L_9-AS can be significantly minimized, compared to systemic injection, due to better targeting efficacy.

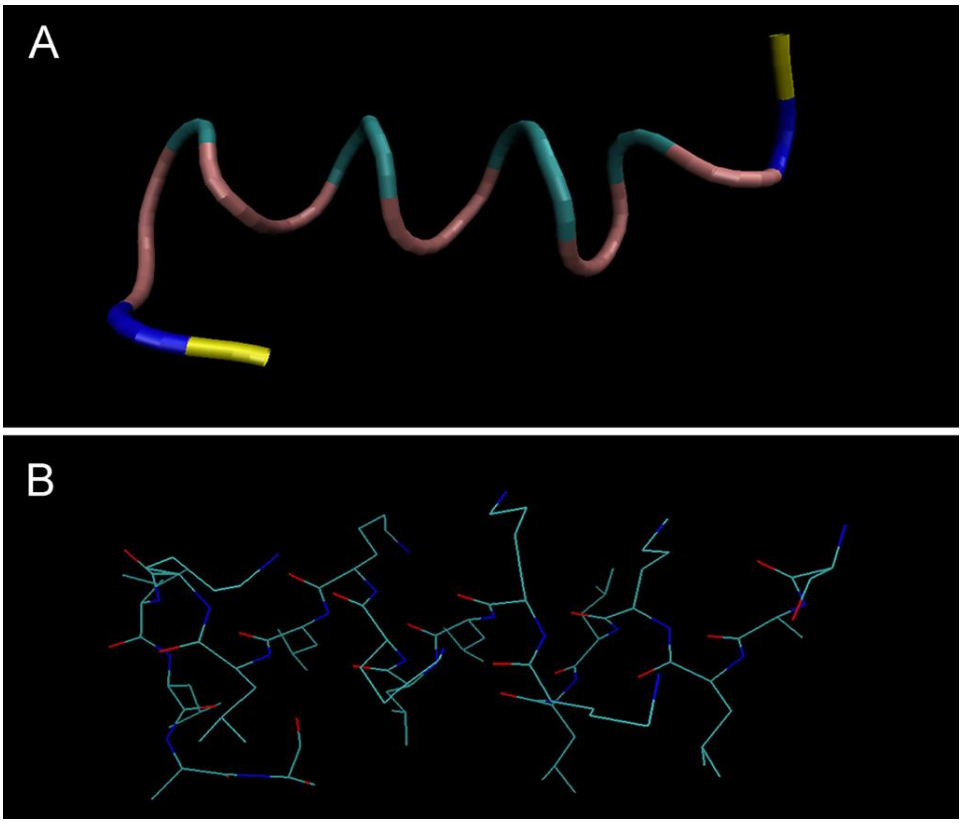

Figure 2.1 Folded SA-D-K_6L_9-AS structure, as calculated by PEPstrMOD.

A: tube mode; B: 3D structure showing carbon, nitrogen, and oxygen atoms (hydrogens are omitted).

2.2 Materials and Methods

2.2.1 Synthesis and characterization of peptides

SA-D-K_6L_9-AS was synthesized by standard Fmoc-based solid phase synthesis.[44-45] 0.77mmol (1.003g) of H-Ser(tBu)-2-ClTrt-Resin was allowed to swell in DCM for 20 min. in a peptide synthesis tube. After washing with DMF, a mixture of 3 equiv. HBTU and Fmoc-Ala-OH in 8.0ml of DIEA:DMF (1:23) was added to the tube and allowed to swirl at RT for 30 min. This reaction was repeated for 30 min to optimize the coupling yield. The resin was then treated with 20% piperidine in DMF for 1 min., and again swirled in 8.0 ml of new 20% piperidine for 10min to remove the Fmoc protection group. This cycle of amino acid coupling and subsequent Fmoc deprotection was repeated until the whole sequence was completed. Yield: 2.8g of yellow dry resin.

1.7g (0.468mmol) of dry resin was swelled in DCM. 8.0ml of a mixture of 95% TFA, 2.5% TIPS, and 2.5% of DI water was reacted with the resin for 3h. Then, the solution was filtered into 25ml of cold (0^{o}C) diethyl ether. A white peptide precipitate was formed, which was collected and then washed 3 times with diethyl ether. The crude product was then dissolved in 5.0 ml of DI water and lyophilized. Yield: 639 mg (0.301mmol) of white powder, 64%.

D-K_6L_9 was synthesized in the same way starting with H-Leu-2-ClTrt-Resin. Yield: 439mg (0.243mmol) white powder, 82.9%.

Rhodamine B labeled peptides were prepared by adding 3 eqv. Rhodamine B and HBTU in DIEA:DMF (1:23) after the last amino acid coupled.

Peptides were purified with HPLC and characterized by TOF MS ES+ (employing a Waters G2-XS QTof mass spectrometer, which is available in the group of Dr. Ping Li in the Chemistry Department at Kansas State).

2.2.2 HPLC analysis and purification

Both, peptide analysis and purification was performed by means of HPLC (Ultimate 3000, Thermo scientific).

Peptide analysis: The crude peptides were dissolved in distilled water in a concentration of 2.0 mg/mL, respectively. 20 µl of these solutions were filtered using 0.2 µM nylon filters and then injected into the HPLC column (Thermo Acclaim^{TM} 300, C18, 3µm, 2.1 x 150mm). The flow rate was maintained at 0.30 mL/min using a binary mixture. A: water containing 0.10% TFA, B: acetonitrile with 0.10% TFA. Gradient: 1-16min: 20% - 80% B, 16-20min: 80% B. Figures 2.3, 2.4, and 2.5 show the HPL chromatograms of the therapeutic peptides before and after HPLC purification.

Peptide purification: The crude peptides were dissolved in distilled water in a concentration of 20.0 mg/mL, respectively. 100 µl of these solutions were filtered using 0.2 µM nylon filters and then injected into the HPLC column (Phenomenex Kinetex 5u XB-C18, 250 x 21.1mm). The flow rate was maintained at 8 mL/min using 32% acetonitrile in water with 0.10% TFA.

2.2.3 Cell Cultures and MTT Assay

GL26 cells[46] were cultured in a T-25 flask in RPMI medium which contains 10% FBS. After the flask reaches about 80% confluency, cells were lifted with 0.1% trypsin then re-plated on a 96-well plate with a density of 10,000/cm^2 and cultured at 37℃ overnight in a cell culture incubator.

4T1 cells were maintained in the same way. A 0.25% trypsin solution was used to digest 4T1 cells for re-plating.

C17.2 neural progenitor cells (NPCs)[38] were a gift from Dr. V. Ourednik (Iowa State University) to Dr. Deryl L. Troyer, DVM (Kansas State University, Anatomy & Physiology). NPCs were originally developed by Dr. Evan Snyder.[47] These cells were maintained in DMEM supplemented with 10% FBS (Sigma-Aldrich), 5% horse serum (Invitrogen), 1% glutamine (Invitrogen), and 1% penicillin/streptomycin (Invitrogen).

Pig Monocytes, which were originally developed by Dr. Tej B. Shrestha, were cultured in RPMI medium with 10% FBS. Cells were lifted with scraper instead of trypsin, then re-plate on a 96-well plate for MTT assay.

2.2.4 MTT Assays

The cytotoxicity of D-K_6L_9 and SA-D-K_6L_9-AS was assessed by utilizing the MTT assay[48]: D-K_6L_9 and SA-D-K_6L_9-AS were diluted in 10% FBS containing RPMI medium to give a series concentration of 0, 0.05, 0.1, 0.2, 0.4, 0.6, 0.8, 1, 2, 5, 10, 20 μM and loaded to the cells in 4 replications. After 24h incubation at 37℃, 10 μl of MTT solution was added to each well. Then 100 μl of the 10% SDS in 0.01M HCl was added after another 4h. The plate was then placed in the incubator at 37℃ overnight. The absorbance was read by plate reader at a wavelength interval of 550nm and 690nm.

4T1, NSC, and pig monocyte cells were used for the MTT assay in a similar way. For NSC cells, NSC medium was used instead of RPMI. Sample concentration was tested up to 100μM (0, 0.1, 0.2, 0.5, 1, 2, 5, 10, 15, 20, 50, 100 μM).

Data was processed by Graphpad Prism 5.0.[49]

2.2.5 2D NMR study

Purified and lyophilized SA-D-K_6L_9-AS peptide (2.5mg) was dissolved in 500uL DMSO-d6. 2D ^{1}H-^{1}H-COSY, NOESY, and TOCSY spectra were obtained using the Varian System 500 MHz NMR spectrometer located in the Department of Biochemistry & Molecular Biophysics at Kansas State University. Peak assignments were obtained with Sparky 3.114.[50] The resulting 3D structure was resolved with the software package CNS 1.2[51] and processed with VMD 1.9.3.[52]

Three two-dimensional pulse sequences were used: COSY, TOCSY, and NOESY.[53]

COSY: Correlation Spectroscopy

^{1}H-^{1}H-COSY is one of the simplest and most useful 2D NMR homonuclear correlation experiments. Cross-peaks in a COSY spectrum arise from pairs of protons that experience scalar coupling (J-coupling). In a typical COSY spectrum, J-coupling that features an r^{-3} dependence (r = distance between coupling nuclei), can be observed between geminal or vicinal protons with coupling constants in the range of 3 to 15Hz. Long range couplings are rarely observed.

TOCSY: Total Correlation Spectroscopy

TOCSY spectra display cross-peaks from all protons that are located within a J-coupling network (spin system) by transferring coherence from proton to proton by means of J-coupling. TOCSY spectra enable the identification of individual amino acids in a peptide sequence.

NOESY: Nuclear Overhauser Effect Spectroscopy

NOESY spectra feature cross-peaks that are caused by dipolar cross-relaxation between nuclei in a close spatial relationship. NOE processes are characterized by a r^{-6} dependence. Therefore, they only appear for coupling protons that are less than 0.5 nm apart. Since NOE only

depends on the distance between coupling protons, it is extremely useful for determining the 3D structures of peptide sequences.

2.2.6 Confocal Imaging

Laser confocal microscopy of live and fixed cells was performed in the Confocal Microscopy and Microfluorometry Core in the Department of Anatomy & Physiology at Kansas State University. The confocal microscope, Carl Zeiss LSM 880, consists of an inverted microscope outfitted with five objectives, 2.5x, 10x, 20x, 40x (1.3 NA Oil) and 40x (1.2 NA (Water), six lasers, 405 (blue), 458 (blue), 488 (cyan), 514 (green), 561 (green) and 633 nm (red), three fluorescence emission detectors and one transmission detector.

GL26 cells and pig monocyte cells were plated in glass bottom microwell dishes with 8,000/cm^2, separately. Cells were washed with PBS after overnight incubation. 5 M Rhodamine-B labeled peptide SA-D-K_6L_9-SA was dissolved in RPMI (with 10% FBS) medium. The solution was added to cells and incubated at 37°C.

After 20min incubation, the solution was removed and cells were washed with PBS. 2.0mL of cell formalin solution (4% formaldehyde) was added to the dish and kept for 10 min. Then cells were washed again with PBS and stained with 1% Hoechst 33342 solution[54] (maxima: λ_{ex} = 350 nm, λ_{em} = 461 nm).

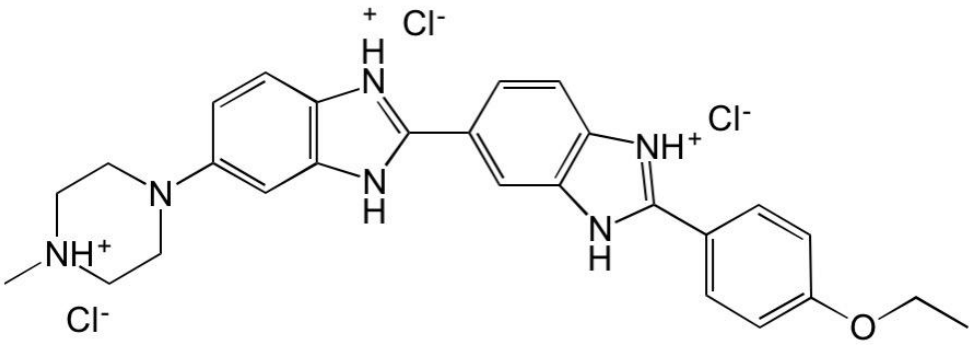

Figure 2.2, Chemical structure of Hoechst 33342

For live confocal imaging, GL26 cells and pig monocyte cells were prepared in the same way as above. After overnight incubation, 3μM of Rhodamine B labeled S2 in medium was added after removing the old one.

2.3 Results and Discussion

2.3.1 HPLC characterization of the peptides

Before the efficacies of the peptides D-K_6L_9[22-25] and SA-D-K_6L_9-AS, which was newly designed in my thesis research, could be compared *in-vitro*, the purity of both peptide sequences was determined by analytical HPLC. In Figure 2.3, the HPL chromatogram of D-K_6L_9 is shown. From the UV-absorbance of D-K_6L_9 at = 205 nm a purity of 76 ± 2% after synthesis was estimated. As shown in Figure 2.4, the purity of SA-D-K_6L_9-AS after synthesis was 72 ± 2%. After preparative HPCL purification, the purity of both peptide sequences was virtually 100 % (Figure 2.5). It is noteworthy that the retention time of SA-D-K_6L_9-AS (t = 8.52 min.) is slightly shorter than of D-K_6L_9 (9.03 min.). Both, D-K_6L_9 and SA-D-K_6L_9-AS have a pI = 10.70)[39]) in aqueous buffers. However, the influence of the organic solvent acetonitrile on the peptides' 3D structures cannot be predicted. Therefore, we were not able to rationalize this empirical data.

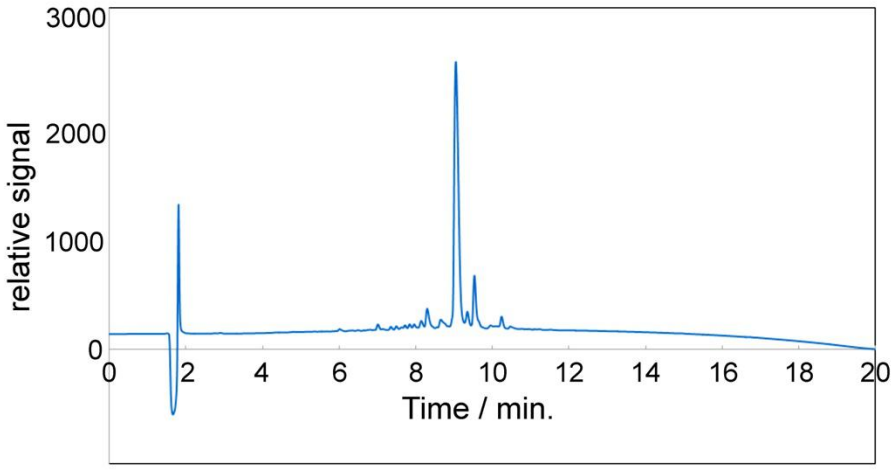

Figure 2.3, HPL chromatogram of D-K_6L_9 before purification.

Flow rate: 0.30 mL/min. A: water with 0.1% TFA, B: acetonitrile with 0.1% TFA, 1-16 min.: 20% - 80% B, 16-20 min.: 80% B. UV-detection wavelength = 205 nm.

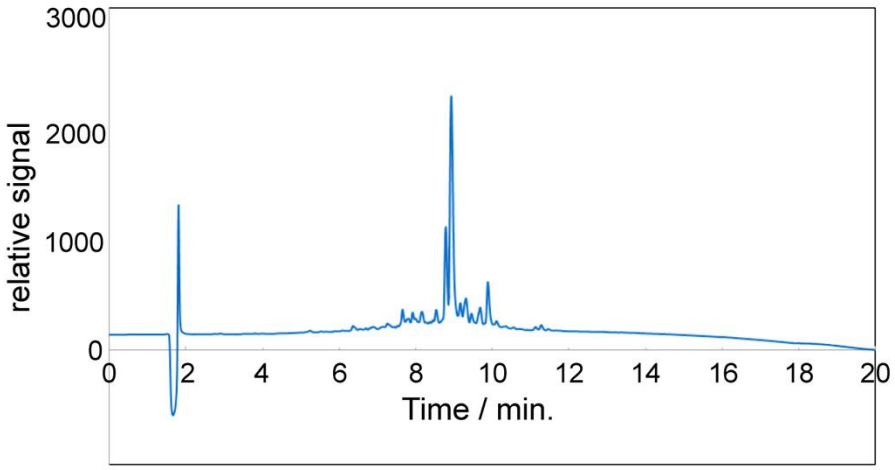

Figure 2.4, HPL chromatogram of SA-D-K_6L_9-AS before purification.

Flow rate: 0.30 mL/min. A: water with 0.1% TFA, B: acetonitrile with 0.1% TFA, 1-16 min.: 20% - 80% B, 16-20 min.: 80% B. UV-detection wavelength = 205 nm.

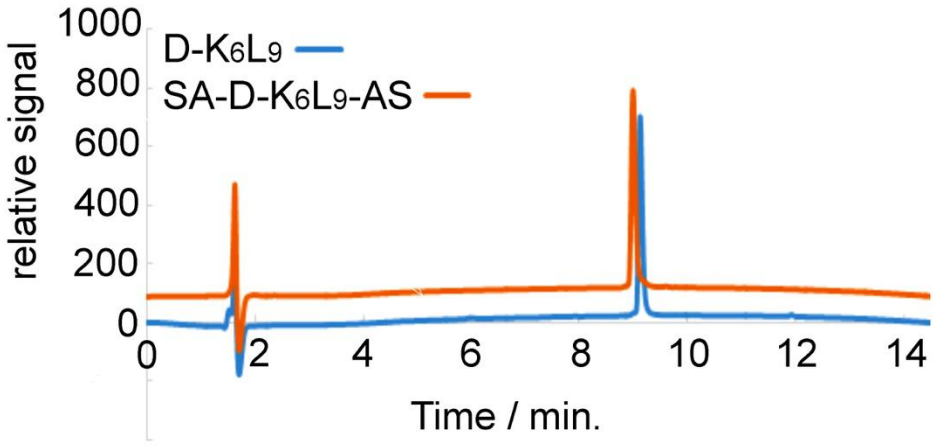

Figure 2.5, HPL chromatograms of D-K_6L_9 (blue) SA-D-K_6L_9-AS (orange) after purification.

Flow rate: 0.30 mL/min. A: water with 0.1% TFA, B: acetonitrile with 0.1% TFA, 1-16 min.: 20% - 80% B, 16-20 min.: 80% B. UV-detection wavelength = 205 nm.

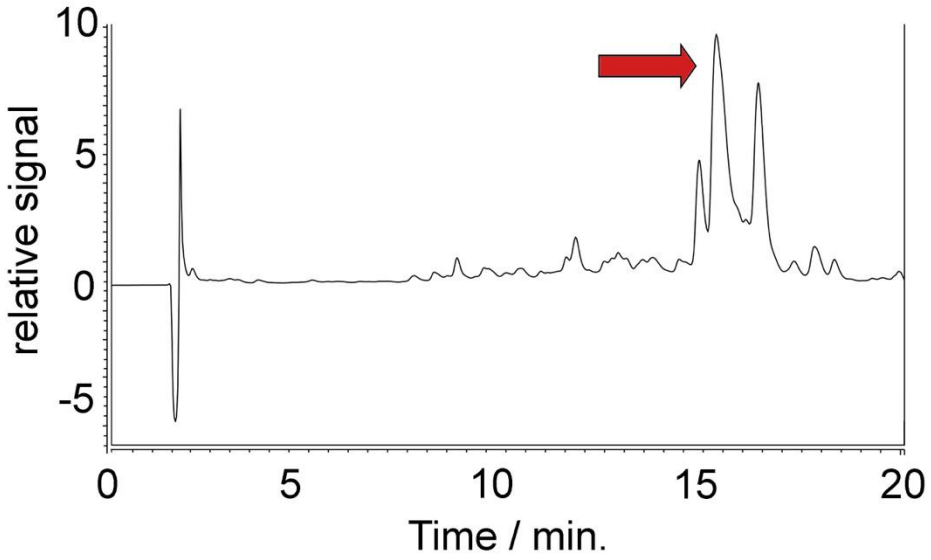

Figure 2.6, HPL chromatogram of Thodamine-B-labeled-SA-D-K_6L_9-AS after purification.

Flow rate: 0.30 mL/min. A: water with 0.1% TFA, B: acetonitrile with 0.1% TFA, 1-16 min.: 20% - 80% B, 16-20 min.: 80% B. UV-detection wavelength = 546 nm. The main fraction is marked with a red arrow.

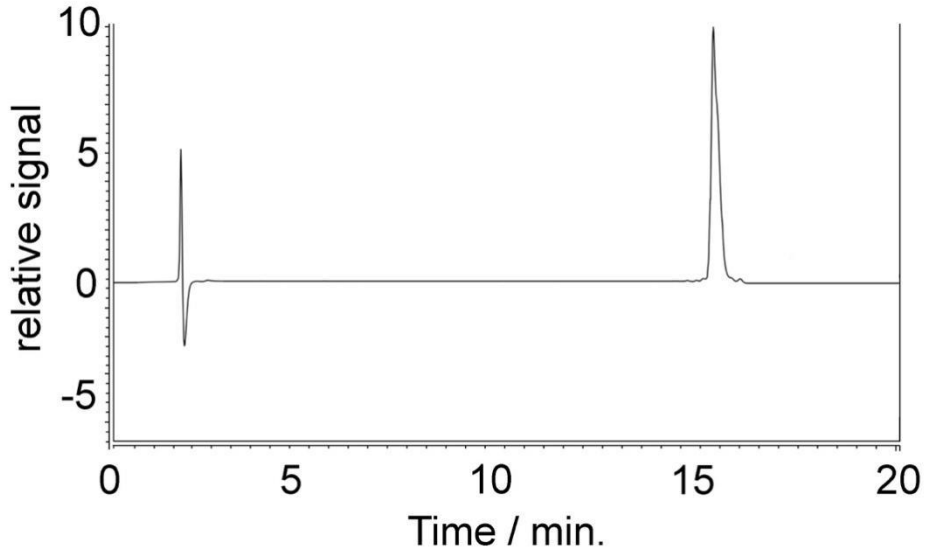

Figure 2.7, HPL chromatogram of Rhodamine-B-labeled-SA-D-K_6L_9-AS after purification.

Flow rate: 0.30 mL/min. A: water with 0.1% TFA, B: acetonitrile with 0.1% TFA, 1-16 min.: 20% - 80% B, 16-20 min.: 80% B. UV-detection wavelength = 546 nm.

2.3.2 Characterization of the Peptides D-K_6L_9 and SA-D-K_6L_9-AS by means of HRMS

High-resolution mass spectrometry (HRMS) of the HPCL-purified peptides was recorded using a Waters G2-XS QTof mass spectrometer. Both peptides were dissolved in DI water. In agreement with previous findings, both D-K_6L_9 and SA-D-K_6L_9-AS show several major fragmentation peaks. For D-K_6L_9 the M+ peak occurred at 1805.4265 m/z, which is in agreement with the calculated mass for D-K_6L_9. For SA-D-K_6L_9-AS the M+ peak is found at 2121.5251 m/z, which is again in agreement with the prediction for this peptide sequence. It is our conclusion from these data that the chemical compositions of both D-K_6L_9 and SA-D-K_6L_9-AS was confirmed.

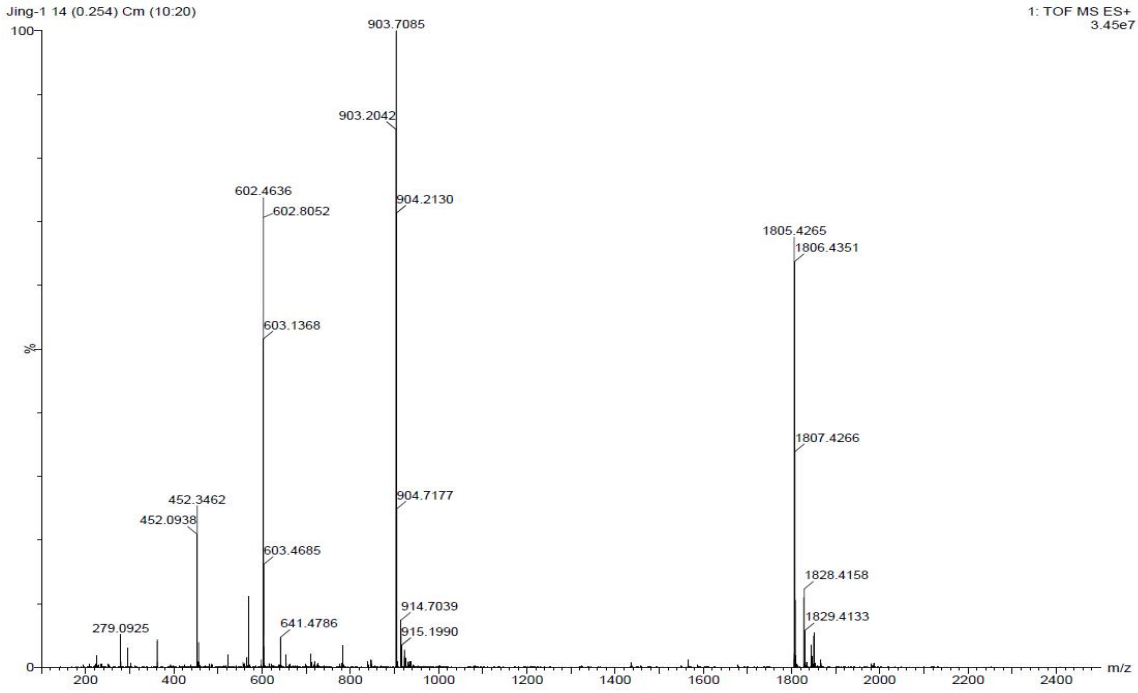

Figure 2.8, High-resolution mass spectrum of D-K_6L_9.
The molecular weight of D-K_6L_9 is 1805 m/z.

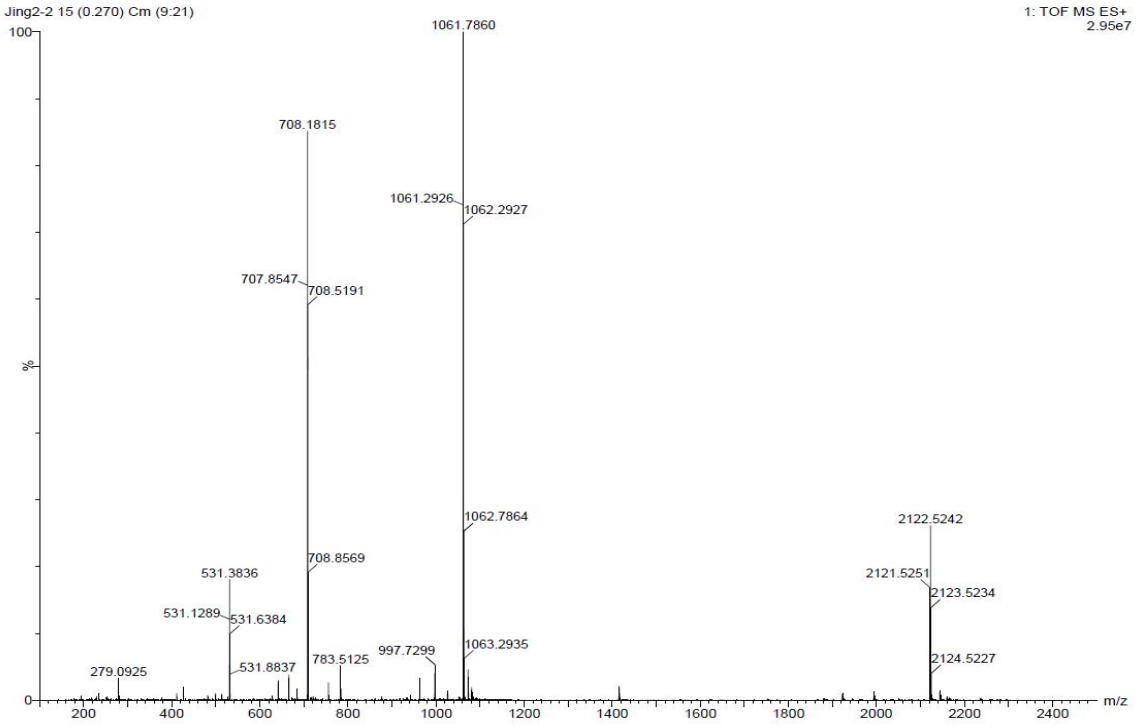

Figure 2.9, High-resolution mass spectrum of SA-D-K_6L_9-AS.

The molecular weight of SA-D-K_6L_9-AS is 2121 m/z.

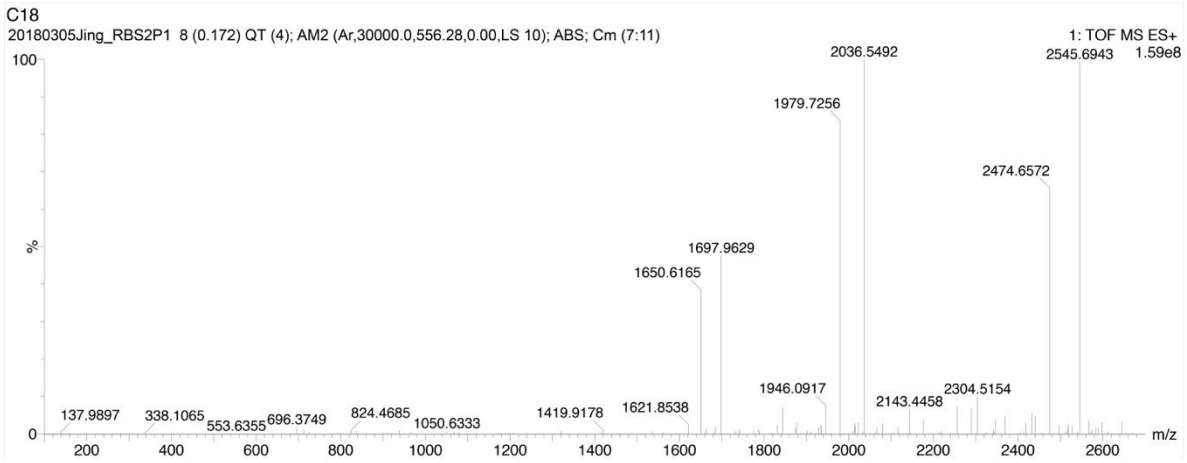

Figure 2.10, High-resolution mass spectrum of Rhodamine B-labeled SA-D-K_6L_9-AS.

The molecular weight of SA-D-K_6L_9-AS is 2582 m/z. The peak at 2545.69 m/z is indicative of Rhodamine B-labeled SA-D-K_6L_9-AS minus a chlorine atom.

2.3.3 MTT Assay[48]

The cell viability of 4 different cell lines was determined by cell MTT assay. GL26 was tested up to 20 μM, and the other three cell lines were measured up to 100 μM of peptide sequence concentration. As Figures 2.11-2.14 and the Medial Lethal Doses (LC_{50})[55] that are summarized in Table 2.1 indicate, both peptides exhibit cytotoxicity against all cell lines that were investigated. Among all tested cell lines, SA-D-K_6L_9-AS had a significantly higher killing efficacy than D-K_6L_9. SA-D-K_6L_9-AS is 8 times more effective on the murine glioma cell line GL26 when compared to D-K_6L_9, whereas SA-D-K_6L_9-AS is only 5.50 times more effective than D-K_6L_9 for pig monocytes, 3.39 times for 4T1 cells (murine metastasizing breast cancer), and 2.47 times for NSCs (murine neural stem cells). These findings clearly indicate that the targeting efficacy of SA-D-K_6L_9-AS towards cancer cell lines vs. non-cancerous cells lines is somewhat improved in comparison to D-K_6L_9. However, this won't be sufficient for safely using SA-D-K_6L_9-AS *in-vivo* without designing a suitable delivery system.

	D-K_6L_9	SA-D-K_6L_9-AS
GL26	14.18^{*} ($R^2 = 0.9104$)	1.707^{**} ($R^2 = 0.9634$)
4T1	10.14^{***} ($R^2 = 0.9333$)	2.987^{**} ($R^2 = 0.9896$)
NSC	6.621^{***} ($R^2 = 0.9688$)	2.679^{**} ($R^2 = 0.9593$)
Pig monocytes	11.22^{**} ($R^2 = 0.9804$)	2.038^{**} ($R^2 = 0.9964$)

Table 2.1, Medial Lethal Doses (LC_{50})[55] for SA-D-K_6L_9-AS and D-K_6L_9 for Cancerous (GL26, 4T1) and non-cancerous cell lines (NSC, Pig Monocytes).

Determined by means of the MTT[48] assay. All concentrations are micromolar (μM L^{-1})

* Linear fit.
** Non-linear fit, one phase decay
*** Non-linear fit, plateau followed by one phase decay

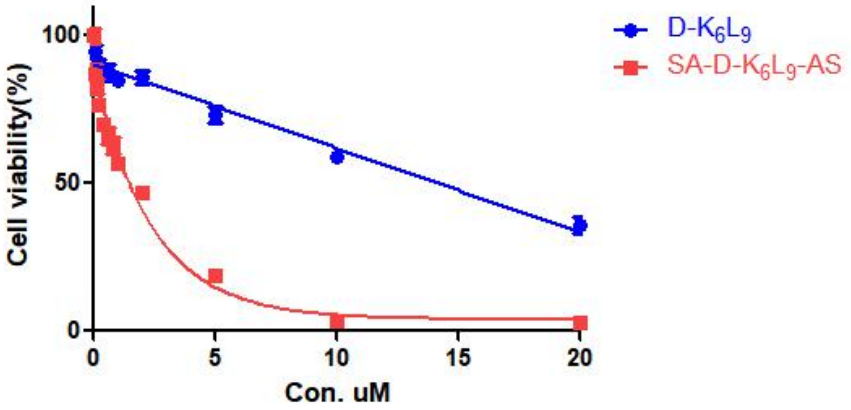

Figure 2.11, Cell viabilities (in percent) of GL26 cells, as determined by means of the MTT assay, vs. concentration of SA-D-K_6L_9-AS or D-K_6L_9 in 10% FBS containing RPMI medium after 24h of incubation.

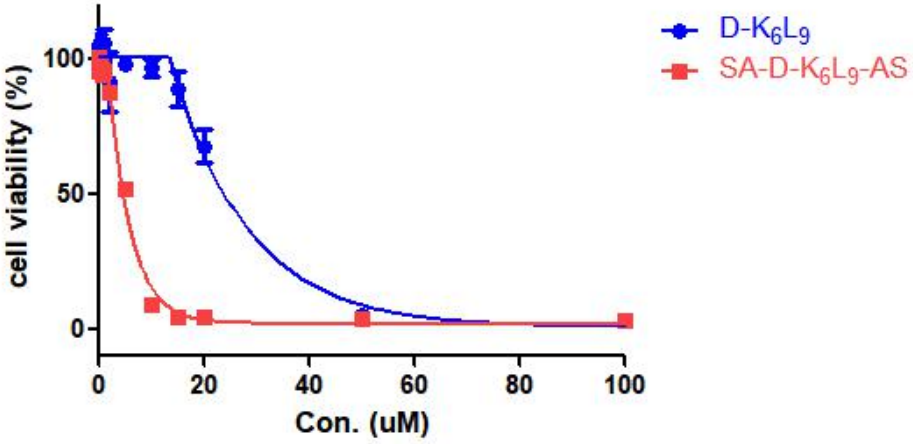

Figure 2.12, Cell viabilities (in percent) of 4T1 cells, as determined by means of the MTT assay, vs. concentration of SA-D-K_6L_9-AS or D-K_6L_9 in 10% FBS containing RPMI medium after 24h of incubation.

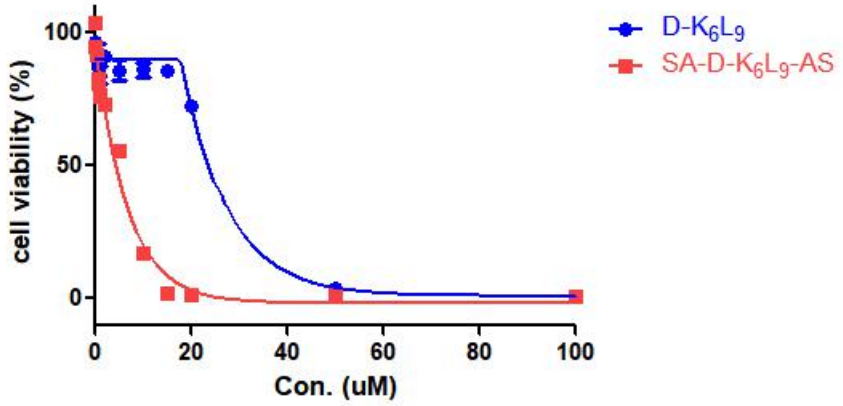

Figure 2.13, Cell viabilities (in percent) of NSC cells, as determined by means of the MTT assay, vs. concentration of SA-D-K_6L_9-AS or D-K_6L_9 in NSC medium after 24h of incubation.

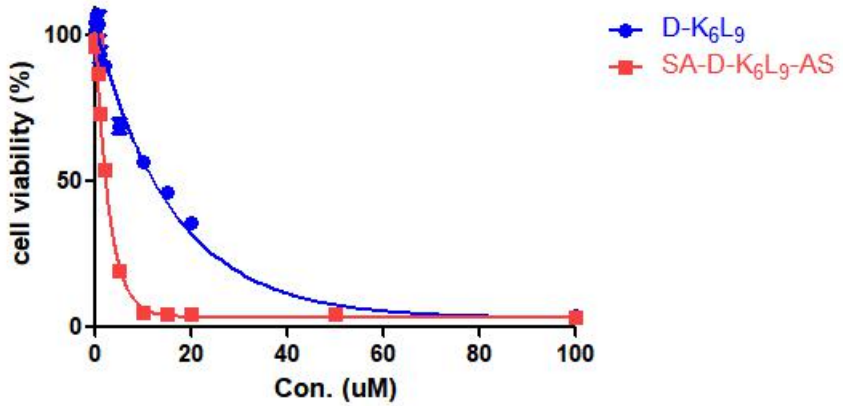

Figure 2.14, Cell viabilities (in percent) of pig monocytes cells, as determined by means of the MTT assay[48], vs. concentration of SA-D-K_6L_9-AS or D-K_6L_9 in 10% FBS containing RPMI medium after 24h of incubation.

Based on the results of the MTT assays, SA-D-K_6L_9-AS is 8.31 to 2.47 times for effective than D-K_6L_9, from which it is derived. Therefore, it is of interest to elucidate the biochemical reasons for the observed increase in efficacy. Shai et al. have determined the secondary structures of L-K_6L_9 and D-K_6L_9 by means of FTIR spectroscopy, more specifically via deconvolution of the amide band I and circular dichroism (CD) spectroscopy.[56] Whereas L-K_6L_9 was found to be predominantly alpha-helical (93%), D-K_6L_9 did neither exhibit an alpha-helical structure, nor did it assume a beta-sheet structure.[56] Therefore, we have decided to study the secondary structure of SA-D-K_6L_9-AS by NMR spectroscopy. It is noteworthy that neither L-K_6L_9 nor D-K_6L_9 can be studied via NMR, because it is not possible to assign all positions in the 15-mer correctly, due to the presence of six lysines and nine leucines in the 15-mer and the resulting spectral overlap. However, the introduction of two serines and two alanines in SA-D-K_6L_9-AS enables the observation of formerly unavailable J-coupling in SALK*L*LK*K*L*LK*KLL*K*LLAS-NH_2 which permits to solve the structure by utilizing the two-dimensional NMR spectroscopic methods.[53]

2.3.4 2D NMR Study of the Secondary Structure of SALK*L*LK*K*L*LK*KLL*K*LLAS

2.3.4.1 Solving the structure of SA-D-K_6L_9-AS

The first step in solving the structure of SA-D-K_6L_9-AS (SALK*L*LK*K*L*LK*KLL*K*LLAS-NH_2) consisted in obtaining the ^{1}H-NMR chemical shifts for all amino acids from the Biological Magnetic Resonance Data Bank.[57] The relevant chemical shifts are summarized in Table 2.2. The positions of the hydrogens are shown in Figure 2.15.

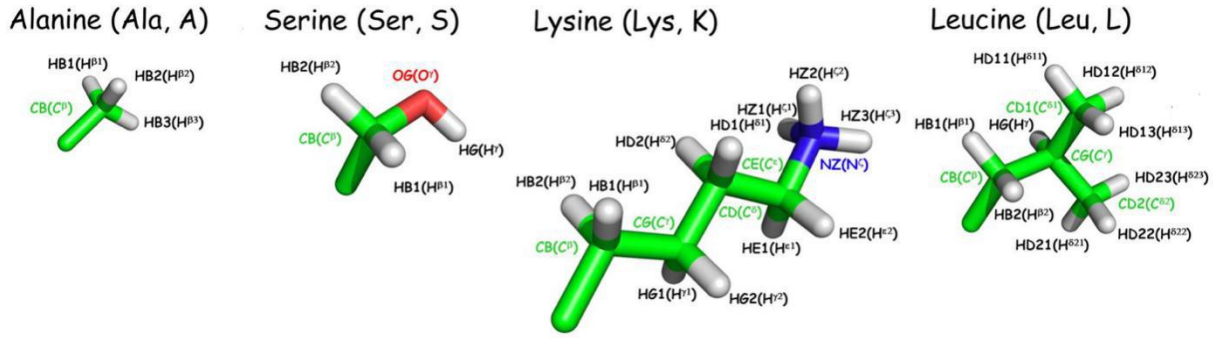

Figure 2.15, Nomenclature used in all NMR assignments.[58] The alpha carbon of each amino acids and their hydrogens (HA) and the hydrogen of the amide bond (HN) are not shown.

	Ala (A)	Ser (S)	Leu (L)	Lys (K)
HN	8.19	8.29	8.22	8.18
HA	4.25	4.48	4.31	4.26
HB	1.35	3.87/3.84	1.61/1.52	1.77/1.74
HG		5.45 (OH)	1.50	1.36/1.35
HD			0.75/0.72	1.61/1.59
HE				2.91/2.90
HZ				7.32 (-NH_2)

Table 2.2, Chemical Shifts of Alanine, Serine, Leucine, and Lysine[57] The positions of the hydrogen atoms are shown in Figure 2.15, with the exception of the hydrogens at the alpha-atoms (HA) and the amide bonds (HN).

The secondary structure of SA-D-K_6L_9-AS (SALK*L*LK*K*L*LK*KLL*K*LLAS) was resolved in three steps: 1) The sequential assignment of the 19-mer was performed through a comparison of the 2D ^{1}H-^{1}H -COSY, NOESY, and TOCSY spectra with the chemical shifts of alanine, serine, leucine, and lysine[57], as well the occurring J-coupling and dipolar cross-relaxation between nuclei in a close spatial relationship. Examples of this strategy are provided in Figures 2.18 and 2.19. 2) After successful assignment of all amino acids in SALK*L*LK*K*L*LK*KLL*K*LLAS, meaningful NOE signals were extracted for the purpose of structure generation. 3) Structure calculations were performed using the software package CNS[51] based on the sequential assignment and a total of 67 NOE signals (see below).

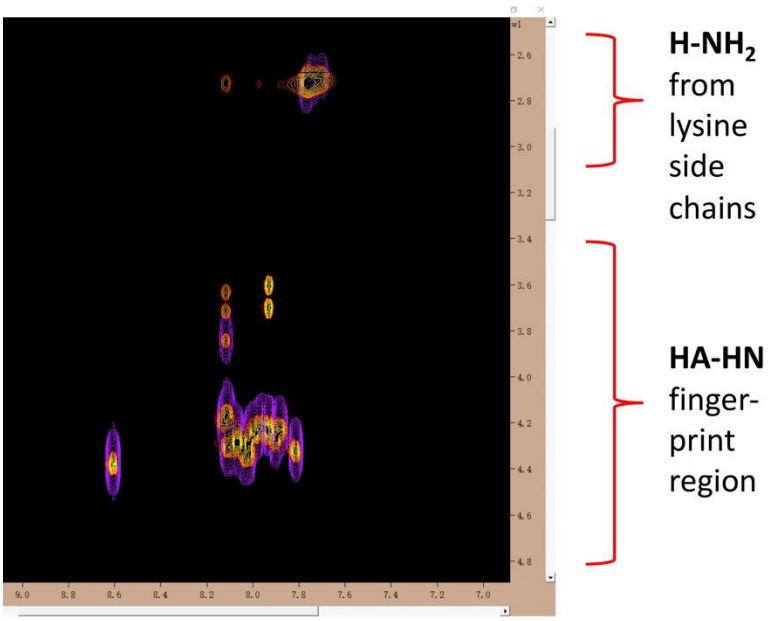

Figure 2.16, Section of the ^{1}H-^{1}H COSY spectrum of SALK*L*LK*K*L*LK*KLL*K*LLAS showing cross-peaks occurring from the fingerprint region and the lysine side chains.
Purple peaks are COSY signal, orange peaks are TOCSY.

In Figure 2.16, a section of the ^{1}H-^{1}H COSY spectrum of SALK*L*LK*K*L*LK*KLL*K*LLAS is shown. The spectral region comprising the HN-HA protons is called the ***fingerprint*** region. A

sufficient spatial resolution in this region is required for successful sequential assignment and subsequent determination of the secondary structure.

Whereas a ^{1}H-^{1}H COSY spectrum reveals scalar couplings within a three-bond coupling network, TOCSY facilitates magnetization transfer from one spin to another without the necessity of direct coupling. Consequently, cross-peaks occur between all members of a coupled spin network. When assigning spins in polypeptides and other biomolecules, TOCSY reveals characteristic spin pattern for specific spin systems. NOESY reveals only direct polar couplings occurring between spins, which have to have a distance of less than 0.5 nm for cross-relaxation to be effective.[59]

Sequential assignment is performed by means of a TOCSY-NOESY sequential walk.[59] TOCSY reveals J-coupled HN-HA cross peaks in the fingerprint region. NOESY uncovers self- and sequential NOE cross peaks (see Figure 2.17)

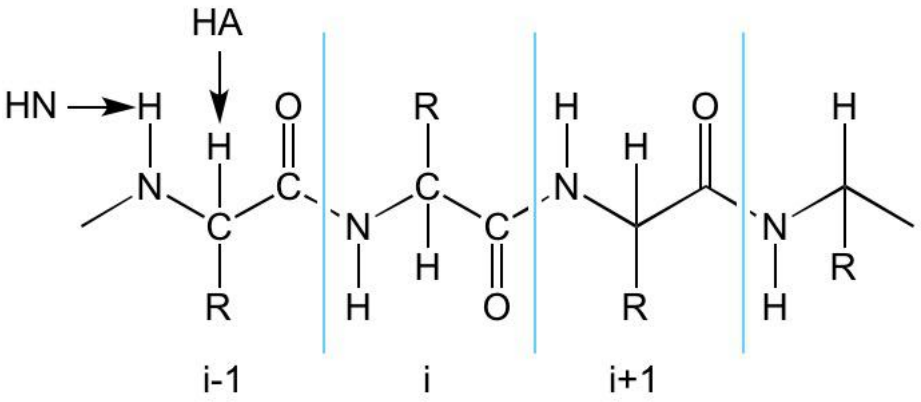

Figure 2.17, "Self" cross peaks occur from NHi-HAi pairs, sequential cross peaks arise from NHi-HA(i-1) pairs.

Figures 2.18 and 2.19 elucidate this approach. The examples depicted show how both alanines in SALK*L*LK*K*L*LK*KLL*K*LLAS were assigned.

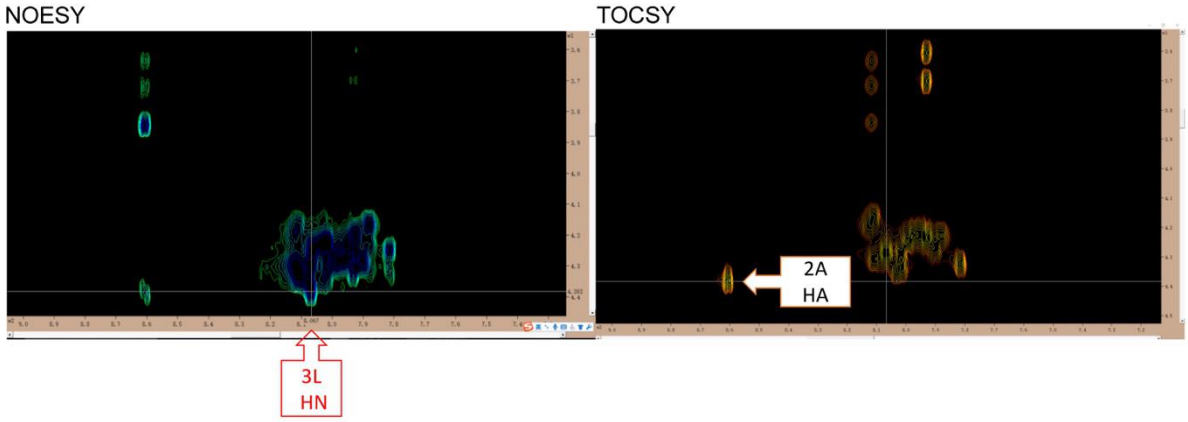

Figure 2.18, TOCSY-NOESY walk: identification of SALK*L*LK*K*L*LK*KLL*K*LLAS

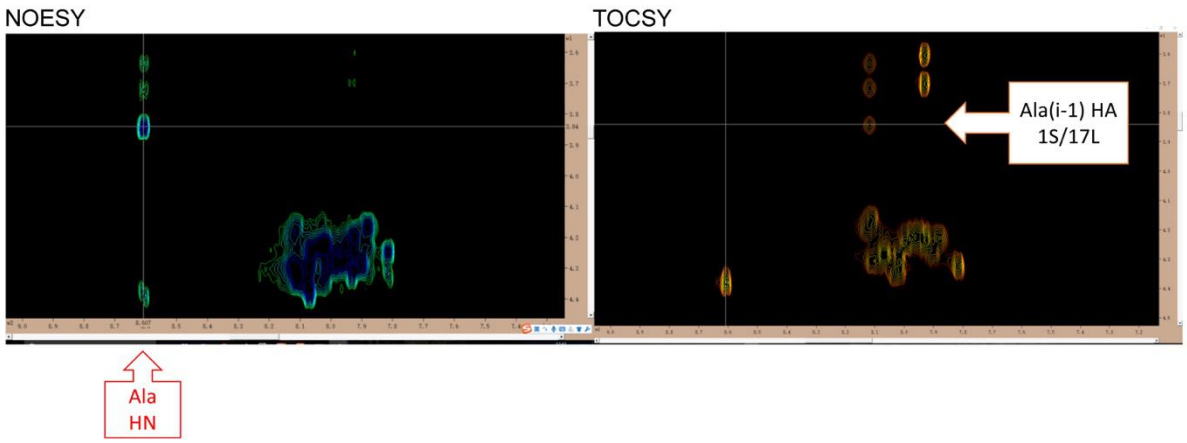

Figure 2.19, TOCSY-NOESY walk: identification of SALK*L*LK*K*L*LK*KLL*K*LLAS

Selected assignments of SALK*L*LK*K*L*LK*KLL*K*LLAS are shown in the TOCSY spectrum in Figure 2.20.

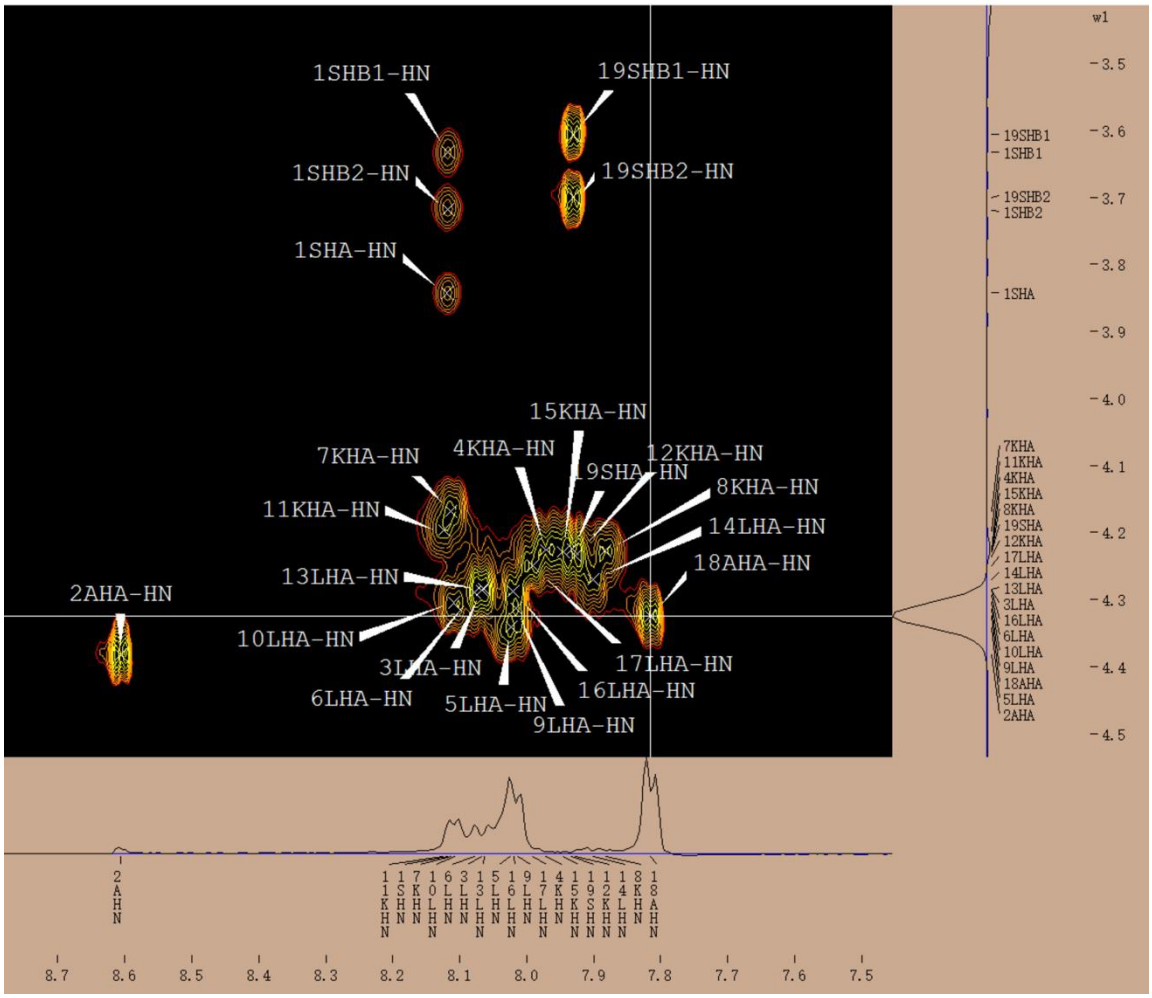

Figure 2.20, Selected assignments in the TOCSY spectrum of SALK*L*LK*K*L*LK*KLL*K*LLAS. Each assignment was confirmed by performing a TOCSY-NOESY walk.

Assignment	W1	W2
1SHA-HN	3.843	8.119
1SHA-OH	3.843	5.513
1SHB1-HA	3.633	3.841
1SHB1-HB2	3.633	3.728
1SHB1-HN	3.633	8.118

1SHB1-OH	3.634	5.513
1SHB2-HA	3.716	3.841
1SHB2-HN	3.718	8.118
1SHB2-OH	3.716	5.514
2AHA-HN	4.382	8.606
2AHB#-HN	1.221	8.606
3LHA-HN	4.286	8.067
3LHB#-HN	1.573	8.068
4KHA-HN	4.226	7.971
4KHB#-HN	1.626	7.972
4KHG#-HN	1.271	7.972
5LHA-HN	4.341	8.024
5LHB#-HN	1.520	8.025
6LHA-HN	4.290	8.078
6LHB#-HN	1.583	8.075
7KHA-HN	4.168	8.113
7KHB#-HN	1.626	8.114
7KHG#-HN	1.315	8.113
8KHA-HN	4.228	7.883
8KHB#-HN	1.657	7.881
8KHG#-HN	1.230	7.881
9LHA-HN	4.313	8.016
9LHB#-HN	1.529	8.014
10LHA-HN	4.305	8.109
10LHB#-HN	1.343	8.105
11KHA-HN	4.197	8.124
11KHB#-HN	1.625	8.123
11KHG#-HN	1.271	8.125
12KHA-HN	4.235	7.927
12KHB#-HN	1.597	7.927

12KHG#-HN	1.242	7.928
13LHA-HN	4.283	8.065
13LHB#-HN	1.583	8.063
14LHA-HN	4.270	7.901
14LHB#-HN	1.548	7.903
15KHA-HN	4.229	7.946
15KHB#-HN	1.629	7.947
15KHG#-HN	1.239	7.946
16LHA-HN	4.288	8.020
16LHB#-HN	1.511	8.020
17LHA-HN	4.249	7.991
17LHB#-HN	1.606	7.991
18AHA-HN	4.325	7.815
18AHB#-HN	1.197	7.814
19SHA-HN	4.225	7.932
19SHA-OH	4.230	5.004
19SHB1-HA	3.606	4.231
19SHB1-HB2	3.605	3.700
19SHB1-HN	3.607	7.931
19SHB1-OH	3.607	5.004
19SHB2-HA	3.700	4.231
19SHB2-HN	3.700	7.931
19SHB2-OH	3.700	5.003

Table 2.3, Peak list for TOCSY.

more than one of the same type of H overlapped.

Assignment	W1	W2	Note		
1SHA-2AHN	3.845	8.606	s	q	n
1SHB1-2AHN	3.634	8.606	w	q	n
1SHB2-2AHN	3.719	8.606	w	q	n
2AHA-3LHN	4.382	8.070	s	q	n
3LHA-4KHN	4.286	7.971	s	q	n
3LHB#-4KHN	1.572	7.973	m	q	y
3LHN-2AHN	8.069	8.607	m	q	n
3LHN-4KHN	8.065	7.973	m	q	n
4KHA-5LHN	4.225	8.025	s	q	n
4KHG#-6LHN	1.276	8.079	m	l	y
5LHA-6LHN	4.343	8.074	s	q	n
5LHN-8KHN	8.028	7.882	s	l	n
6LHA-7KHN	4.297	8.112	s	q	n
6LHN-4KHN	8.080	7.973	m	l	n
6LHN-5LHN	8.085	8.026	s	q	n
7KHA-8KHN	4.169	7.881	s	q	n
7KHB#-8KHN	1.627	7.881	s	q	y
7KHG#-5LHN	1.311	8.024	m	l	y
7KHG#-6LHN	1.311	8.078	m	q	y
7KHG#-9LHN	1.307	8.013	m	l	y
7KHG#-12KHN	1.313	7.928	w	l	y
7KHG#-13LHN	1.311	8.062	w	l	y
7KHN-5LHN	8.113	8.026	s	l	n
7KHN-8KHN	8.113	7.884	s	q	n
8KHA-9LHN	4.230	8.012	s	q	n
8KHB#-5LHN	1.649	8.024	s	l	y
8KHG#-3LHN	1.228	8.067	s	l	y
9LHA-10LHN	4.319	8.107	s	q	n
10LHA-11KHN	4.304	8.119	s	q	n

10LHB#-6LHN	1.341	8.082	w	l	y
10LHB#-8KHN	1.338	7.875	w	l	y
10LHB#-12KHN	1.340	7.929	w	l	y
10LHB#-13LHN	1.340	8.059	w	l	y
10LHN-8KHN	8.104	7.882	s	l	n
10LHN-9LHN	8.111	8.013	s	q	n
10LHN-12KHN	8.103	7.928	m	l	n
11KHA-12KHN	4.199	7.929	s	q	n
11KHG#-9LHN	1.269	8.013	m	l	y
11KHN-8KHN	8.130	7.882	s	l	n
11KHN-12KHN	8.125	7.928	s	q	n
11KHN-13LHN	8.128	8.064	s	l	n
12KHA-13LHN	4.238	8.065	s	q	n
12KHG#-5LHN	1.243	8.025	s	l	y
13LHA-14LHN	4.287	7.901	s	q	n
13LHB#-16LHN	1.581	8.018	m	l	y
13LHN-12KHN	8.063	7.928	s	q	n
13LHN-14LHN	8.065	7.901	s	q	n
14LHA-15KHN	4.270	7.946	s	q	n
14LHN-18AHN	7.901	7.814	m	l	n
15KHA-16LHN	4.229	8.020	s	q	n
15KHB#-9LHN	1.628	8.016	s	l	y
15KHG#-19SHN	1.235	7.937	s	l	y
15KHN-14LHN	7.948	7.896	s	q	n
15KHN-18AHN	7.944	7.817	w	l	n
16LHA-17LHN	4.286	7.991	s	q	n
16LHB#-13LHN	1.509	8.060	s	l	y
16LHB#-14LHN	1.509	7.905	m	l	y
16LHN-15KHN	8.020	7.941	s	q	n
17LHA-18AHN	4.250	7.814	s	q	n

17LHG-14LHN	1.463	7.901	s	l	n
17LHG-18AHN	1.466	7.813	s	q	n
17LHG-19SHN	1.464	7.938	s	l	n
17LHN-6LHN	7.989	8.076	s	l	n
17LHN-18AHN	7.993	7.813	m	q	n
18AHA-19SHN	4.326	7.932	s	q	n
18AHB#-19SHN	1.197	7.931	m	q	y
18AHN-19SHN	7.818	7.933	m	q	n

Table 2.4, Peak list for NOESY.

more than one of the same type of H overlapped.

s/m/w means signal intensity, strong /medium /weak.

l/q means whether the two residues next to each other, long /sequential.

y/n means whether there are more than one of the same type H overlapped, same as #, yes /no.

2.3.4.2 Extraction of NOE signals for the Purpose of Structure Generation

In total, 67 meaningful NOE signals were extracted for the purpose of structure generation. The restrains limits used for each assignment are listed below.

assign (residue 1 and name HA) (residue 2 and name HN) 2.2 0.4 0.3
assign (residue 2 and name HA) (residue 3 and name HN) 2.2 0.4 0.3
assign (residue 3 and name HA) (residue 4 and name HN) 2.2 0.4 0.3
assign (residue 4 and name HA) (residue 5 and name HN) 2.2 0.4 0.3
assign (residue 5 and name HA) (residue 6 and name HN) 2.2 0.4 0.3
assign (residue 5 and name HN) (residue 8 and name HN) 2.2 0.4 0.3
assign (residue 6 and name HA) (residue 7 and name HN) 2.2 0.4 0.3
assign (residue 6 and name HN) (residue 5 and name HN) 2.2 0.4 0.3
assign (residue 7 and name HA) (residue 8 and name HN) 2.2 0.4 0.3
assign (residue 7 and name HN) (residue 5 and name HN) 2.2 0.4 0.3
assign (residue 7 and name HN) (residue 8 and name HN) 2.2 0.4 0.3
assign (residue 8 and name HA) (residue 9 and name HN) 2.2 0.4 0.3
assign (residue 9 and name HA) (residue 10 and name HN) 2.2 0.4 0.3
assign (residue 10 and name HA) (residue 11 and name HN) 2.2 0.4 0.3
assign (residue 10 and name HN) (residue 8 and name HN) 2.2 0.4 0.3
assign (residue 10 and name HN) (residue 9 and name HN) 2.2 0.4 0.3

assign (residue 11 and name HA) (residue 12 and name HN) 2.2 0.4 0.3
assign (residue 11 and name HN) (residue 8 and name HN) 2.2 0.4 0.3
assign (residue 11 and name HN) (residue 12 and name HN) 2.2 0.4 0.3
assign (residue 11 and name HN) (residue 13 and name HN) 2.2 0.4 0.3
assign (residue 12 and name HA) (residue 13 and name HN) 2.2 0.4 0.3
assign (residue 13 and name HA) (residue 14 and name HN) 2.2 0.4 0.3
assign (residue 13 and name HN) (residue 12 and name HN) 2.2 0.4 0.3
assign (residue 13 and name HN) (residue 14 and name HN) 2.2 0.4 0.3
assign (residue 14 and name HA) (residue 15 and name HN) 2.2 0.4 0.3
assign (residue 15 and name HA) (residue 16 and name HN) 2.2 0.4 0.3
assign (residue 15 and name HN) (residue 14 and name HN) 2.2 0.4 0.3
assign (residue 16 and name HA) (residue 17 and name HN) 2.2 0.4 0.3
assign (residue 16 and name HN) (residue 15 and name HN) 2.2 0.4 0.3
assign (residue 17 and name HA) (residue 18 and name HN) 2.2 0.4 0.3
assign (residue 17 and name HG) (residue 14 and name HN) 2.2 0.4 0.3
assign (residue 17 and name HG) (residue 19 and name HN) 2.2 0.4 0.3
assign (residue 17 and name HN) (residue 6 and name HN) 2.2 0.4 0.3
assign (residue 18 and name HA) (residue 19 and name HN) 2.2 0.4 0.3
assign (residue 17 and name HA) (residue 18 and name HN) 2.2 0.4 0.3
assign (residue 3 and name HN) (residue 2 and name HN) 3.2 1.4 0.3
assign (residue 3 and name HN) (residue 4 and name HN) 3.2 1.4 0.3
assign (residue 6 and name HN) (residue 4 and name HN) 3.2 1.4 0.3
assign (residue 10 and name HN) (residue 12 and name HN) 3.2 1.4 0.3
assign (residue 14 and name HN) (residue 18 and name HN) 3.2 1.4 0.3
assign (residue 17 and name HN) (residue 18 and name HN) 3.2 1.4 0.3
assign (residue 18 and name HN) (residue 19 and name HN) 3.2 1.4 0.3
assign (residue 1 and name HB1) (residue 2 and name HN) 4 2.2 1
assign (residue 1 and name HB2) (residue 2 and name HN) 4 2.2 1
assign (residue 15 and name HN) (residue 18 and name HN) 4 2.2 1
assign (residue 7 and name HB#) (residue 8 and name HN) 3.2 1 0.3
assign (residue 8 and name HB#) (residue 5 and name HN) 3.2 1 0.3
assign (residue 8 and name HG#) (residue 3 and name HN) 3.2 1 0.3
assign (residue 12 and name HG#) (residue 5 and name HN) 3.2 1 0.3
assign (residue 15 and name HB#) (residue 9 and name HN) 3.2 1 0.3
assign (residue 15 and name HG#) (residue 19 and name HN) 3.2 1 0.3
assign (residue 16 and name HB#) (residue 13 and name HN) 3.2 1 0.3
assign (residue 3 and name HB#) (residue 4 and name HN) 4.2 2 0.3
assign (residue 4 and name HG#) (residue 6 and name HN) 4.2 2 0.3
assign (residue 7 and name HG#) (residue 5 and name HN) 4.2 2 0.3
assign (residue 7 and name HG#) (residue 6 and name HN) 4.2 2 0.3
assign (residue 7 and name HG#) (residue 9 and name HN) 4.2 2 0.3
assign (residue 11 and name HG#) (residue 9 and name HN) 4.2 2 0.3
assign (residue 13 and name HB#) (residue 16 and name HN) 4.2 2 0.3

assign (residue 16 and name HB#) (residue 14 and name HN) 4.2 2 0.3
assign (residue 18 and name HB#) (residue 19 and name HN) 4.2 2 0.3
assign (residue 7 and name HG#) (residue 12 and name HN) 5 2.8 1
assign (residue 7 and name HG#) (residue 13 and name HN) 5 2.8 1
assign (residue 10 and name HB#) (residue 6 and name HN) 5 2.8 1
assign (residue 10 and name HB#) (residue 8 and name HN) 5 2.8 1
assign (residue 10 and name HB#) (residue 12 and name HN) 5 2.8 1
assign (residue 10 and name HB#) (residue 13 and name HN) 5 2.8 1

In Figures 2.21, 2.22, and 2.23, the resulting NOE signals in the finger print region, NH-CH region, and NH-NH region of the NOESY of SALK*L*LK*K*L*LK*KLL*K*LLAS are shown.

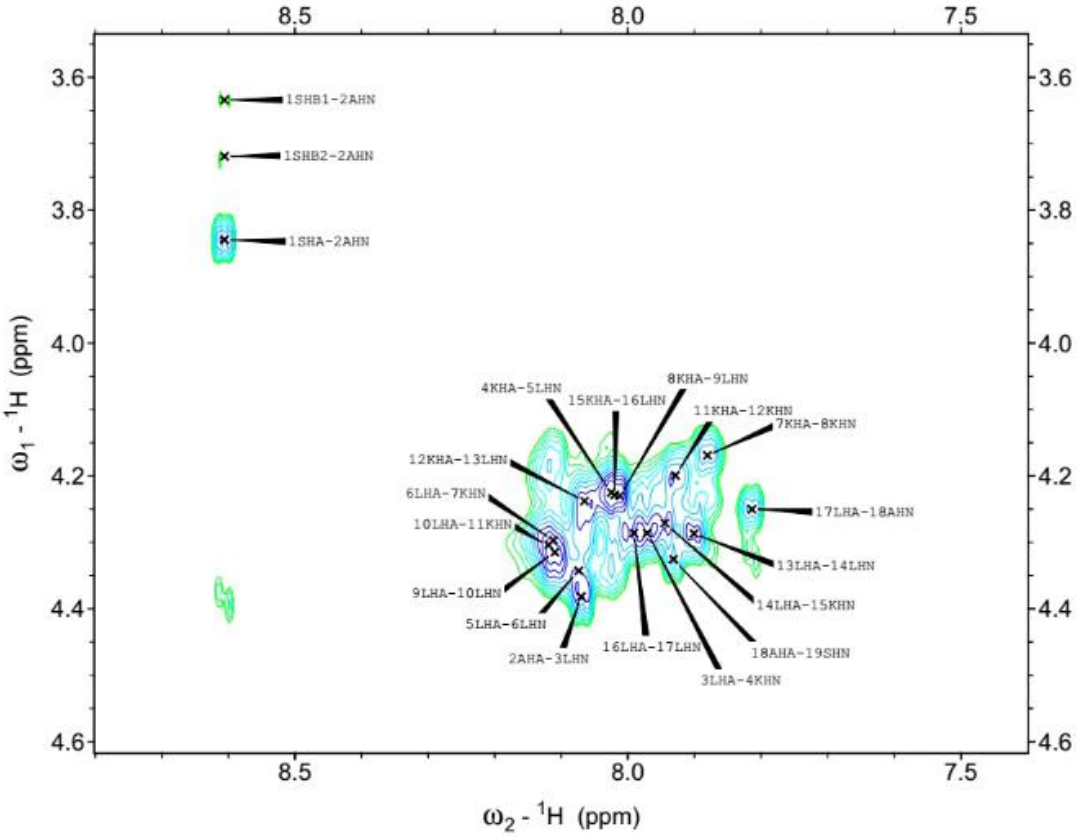

Figure 2.21, NOESY spectrum of SALK*L*LK*K*L*LK*KLL*K*LLAS: finger print region.

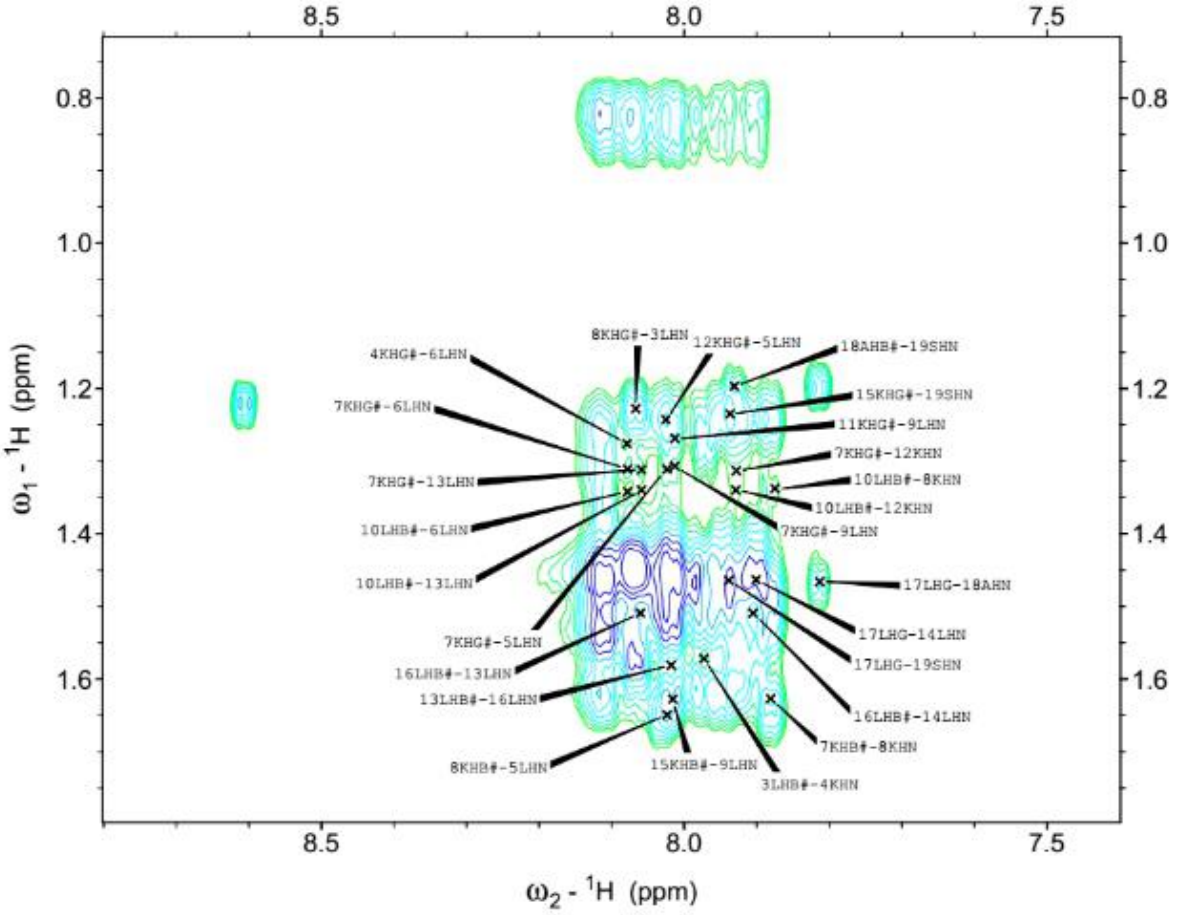

Figure 2.22, NOESY spectrum of SALK*L*LK*K*L*LK*KLL*K*LLAS: NH-CH region.

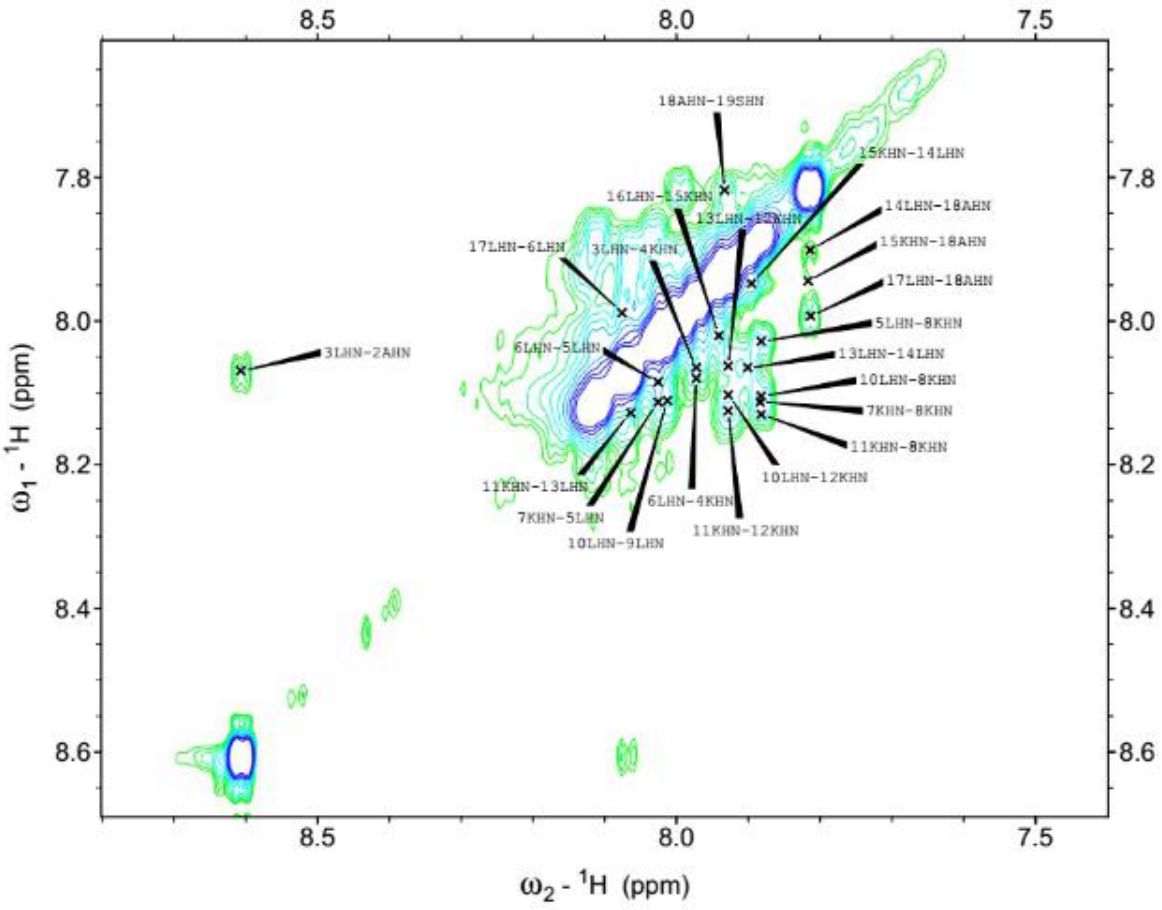

Figure 2.23, NOESY spectrum of SALK*L*LK*K*L*LK*KLL*K*LLAS: NH-NH region.

2.3.4.3 Structure Calculation Utilizing the Software Package CNS[51]

Protein structure calculations were performed using the software package CNS[51] based on the sequential assignment and a total of 67 NOE signals that are depicted in Figures 2.21, 2.22, and 2.23. Table 2.5 summarized the results of this calculation. Based on the energies of the optimized structures and the number of NOE violations, have obtained 10 annealed structures, which are summarized in Table 2.5. All 10 structures are provided in the Supplemental Information Section.

Annealed Structure	#1	#2	#3	#4	#5	#6	#7	#8	#9	#10
Number of NOE Violations	13	7	9	8	10	8	8	9	13	7
Total Energy (kcal/mol)	2158	2117	2337	2339	2120	2201	2026	2699	2474	2277

Table 2.5, Energies of the 10 best annealed structures, as well as number of NOE violations, as calculated by the software package CNS.[51]

The most likely structures are #2 and #10, based on the smallest number of NOE violations (7). The lowest energies of the annealed structures were calculated for #7, #2, and #5 (in this sequence). Therefore #2, which has the lowest number of NOE violations and the second lowest energy of the annealed structure, is the most likely secondary structure. As it can be seen in Figure 2.24, the secondary structure (tube mode) of SALK*L*LK*K*L*LK*KLL*K*LLAS is a distorted alpha-helix. This is in agreement with previous findings by means of FTIR deconvolution and circular dichroism (CD) spectroscopy[56], which have revealed an amorphous structure for D-K_6L_9 (LK*L*LK*K*L*LK*KLL*K*LL).

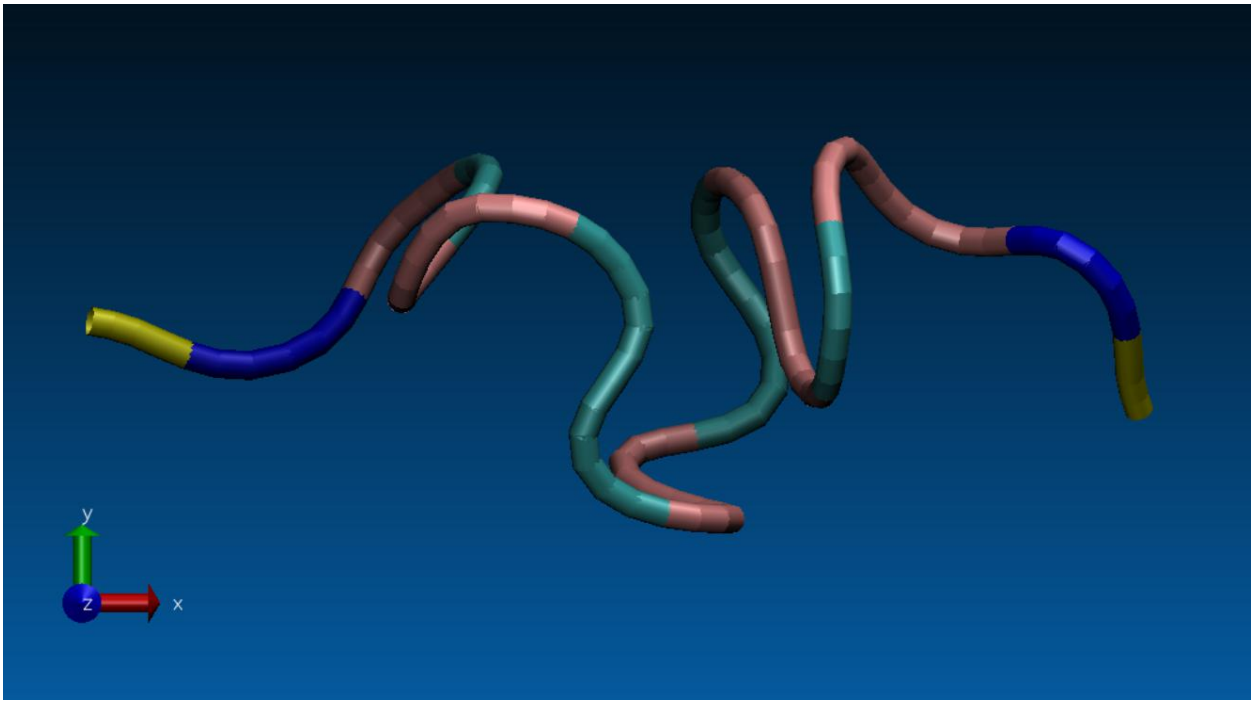

Figure 2.24, Most probable secondary structure (tube mode) of SA-D-K_6L_9-AS (SALK*L*LK*K*L*LK*KLL*K*LLAS) in DMSO (D6)

Based on the lowest number of NOE violations (7) and a total energy of 2117 kcal/mol, as calculated by CNS.

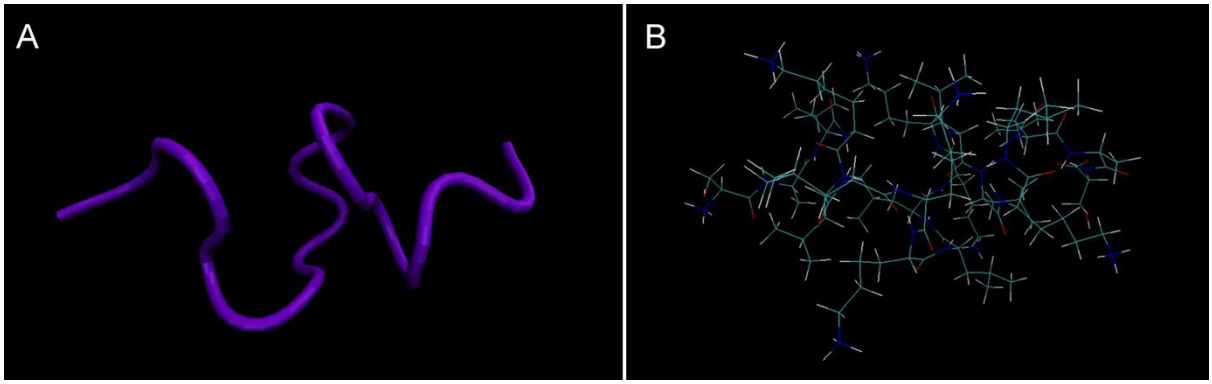

Figure 2.25, Comparison of tube mode structure (A) and molecular structure (B) of SALK*L*LK*K*L*LK*KLL*K*LLAS.

It should be noted that all 10 annealed structures of SALK*L*LK*K*L*LK*KLL*K*LLAS, as summarized in Table 2.5, exhibit distorted alpha-helical structures that are formed by LK*L*LK*K*L*LK*KLL*K*LL (see Supplementary Information section). Based on this finding, our

paradigm is that SA-D-K_6L_9-AS is able to interact with mammalian cell membranes, because the D-K_6L_9 segment (LK*L*LK*K*L*LK*KLL*K*LL) is assuming a similar secondary structure than this is known for not derivatized D-K_6L_9.[56] However, the comparison of the NMR-derived secondary structure of SALK*L*LK*K*L*LK*KLL*K*LLAS with the formerly known structure of LK*L*LK*K*L*LK*KLL*K*LL does NOT explain the significantly higher cell killing efficacy of SA-D-K_6L_9-AS, compared to D-K_6L_9. In order to better understand the biochemical consequences of adding SA and AS to D-K_6L_9 we have performed confocal microscopy experiments of rhodamine B – derivatized SA-D-K_6L_9-AS.

2.3.5 Confocal Microcopy Studies of the Interaction of SA-D-K_6L_9-AS with GL26 Cells and Pig Monocytes.

Rhodamine B was selected as fluorescent dye for our confocal microscopy studies because of its good absorption properties and high emission quantum yield (Φ= 0.45 to 1.0, depending on concentration and excitation parameters[60-61]). A second rationale for attaching rhodamine B to the C-terminus of SA-D-K_6L_9-AS is that Shai et. al. had attached the same dye to D-K_6L_9-AS in their confocal studies.[25]

Laser confocal microscopy of live and fixed cells was performed in the Confocal Microscopy and Microfluorometry Core in the Department of Anatomy & Physiology at Kansas State University. A Carl Zeiss LSM 880 confocal microscope was used. Laser excitation was performed at 553 nm. The emission of SA-D-K_6L_9-AS- attached rhodamine B was monitored at λ = 627 nm.

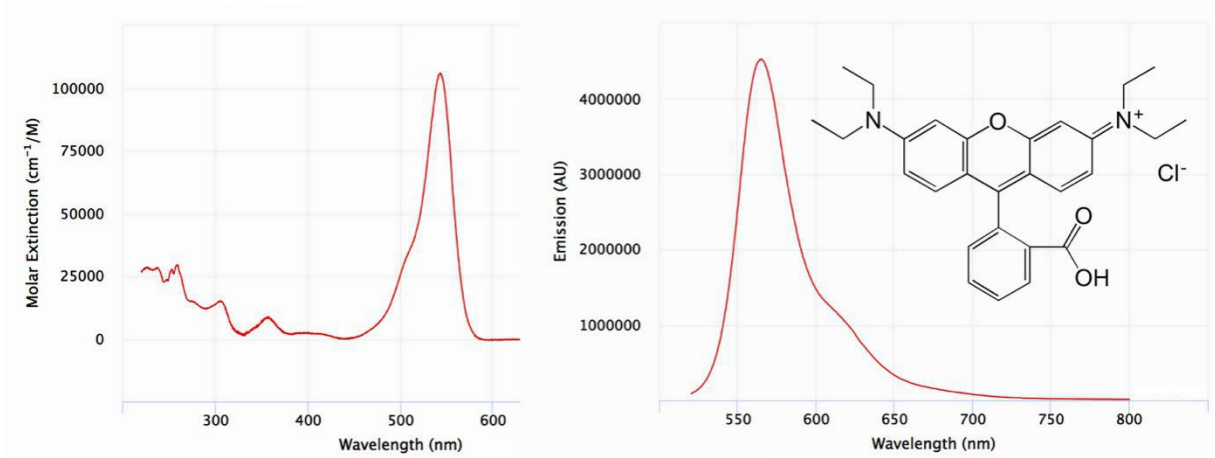

Figure 2.26, Chemical structure, UV/Vis-absorption, and fluorescence spectrum of Rhodamine B.

(IUPAC name: [9-(2-carboxyphenyl)-6-diethylamino-3-xanthenylidene]-diethylammonium chloride (λ_{ex} = 542.8 nm (106,000 cm^{-1}/M), λ_{ex} = 565 nm in ethanol)[61]

2.3.5.1 Static Confocal Imaging

For the purpose of static confocal imaging, the GL26 cells and pig monocytes were prepared by means of the following procedure: 1) the cells were treated with rhodamine-labeled SA-D-K_6L_9-AS (3μM) for 20 min. 2) After treatment, the cells were washed with PBS (phosphate-buffered saline solution) three times and then fixed with 4% formaldehyde solution. 3) The nuclei of the fixed cells were stained with Hoechst 33342 (1 μg /mL) for 10 min. Hoechst 33342 is a DNA-intercalating dye that shows blue fluorescence. Fluorescence occurring from peptide-bound Rhodamine B is red.

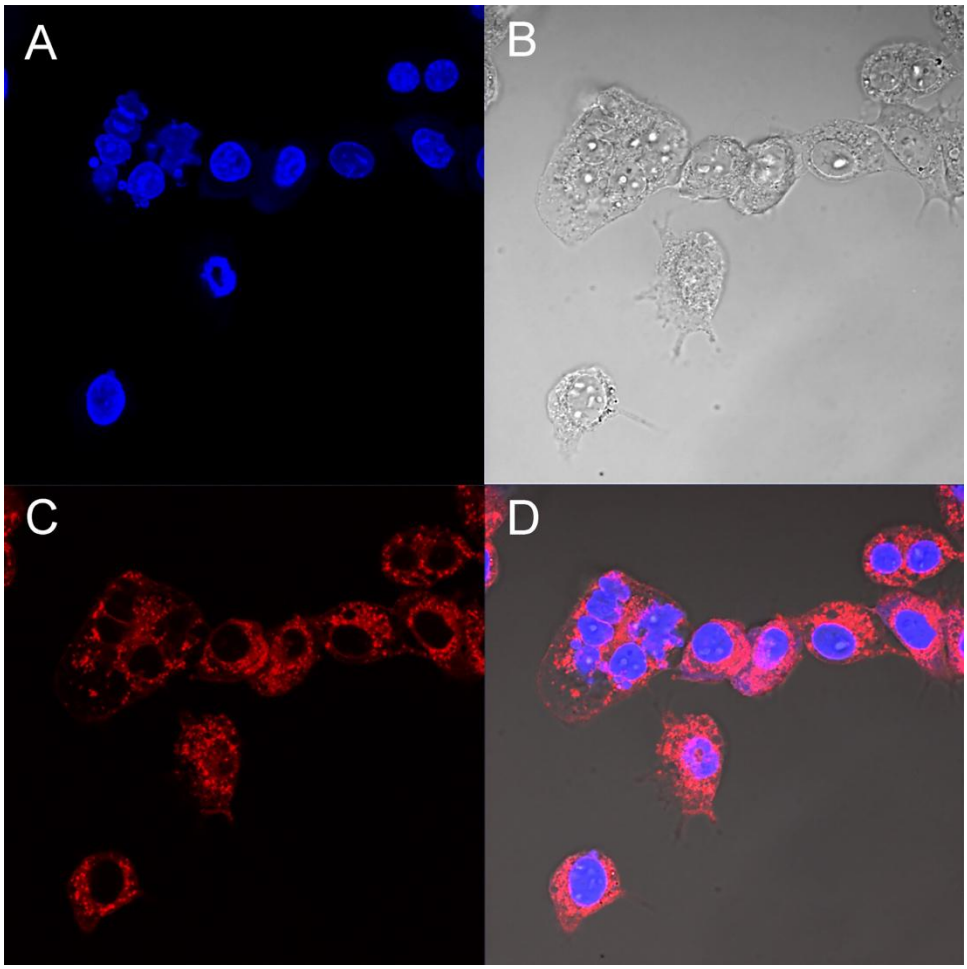

Figure 2.27, Fluorescence microscopy of GL26 stained with Hoechst 33342 and Rhodamine B labeled peptide.

Cells were treated with 3 μM of Rhodamine B labeled SA-D-K_6L_9-AS for 20min., prior to washing (3x) and cell fixing procedure; 40x magnification; A: nuclear staining with Hoechst 33342, B: bright field image, C: Red emission occurring from Rhodamine B labeled SA-D-K_6L_9-AS), D: overlay of A, B, and C.

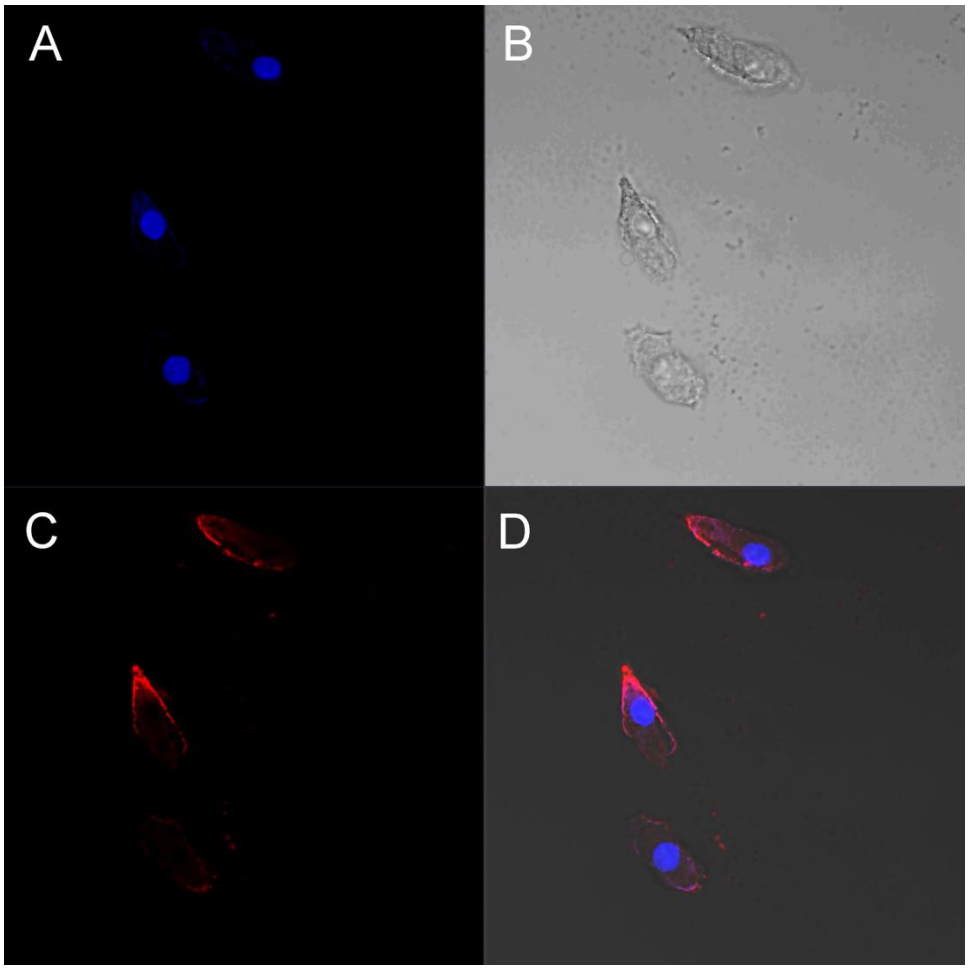

Figure 2.28, Fluorescence microscopy of pig monocytes stained with Hoechst 33342 and Rhodamine B labeled peptide.

Cells were treated with 3 μM of Rhodamine B labeled SA-D-K_6L_9-AS for 20min., prior to washing (3x) and cell fixing procedure; 40x magnification; A: nuclear staining with Hoechst 33342, B: bright field image, C: Red emission occurring from Rhodamine B labeled SA-D-K_6L_9-AS), D: overlay of A, B, and C.

The confocal imaging results for both, GL26 cells and pig monocytes have established that Rhodamine B labeled SA-D-K_6L_9-AS targets the cell membranes. This was anticipated, based on previous literature reports.[25] The intensity of red fluorescence at the from the cell membranes is heterogeneously distributed, which is in support of the Carpet mechanism[35]. Apparently, SA-D-K_6L_9-AS aggregates in distinct regions and dissolves the cell membrane, leading to necrotic cell death. Principally, there are (at least) two different possibilities: A) The

first SA-D-K_6L_9-AS peptide sequences are absorbed at or absorbed in the cell membrane, causing disorder, which favors the binding of further SA-D-K_6L_9-AS peptide sequences. Once a carpet of SA-D-K_6L_9-AS peptide sequences is formed on the surface, a part of the cell membrane is dissolved (see Figure 1.5 carpet mechanism[35]). B) The second possibility consists of the existence of negatively charged areas on both, GL26 and pig monocyte surfaces, which attracts SA-D-K_6L_9-AS peptide sequences. We were unable to distinguish between both possibility by means of confocal microscopy.

It is noteworthy that the cells' nuclei (regions of blue fluorescence due to staining with Hoechst 33342) did not exhibit any red fluorescence, as the overlays in Figures 2.27 and 2.28 clearly prove. This can be regarded as experimental proof that SA-D-K_6L_9-AS does not target cell nuclei, at least not within 20 min. of exposure. The capability of SA-D-K_6L_9-AS to target cell membranes and to cause membrane disruption / dissolution is in very good agreement with its secondary structure (Figure 2.24). Although this structure was determined in DMSO(D_6) as solvent because of technical reasons, the results from confocal microscopy principally confirm the NMR findings.

2.3.5.2 Live Confocal Imaging

We have performed live confocal imaging experiments with GL26 cells and pig monocytes to ascertain, whether SA-D-K_6L_9-AS only reacts with cell surfaces, or whether it is able to target other cell organelles as well. GL26 cells were plated in glass bottom microwell dishes with 8,000/cm^2, as described. Cells were washed with PBS after overnight incubation. 3 μM Rhodamine-B labeled peptide SA-D-K_6L_9-SA was dissolved in RPMI (with 10% FBS) medium. The solution was added to cells and incubated at 37℃. Pig monocytes were used in a same way.

The confocal imaging experiments with live cells confirmed the findings from the confocal imaging of fixed cells. Rhodamine-B labeled peptide SA-D-K_6L_9-SA forms patches on the cell surfaces, leading to partial dissolution of entire membrane sections. This results in "streaking", which is shown below. This has to be regarded as a clear indication for the carpet mechanism[35].

Figure 2.29, Confocal bright field image of pig monocytes that were incubated with 3 µM Rhodamine-B labeled peptide SA-D-K_6L_9-SA for 10 min.

2.3.5.3 Co-Staining of Mitochondria

The fluorescent dye Mitotracker Green FM (λ_{ex} = 490nm, λ_{em} = 516 nm)[62] was utilized to stain the mitochondria in GL26 cells and pig monocytes. Both, GL26 cells and pig monocytes were pre-treated with 0.10 μM of Mitotracker Greem FM for 30 min. and then washed with PBS to remove the dye that was not taken up.

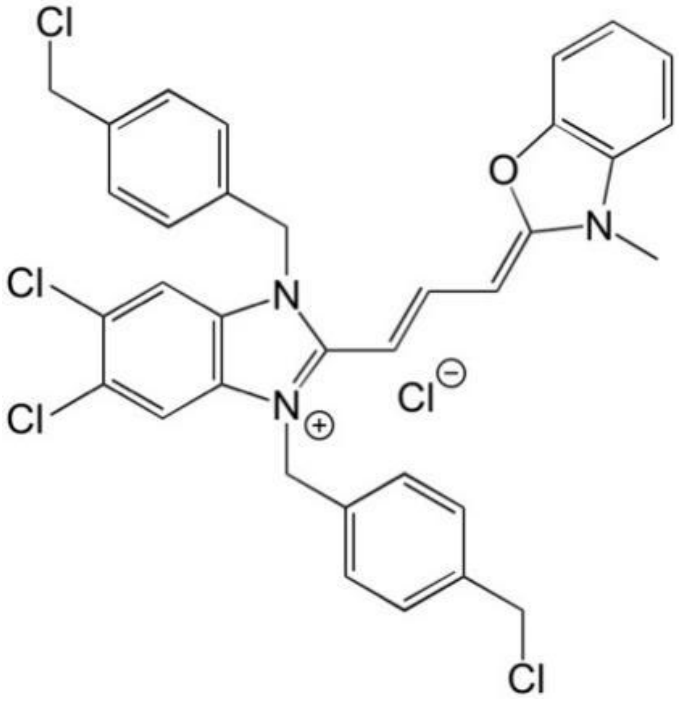

Figure 2.30, Mitotracker Green FM[62], λ_{ex} = 490nm, λ_{em} = 516 nm

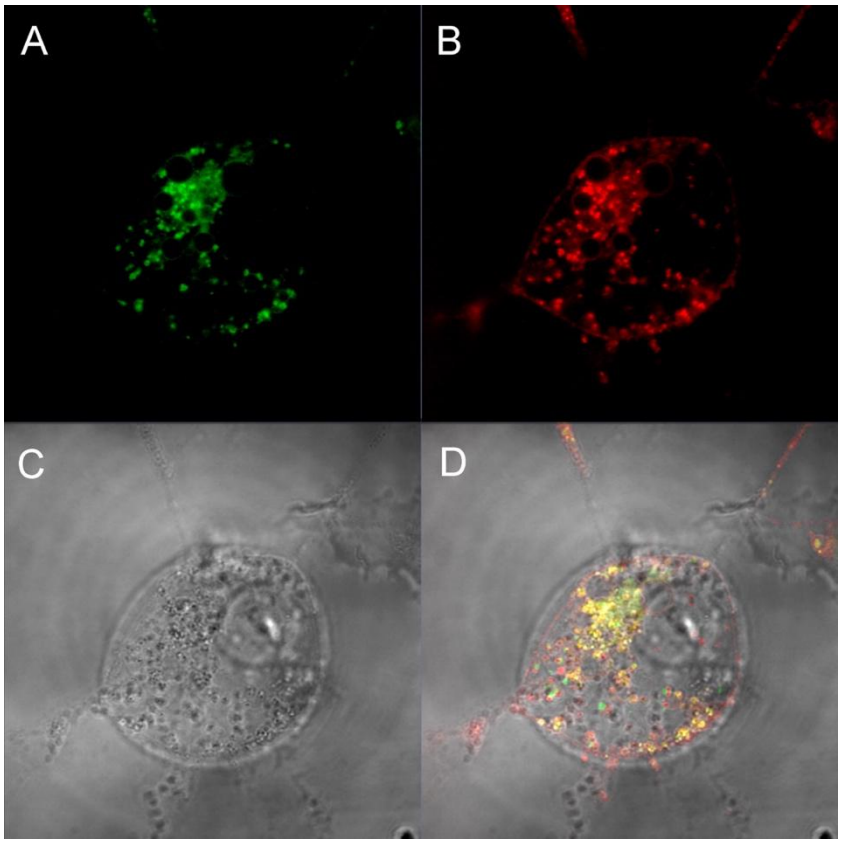

Figure 2.31, Fluorescence microscopy of GL26 stained with Mitotracker Green FM, treated with 3μM of Rhodamine B labeled SA-D-K_6L_9-AS for live confocal imaging.

(A), Green fluorescence for Mitotracker Green FM. (B), Red fluoreescence for Rhodamine B labeled SA-D-K_6L_9-AS. (C), Bright field image. (D), Overlap of (A) (B) and (C). 400x magnification. Picture captured at 20min after monitoring.

The confocal fluorescence (A,B) and bright field images (C,D) clearly show that both, the green and the red fluorescence occur, principally, from the same locations within the cell. Mitotracker Green FM stains mitochondria.[62] Therefore, since the green and the red fluorescence originate from the same regions, it is our conclusion that SA-D-K_6L_9-SA is able to enter the cells and to target the mitochondria. This was previously not observed for D-K_6L_9.[25] It is noteworthy that the same fluorescent red dye, rhodamine B, was attached to SA-D-K_6L_9-SA in the study by Shai et al. and in our study.[25] Therefore, the novel quality of entering the cells'

interior that SA-D-K_6L_9-SA, but not D-K_6L_9 possesses, cannot be attributed to the presence of the attached dye.

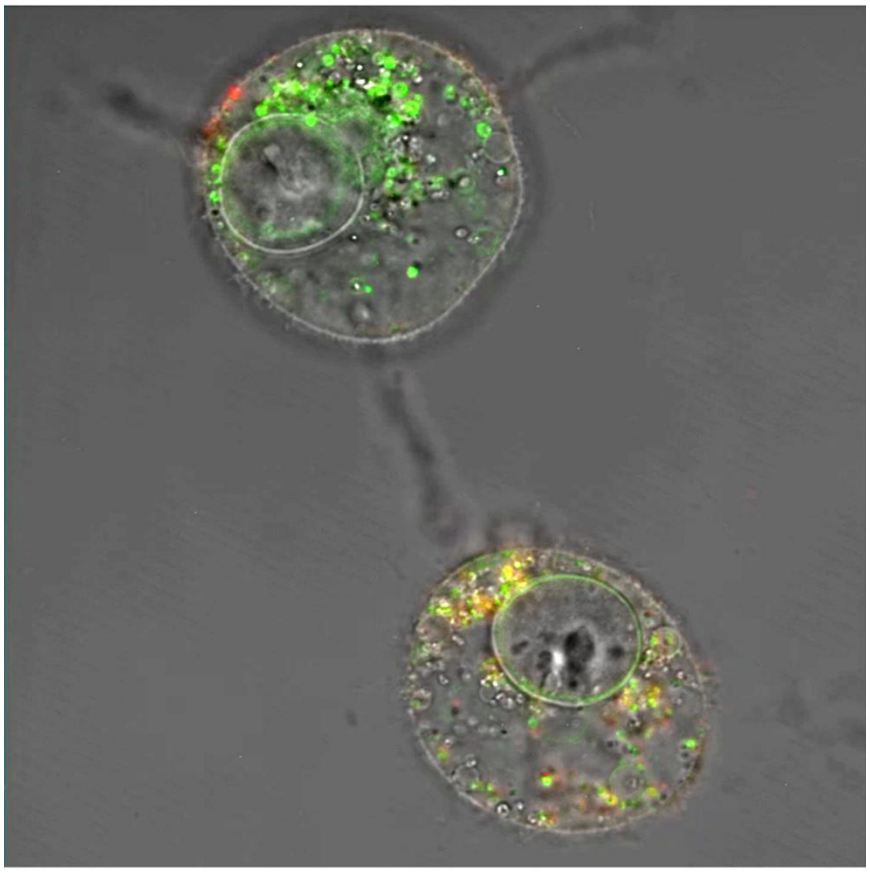

Figure 2.32, GL26 stained with Mitotracker Green FM, treated with 3µM of Rhodamine B labeled SA-D-K6L9-AS for live confocal imaging;
400x. Captured at 30min after monitoring.

As shown in Figure 2.31 and 2.32, SA-D-K_6L_9-SA is also able to enter GL26 cells and to target the mitochondria. A SA-D-K_6L_9-SA patch at/in the cell membrane is clearly visible at the upper cell. This has to be understood as an early event in cell targeting. From there, a fraction of the membrane will be dissolved, leading to necrosis.[35] However, a fraction of SA-D-K_6L_9-SA is apparently able to enter the cells and to associate with the mitochondria. Disruption of mitochondrial membranes leads to apoptosis (programmed cell death).[19] It is noteworthy that

recent studies have found that mitochondria do not feature negative surface charges as long as they remain in a healthy state.[63] However, at the onset of apoptosis, mitochondrial membranes become negative, due to the overexpression of dianionic cardiolipin and flipping of phosphatidylserine across the plasmalemma. Apparently, mitochondrial exposure of negatively charged lipids is key event in apoptosis, because it facilitates the attraction of positively charged proteins, including K-Ras.[63] Since SA-D-K_6L_9-SA bears up to six positive charges, it will be strongly attracted by the mitochondrial membrane upon the onset of apoptosis. For the latter to occur, only a minor disturbance of either the outer or inner mitochondrial membranes is required, which can be triggered by interaction with SA-D-K_6L_9-SA.[19]

The ultra-high resolution confocal bright field image of a pig monocyte that interacts with SA-D-K_6L_9-SA was recorded at 1000X (Figure 2.33). It again shows a SA-D-K_6L_9-SA patch on the outer membrane. Most interesting, it also shows smaller SA-D-K_6L_9-SA patches at the locations of the mitochondria, indicating that mitochondrial targeting is indeed driven by the appearance of negative charges at the outer mitochondrial membrane at the onset of apoptosis.

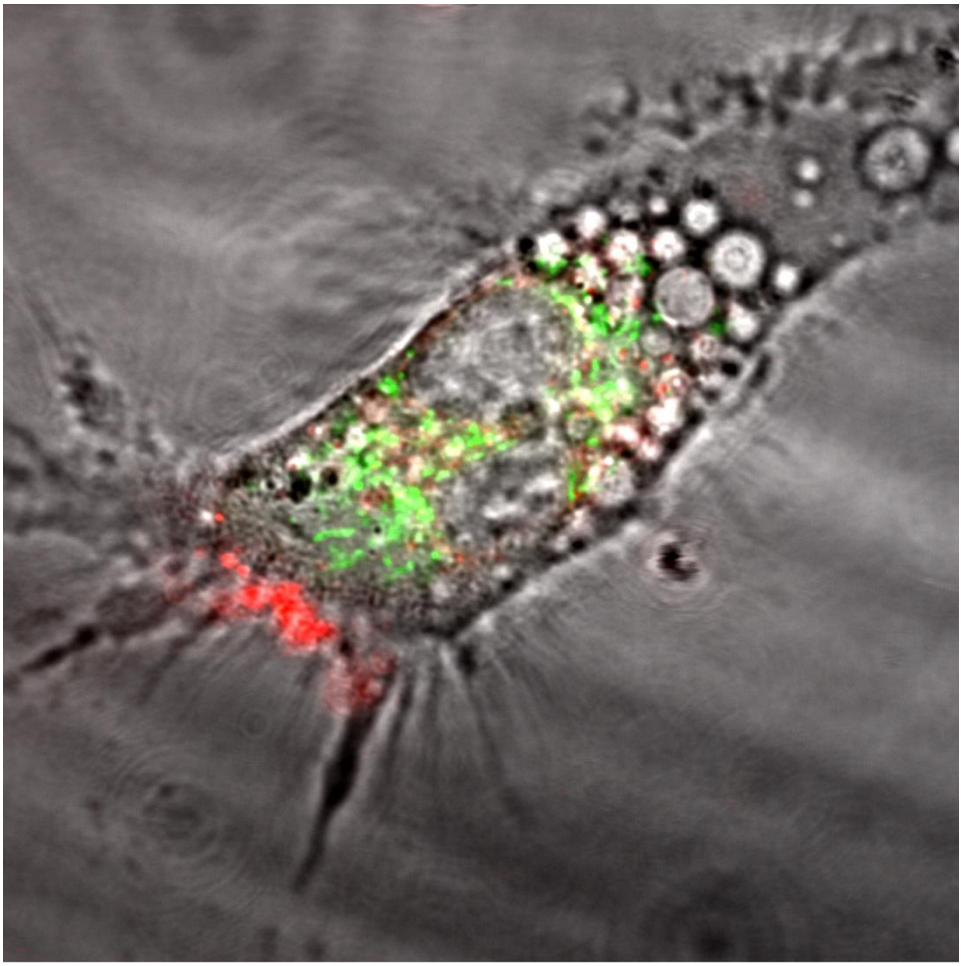

Figure 2.33, Pig monocytes stained with Mitotracker Green FM, treated with 3 μM of Rhodamine B labeled SA-D-K_6L_9-AS for live confocal imaging.

1000x. Captured at 30min after monitoring.

2.4 Conclusion

The novel D-K_6L_9 derivative SA-D-K_6L_9-SA (SALK*L*LK*K*L*LK*KLL*K*LLAS) was synthesized, purified, and characterized. The design of this therapeutic peptide against solid tumors permitted the elucidation of its secondary structure for the first time. SALK*L*LK*K*L*LK*KLL*K*LLAS is a distorted alpha-helix. Confocal experiments have confirmed that SA-D-K_6L_9-SA interacts with cell membranes according to the carpet mechanism. SA-D-K_6L_9-SA showed increased efficacy against Gl26 cells and pig monocytes (control cell culture), when compared with D-K_6L_9. We attribute this finding to the ability of SA-D-K_6L_9-SA to enter the cells' interior, which is not known for D-K_6L_9. Furthermore, confocal co-staining experiments have shown that SA-D-K_6L_9-SA can target mitochondrial membranes. Based on this observation, it is our paradigm that SA-D-K_6L_9-SA can cause both, necrosis by partially dissolving cell membranes, and apoptosis by means of targeting the mitochondria. Due to the activation of both pathways towards cell death, SA-D-K_6L_9-SA can be more effective against cancer and healthy eukaryotic cells.

2.5 References

1. https://www.ncbi.nlm.nih.gov/pubmedhealth/PMHT0015630/.

2. Siegel, R. L.; Miller, K. D.; Jemal, A., Cancer statistics, 2018. *CA: A Cancer Journal for Clinicians* **2018,** *68* (1), 7-30.

3. http://www.cancer.gov/about-cancer/understanding/what-is-cancer.

4. Hanahan, D.; Weinberg, R. A., Hallmarks of cancer: the next generation. *Cell (Cambridge, MA, U. S.)* **2011,** *144* (5), 646-674.

5. Hanahan, D.; Coussens, L. M., Accessories to the Crime: Functions of Cells Recruited to the Tumor Microenvironment. *Cancer Cell* **2012,** *21* (3), 309-322.

6. https://cancerstaging.org/Pages/default.aspx.

7. McPhail, S.; Johnson, S.; Greenberg, D.; Peake, M.; Rous, B., Stage at diagnosis and early mortality from cancer in England. *British Journal Of Cancer* **2015,** *112*, S108.

8. Jha, S.; Sharma, P. K.; Malviya, R., Hyperthermia: Role and Risk Factor for Cancer Treatment. *Achievements in the Life Sciences* **2016,** *10* (2), 161-167.

9. Dabrowski, J. M.; Arnaut, L. G., Photodynamic therapy (PDT) of cancer: from local to systemic treatment. *Photochem. Photobiol. Sci.* **2015,** *14* (10), 1765-1780.

10. Abadeer, N. S.; Murphy, C. J., Recent Progress in Cancer Thermal Therapy Using Gold Nanoparticles. *J. Phys. Chem. C* **2016,** *120* (9), 4691-4716.

11. Ye, Z.; Li, Z.; Jin, H.; Qian, Q., Therapeutic cancer vaccines. *Adv. Exp. Med. Biol.* **2016,** *909* (Progress in Cancer Immunotherapy), 139-167.

12. DeVita, V. T.; Chu, E., A history of cancer chemotherapy. *Cancer research* **2008,** *68* (21), 8643-8653.

13. Burugu, S.; Dancsok, A. R.; Nielsen, T. O., Emerging targets in cancer immunotherapy. *Semin. Cancer Biol.* **2017**, Ahead of Print.

14. Dempke, W. C. M.; Fenchel, K.; Uciechowski, P.; Dale, S. P., Second- and third-generation drugs for immuno-oncology treatment-The more the better? *Eur. J. Cancer* **2017,** *74*, 55-72.

15. Stoll, G.; Ma, Y.; Yang, H.; Kepp, O.; Zitvogel, L.; Kroemer, G., Pro-necrotic molecules impact local immunosurveillance in human breast cancer. *OncoImmunology* **2017,** *6* (4), e1299302/1-e1299302/8.

16. Chen, Daniel S.; Mellman, I., Oncology Meets Immunology: The Cancer-Immunity Cycle. *Immunity* **2013,** *39* (1), 1-10.
17. Dunn, G. P.; Bruce, A. T.; Ikeda, H.; Old, L. J.; Schreiber, R. D., Cancer immunoediting: from immunosurveillance to tumor escape. *Nature immunology* **2002,** *3* (11), 991.
18. Gamrekelashvili, J.; Greten, T. F.; Korangy, F., Immunogenicity of necrotic cell death. *Cell. Mol. Life Sci.* **2015,** *72* (2), 273-283.
19. Fink, S. L.; Cookson, B. T., Apoptosis, pyroptosis, and necrosis: mechanistic description of dead and dying eukaryotic cells. *Infect. Immun.* **2005,** *73* (4), 1907-1916.
20. Zhang, J. Y., Apoptosis-based anticancer drugs. *Nat Rev Drug Discov* **2002,** *1* (2), 101-2.
21. Hahn, W. C.; Meyerson, M., Telomerase activation, cellular immortalization and cancer. *Ann. Med. (Helsinki, Finl.)* **2001,** *33* (2), 123-129.
22. Papo, N.; Oren, Z.; Pag, U.; Sahl, H.-G.; Shai, Y., The consequence of sequence alteration of an amphipathic alpha-helical antimicrobial peptide and its diastereomers. *J. Biol. Chem.* **2002,** *277* (37), 33913-33921.
23. Braunstein, A.; Papo, N.; Shai, Y., In vitro activity and potency of an intravenously injected antimicrobial peptide and its DL amino acid analog in mice infected with bacteria. *Antimicrobial agents and chemotherapy* **2004,** *48* (8), 3127-3129.
24. Papo, N.; Seger, D.; Makovitzki, A.; Kalchenko, V.; Eshhar, Z.; Degani, H.; Shai, Y., Inhibition of tumor growth and elimination of multiple metastases in human prostate and breast xenografts by systemic inoculation of a host defense–like lytic peptide. *Cancer research* **2006,** *66* (10), 5371-5378.
25. Papo, N.; Braunstein, A.; Eshhar, Z.; Shai, Y., Suppression of human prostate tumor growth in mice by a cytolytic d-, l-amino acid peptide: membrane lysis, increased necrosis, and inhibition of prostate-specific antigen secretion. *Cancer research* **2004,** *64* (16), 5779-5786.
26. Makovitzki, A.; Fink, A.; Shai, Y., Suppression of human solid tumor growth in mice by intratumor and systemic inoculation of histidine-rich and pH-dependent host defense–like lytic peptides. *Cancer research* **2009,** *69* (8), 3458-3463.
27. Silhavy, T. J.; Kahne, D.; Walker, S., The bacterial cell envelope. *Cold Spring Harb Perspect Biol* **2010,** *2* (5), a000414.

28. Birge, R.; Boeltz, S.; Kumar, S.; Carlson, J.; Wanderley, J.; Calianese, D.; Barcinski, M.; Brekken, R.; Huang, X.; Hutchins, J., Phosphatidylserine is a global immunosuppressive signal in efferocytosis, infectious disease, and cancer. *Cell death and differentiation* **2016,** *23* (6), 962.
29. Chen, B.; Le, W.; Wang, Y.; Li, Z.; Wang, D.; Ren, L.; Lin, L.; Cui, S.; Hu, J. J.; Hu, Y., Targeting negative surface charges of cancer cells by multifunctional nanoprobes. *Theranostics* **2016,** *6* (11), 1887.
30. Liberti, M. V.; Locasale, J. W., The Warburg Effect: How Does it Benefit Cancer Cells? *Trends in Biochemical Sciences 41* (3), 211-218.
31. Melo, M. N.; Ferre, R.; Castanho, M. A. R. B., Antimicrobial peptides: linking partition, activity and high membrane-bound concentrations. *Nat. Rev. Microbiol.* **2009,** *7* (3), 245-250.
32. Baumann, G.; Mueller, P., Molecular model of membrane excitability. *J. Supramol. Struct.* **1974,** *2* (5-6), 538-57.
33. Ludtke, S. J.; He, K.; Heller, W. T.; Harroun, T. A.; Yang, L.; Huang, H. W., Membrane Pores Induced by Magainin. *Biochemistry* **1996,** *35* (43), 13723-13728.
34. Leontiadou, H.; Mark, A. E.; Marrink, S. J., Antimicrobial Peptides in Action. *J. Am. Chem. Soc.* **2006,** *128* (37), 12156-12161.
35. Pouny, Y.; Rapaport, D.; Mor, A.; Nicolas, P.; Shai, Y., Interaction of antimicrobial dermaseptin and its fluorescently labeled analogs with phospholipid membranes. *Biochemistry* **1992,** *31* (49), 12416-23.
36. Rosenholm, J. M.; Mamaeva, V.; Sahlgren, C.; Linden, M., Nanoparticles in targeted cancer therapy: mesoporous silica nanoparticles entering preclinical development stage. *Nanomedicine (London, U. K.)* **2012,** *7* (1), 111-120.
37. Pasqua, L.; Leggio, A.; Sisci, D.; Ando, S.; Morelli, C., Mesoporous Silica Nanoparticles in Cancer Therapy: Relevance of the Targeting Function. *Mini Rev Med Chem* **2016,** *16* (9), 743-53.
38. Rachakatla, R. S.; Balivada, S.; Seo, G.-M.; Myers, C. B.; Wang, H.; Samarakoon, T. N.; Dani, R.; Pyle, M.; Kroh, F. O.; Walker, B.; Leaym, X.; Koper, O. B.; Chikan, V.; Bossmann, S. H.; Tamura, M.; Troyer, D. L., Attenuation of Mouse Melanoma by A/C Magnetic Field after Delivery of Bi-Magnetic Nanoparticles by Neural Progenitor Cells. *ACS Nano* **2010,** *4* (12), 7093-7104.
39. https://web.expasy.org/cgi-bin/compute_pi/pi_tool.

40. http://osddlinux.osdd.net/raghava/pepstrmod/d_ss_upload.php.

41. Hancock, R. E. W.; Haney, E. F.; Gill, E. E., The immunology of host defence peptides: beyond antimicrobial activity. *Nat. Rev. Immunol.* **2016,** *16* (5), 321-334.

42. Troyer, D., Cell-based targeting of anti-cancer nanotherapy to tumors. *J. Cancer Sci. Ther.* **2013,** *5* (4), 142-143.

43. Ohta, N.; Kawabata, A.; Uppalapati, D.; Ishiguro, S.; Troyer, D.; Tamura, M. In *Umbilical cord matrix stem cells for cytotherapy of breast cancer*, Wiley-Blackwell: 2013; pp 113-126.

44. Wang, H.; Yapa, A. S.; Kariyawasam, N. L.; Shrestha, T. B.; Kalubowilage, M.; Wendel, S. O.; Yu, J.; Pyle, M.; Basel, M. T.; Malalasekera, A. P.; Toledo, Y.; Ortega, R.; Thapa, P. S.; Huang, H.; Sun, S. X.; Smith, P. E.; Troyer, D. L.; Bossmann, S. H., Rationally designed peptide nanosponges for cell-based cancer therapy. *Nanomedicine (N. Y., NY, U. S.)* **2017,** *13* (8), 2555-2564.

45. Coin, I.; Beyermann, M.; Bienert, M., Solid-phase peptide synthesis: from standard procedures to the synthesis of difficult sequences. *Nat. Protoc.* **2007,** *2* (12), 3247-3256.

46. http://www.dtp.nci.nih.gov/.

47. Ourednik, J.; Ourednik, V.; Lynch, W. P.; Schachner, M.; Snyder, E. Y., Neural stem cells display an inherent mechanism for rescuing dysfunctional neurons. *Nat. Biotechnol.* **2002,** *20* (11), 1103-1110.

48. Stockert, J. C.; Blazquez-Castro, A.; Canete, M.; Horobin, R. W.; Villanueva, A., MTT assay for cell viability: Intracellular localization of the formazan product is in lipid droplets. *Acta Histochem.* **2012,** *114* (8), 785-796.

49. https://www.graphpad.com/support/prism-5-updates/.

50. https://www.cgl.ucsf.edu/home/sparky/.

51. http://www.protein-nmr.org.uk/general/software/structure-calculation/.

52. http://www.ks.uiuc.edu/Research/vmd/current/.

53. Reynolds, W. F.; Enriquez, R. G., Choosing the Best Pulse Sequences, Acquisition Parameters, Postacquisition Processing Strategies, and Probes for Natural Product Structure Elucidation by NMR Spectroscopy. *J. Nat. Prod.* **2002,** *65* (2), 221-244.

54. https://www.thermofisher.com/order/catalog/product/62249.

55. Tong, W.; Welsh, W. J.; Shi, L.; Fang, H.; Perkins, R., Structure-activity relationship approaches and applications. *Environ Toxicol Chem* **2003,** *22* (8), 1680-95.

56. Segev-Zarko, L.; Saar-Dover, R.; Brumfeld, V.; Mangoni, M. L.; Shai, Y., Mechanisms of biofilm inhibition and degradation by antimicrobial peptides. *Biochem. J.* **2015,** *468* (2), 259-270.

57. http://www.bmrb.wisc.edu/ref_info/statful.htm.

58. http://schmieder.fmp-berlin.info/teaching/educational_scripts/aminoacid_nomenclature.htm.

59. Wuthrich, K., *NMR of proteins and nucleic acids*. Wiley: 1986.

60. Lopez Arbeloa, F.; Ruiz Ojeda, P.; Lopez Arbeloa, I., Fluorescence self-quenching of the molecular forms of Rhodamine B in aqueous and ethanolic solutions. *J. Lumin.* **1989,** *44* (1-2), 105-12.

61. Karstens, T.; Kobs, K., Rhodamine B and rhodamine 101 as reference substances for fluorescence quantum yield measurements. *J. Phys. Chem.* **1980,** *84* (14), 1871-2.

62. Presley, A. D.; Fuller, K. M.; Arriaga, E. A., MitoTracker Green labeling of mitochondrial proteins and their subsequent analysis by capillary electrophoresis with laser-induced fluorescence detection. *J. Chromatogr. B: Anal. Technol. Biomed. Life Sci.* **2003,** *793* (1), 141-150.

63. Heit, B.; Yeung, T.; Grinstein, S., Changes in mitochondrial surface charge mediate recruitment of signaling molecules during apoptosis. *American Journal of Physiology-Cell Physiology* **2010,** *300* (1), C33-C41.

Chapter 3 - Mesoporous Silica (Nano)Particles as Delivery Agents for SA-D-K_6L_9-SA

I would like to thank Marla Pyle and Dr. Tej B. Shrestha in the group of Dr. Troyer, who have collaborated with me when performing the cell experiments. Dr. Shrestha also performed the TEM imaging at The University of Kansas, in collaboration with Dr. Prem Thapa. I also would like to thank Dr. Hongwang Wang and Lauren Chlebanoswski for sharing their expertise in MSN synthesis with me. The designer polysilazane copolymer that is used as a gatekeeper was synthesized by Dr. Hongwang Wang.

3.1 Introduction

3.1.1 State-of-the-art of Mesoporous Silica Particles in Drug Delivery

Mesoporous silica nanospheres (MSNs)[1-2] have been intensely discussed as drug delivery devices since the turn of the millennium, as evidenced by more than 5000 journal articles and reviews that have been published since January 01, 2000 in SciFinder. Today, there is a history of *in-vitro* studies that demonstrated that MSNs can be designed to exhibit stimulus-responsive release of drugs, suitable cellular uptake, as well as cell-specific targeting.[3] Furthermore, MSN are able to deliver relatively large payloads of a broad variety of therapeutic agents, ranging from hydrophobic drug molecules to therapeutic peptides and imaging agents. [4-5] The reason why this research is concerned with the development and animal testing of novel Mesoporous Silica Nanospheres for Drug Delivery is that, in spite of all reported successes, MSN have not performed exceedingly well in meaningful animal models.[3, 6] (Studies of MSN in other than in immune-compromised xenograft models are rare.[6]) As expressed in a recent review by Ch.

Bräuchle et al. *"Researchers are still faced with many challenges, especially in-vivo applicable stimuli-responsive release mechanisms, targeting specificity, and biosafety issues, which need to be fully understood to achieve efficient and safe drug delivery. A complete understanding of the mechanisms for intracellular uptake, trafficking, and the fate of multifunctional MSN in the body would be highly desirable. Up to now, only a few in vivo studies of the pharmacokinetics of multifunctional MSN including biodistribution, biodegradation, and excretion and clearance have been performed, and additional work in this area is clearly needed."*[7]

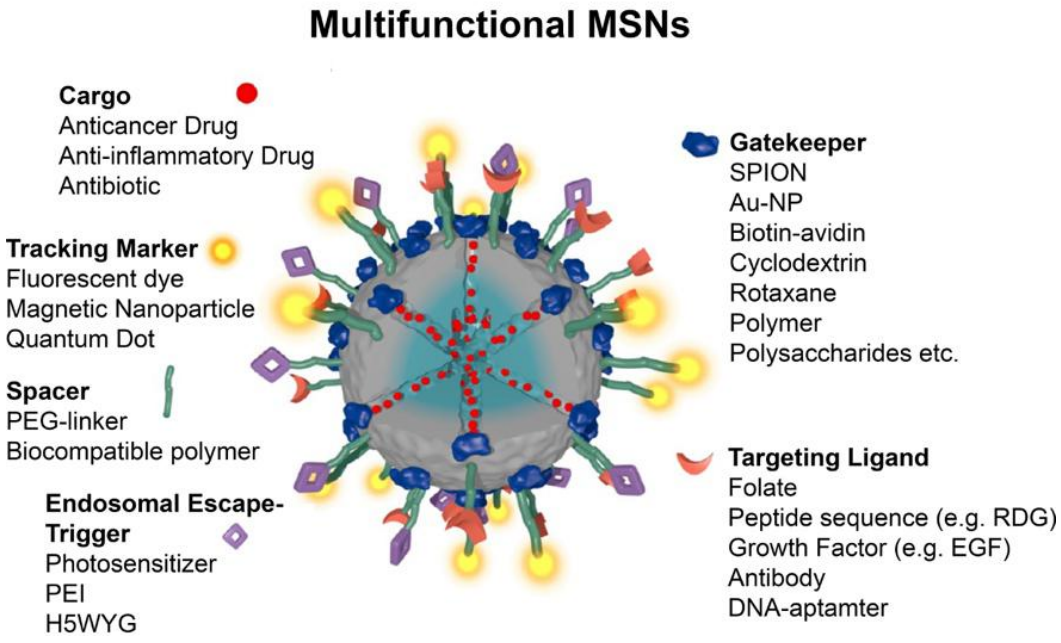

Scheme 3.1, State-of-the-Art of Multifunc-tional Mesoporous Silica Nanospheres (MSN).
PEG: polyethylene glycol; PEI: polyethylene imine; H5WYG: membrane permeating peptide at slightly acidic pH; SPION: superparamagnetic iron oxide nanoparticle; according to reference. [7]

3.1.2 Design Rationale

Scheme 3.1 summarizes the currently available MSNs technology, which is described in detail in several recent reviews.[3-5, 7] The design of the Mesoporous Silica Nano-spheres for Drug Delivery that has been realized here, addresses the inadequacies of current designs with respect

to drug transport to tumor and metastases. MSN designed in this study are designed for delivery using neuronal progenitor cells[8] as transport modality. Strictly non-toxic materials have to be selected for the design of the MSN, because a cell-based delivery strategy depends on the survival of the transport cell during the voyage to the tumor. “Gatekeepers” have the crucial function of retaining cytotoxic anticancer drugs within the mesoporous silica network during transport to the tumor cells.[7] If cell-based transport is attempted, leakage has to be reduced to less than 1% to prevent significant cell death while the payload is being transported to the tumor within 72h. To the best of our knowledge, such efficient gatekeepers have not been constructed to date.

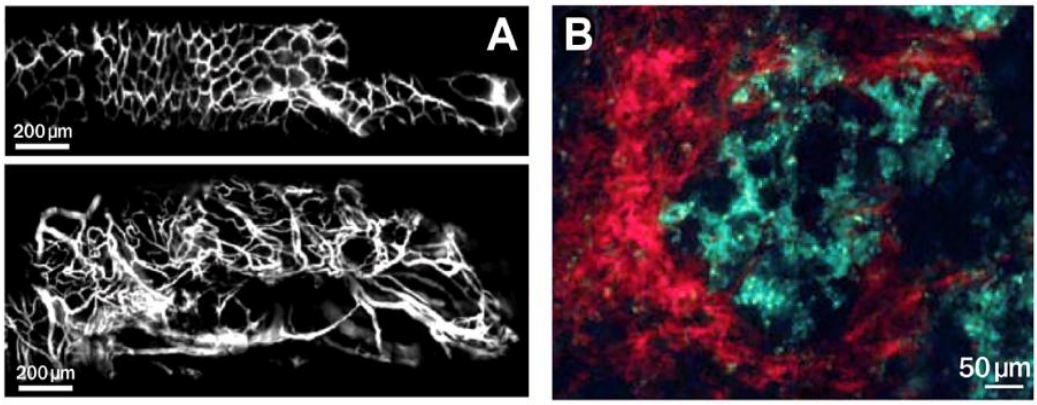

Figure 3.1, A: Longitudinal fluorescence imaging of normal (top) and tumor (bottom) colon tissue in a floxed Apc mouse. B: Diffusion of nanoparticles (green) in the tumor interstitium depends on collagen content (red). At high collagen regions the concentration of nanoparticle (d = 150 nm) is low, and vice versa.
Adapted from reference 9.

3.1.2.1 Delivery Mechanisms, State-of-the-Art

Effective performance of liposomes, MSN, and other nanoscopic and microscopic objects *in-vivo* requires both: bypassing the macrophages of the reticuloendothelial system (RES) located in the spleen, and avoiding rapid filtration through the renal glomerulus into the urine.[10-11] Although counter-measures have been developed, such as stealth coatings, which decrease

uptake by the RES and renal clearance, the resulting spherical stealth MSN are still being removed from the bloodstream within 2h (diameter: 360nm) to 8h (diameter: 80nm).[11] Enhanced circulation times have been observed for MSN-nanorods. However, the clearance times of MSN-nanorods from mouse tissues increased significantly as well, which may result in enhanced toxicity.[12] The enhanced uptake with increased size is noteworthy, because it indicates increased phagocytotic activity of the macrophages of the RES. All nanostructures larger than approx. 6 nm in diameter avoid renal clearance.[10]

Very recently, Stirland et al. have discovered that dynamic extravasation events occur on the scale of microns in xenograft tissue. Multiple colocalization analyses confirmed that silica nanoparticles separated into different dose administrations did not accumulate in the same location.[13] There is a growing sense of urgency in developing effective targeted nanotherapies for clinical trials. However, heterogeneous distribution of therapeutics due to physiologic barriers attributable to high interstitial fluid pressures and the formidable physical barrier imposed by tumor stroma remains a major issue[9]. According to a current paradigm in drug delivery, classic chemotherapy can deliver less than five percent of the chemotherapeutic drugs into tumors and metastases, whereas nanotherapeutic delivery is capable of increasing this percentage to approx. 10 to 20 percent.[9] Active targeting increases the uptake of the nanoformulation by several tumor cell types, but is only achievable after extravasation has taken place.[9] Therefore, active targeting will hardly be able to surpass the existing delivery barriers.

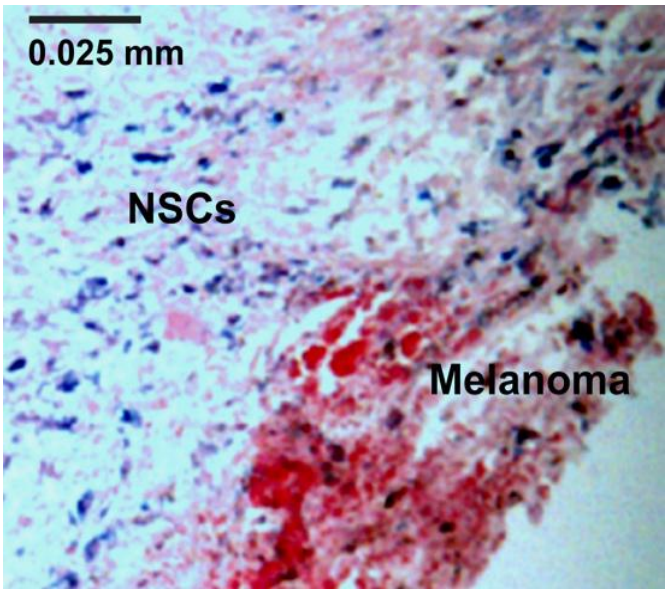

Figure 3.2, C17.2 Neural Progenitor Cells (blue) home to B16F10 Melanomas (red and black colors) in Black Mice.[8]

The Troyer and Bossmann groups have demonstrated that **stem cell- and defensive cell-mediated delivery** *of nanoparticles[8, 14] and drugs[15-16] to tumors and infected sites[17] is very efficient and permits treating cancer in mice with significantly lower doses, thus minimizing collateral effects.* According to the drug delivery paradigm quoted above, cell-based therapy may be capable of delivering more than 50 percent of chemotherapeutic drugs to tumor tissue. MSN have been already successfully used to tag neural progenitor cells and mesenchymal stem cells with MRI and fluorescence labels for the purpose of cell-tracking.[18-22]

Chen, Lesniak et al. have employed pH-sensitive doxorubicin-loaded mesoporous silica nanoparticles (MSN-Dox) in neural stem cells for the treatment of an orthotopic U87 xenograft glioma mouse model.[23] Their work has demonstrated both, the feasibility of transporting an anticancer drug bound to MSNs to the site of solid tumors, as well as the cytotoxicity of doxorubicin that could not be prevented from leaching out of the MSN framework.

3.1.2.2 Triggering Mechanism, State-of-the-Art

The removal of the gatekeepers and subsequent release of the MSN's payload can be achieved by means of **external stimuli** [4, 7]: Examples for **Molecular Pore Gating** are the photochemical cleavage of thymidine dimers[24], the dethreading of cyclodextrines[25], cucurbit[6]uril[26] or nitroveratryl carbamate.[27] **Surface Coating** of MSNs was performed by polymer shells[28] and supported lipid bilayers.[29] All of these applications require UV/Vis light, which make them difficult to apply for the treatment of deep-seated tumors.[30] Surface coating of MSN by means of aptamer DNA shells [31] requires photo-thermal dehybridization, which is somewhat advantageous but still not suitable for treating deep-seated tumors. **Particle Pore Gating** can be achieved by combining a superparamagnetic nanoparticle (e.g. SPION[32]) in an A/C-magnetic or microwave-field or a plasmonic gold nanoparticle[33] with a bond, molecule or macromolecule that can be thermally cleaved[7] (e.g. cleavage of boroesters, dusilfides, or DNA[34]) or a polymer that undergoes a phase transition upon heating (e.g. a poly-NIPAM copolymer[35]).

Internal stimuli[4-7]are advantageous when combined with cell-based delivery, because they work without the exact knowledge where tumors and especially metastases are located. Neural stem cells will migrate to tumors and metastases, because the latter attract them using cytokines.[36] The most widely explored internal stimulus is the use of **pH-sensitive**-bonds[37-38], [2]pseudorotaxanes and other mechanical gate-keepers[39], and (bio)polymers.[40] pH-sensitive bonds take advantage of the decreased pH in the interstitium of many solid tumors ($\leq$ 6.5 (tumor) vs. $\geq$ 7.0 (healthy tissue)).[41] It is noteworthy that pH-activation is a feasible trigger mechanism in larger (primary) tumors, whereas the interstitium of emerging metastases is usually not sufficiently acidic to reliably trigger the release of a drug. However, the successful treatment of (emerging) metastases is mandatory for a successful chemotherapy against higher stage solid

tumors, considering that usually the patient is killed by the metastases and not the primary tumor. Another extensively applied internal stimulus is the use of **disulfide linkers** that are **reductively cleaved** by the glutathione in the cytoplasm of mammalian cells.[7, 42-43] Although some cancer cells lines are reported to feature high levels of glutathione[44], this strategy depends entirely on the initial uptake of the MSN, followed by endosomal escape into the cytoplasm.[45]

To date, the most reliable triggers are **enzymes** that are **overexpressed in solid tumors** and **metastases** (e.g. reductases, esterases, proteases, hydrolases).[42-50] They can be used to remove gatekeepers by cleaving their linkers[46-48], or to degrade polymers (hyaluronic acid[49], polyesters[50], starch derivatives[51], polylactose[52], and peptides[53] or organic polymers containing cleavable peptide sequences).[54] However, enzymatically triggered reactions face the intrinsic problem that numerous enzymes are present in blood.[55-56] Therefore, premature activation of the triggering mechanism can occur, resulting in systemic toxicity instead of targeted delivery.

3.1.3 Experimental Design

As already discussed, most chemotherapeutic drugs have many side effects, because they are non-specific. Therefore, drugs have to be improved by enhancing the targeting efficacy to tumor sites. Nanotechnology has dominated many fields of application, since it has been invented, especially in drug delivery.[57-59] For instance, nanoparticles have been widely used in anti-cancer drugs for different medical applications. Nanoscopic properties can be tailored to modify clearance and retention properties. Furthermore, by controlling their surface charge, better binding and uptake of nanoparticles by cells can be achieved. Moreover, by applying a coating to nanoparticles, a more stable drug formulation can be made.[57] Typical drug-delivery systems are shown in Figure 3.3.

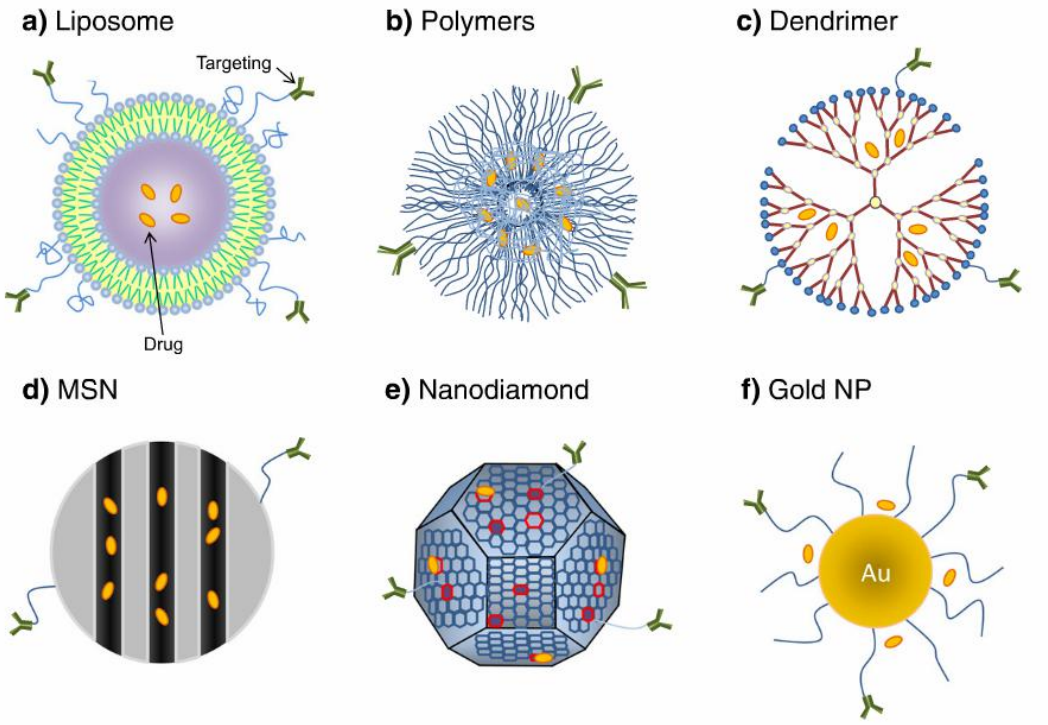

Figure 3.3, Different nanoparticles used in drug delivery systems.

Among numerous nanomaterials, nanosilica particles, especially mesoporous silica nanoparticles (MSNs), have recently become one of the most promising materials due to their unique properties. With advanced synthetic procedures, the pore size and particle size can be controlled. They range from 2 to 50nm and 10nm to micro size, respectively.[1-2] This permits tailored applications. Moreover, silica is a safe material for human bodies. It has great bio-compatibility, so no worries with side effect from the carrier itself. One more advantage is that, not only the hollow structure inside the silica particles can be used, MSNs can be functionally modified on their surfaces as well.[7, 58] Based on these considerations, MSNs can be an appropriate drug carriers to "hide" the toxic peptides. We have chosen a polysilazane as a gate-keeper, because this polymer can be biodegraded by transport cells and cancer cells alike. This permits the timed release of the MSN's payload.

The **payload** of the MSN will be comprised of the therapeutic peptide SA-D-K_6L_9-SA, which has been thoroughly described in chapter 1. The pore diameter of the silica microspheres has been adjusted to 2.0 ± 0.25 nm to accommodate this payload. As described in chapter 1, the amphiphilic oligopeptide SA-D-K_6L_9-AS (SALK*L*LK*K*L*LK*KLL*K*LLAS) depolarizes the transmembrane potential of mammalian cells and eventually lyses the cell membrane according to a carpet mechanism, leading to necrosis.[60] This strategy is capable of avoiding chemoresistance against low molecular weight chemotherapeutics, which is typical for many solid tumors.[61] Necrosis, in contrast to apoptosis, is inherently immunogenic due to rapid release of factors such as HMGB1, TNF-alpha and IL-8.[62] It has been reported that exposure to necrotic but not apoptotic tumor cells provided maturation signals to dendritic cells with resultant upregulation of maturation markers and co-stimulatory molecules with subsequent promotion of a vigorous immune response.[63] Since SA-D-K_6L_9-AS is, contrary to D-K_6L_9, capable of entering the cells and targeting the mitochondria, it is our paradigm that SA-D-K_6L_9-AS can trigger both, necrosis and apoptosis. This is in agreement with its enhanced efficacy against eukaryotic cells, compared to D-K_6L_9.

Although many D-K_6L_9 derivatives are very effective against cancer cells and are, principally, also capable of killing cancer stem cells, they do not differentiate well between cancerous and healthy cells.[64-66] Therefore, tailored delivery to tumors and metastases is mandatory. The improved therapeutic peptide SA-*D*-K_6L_9AS about 3.05 nm long and has a diameter of maximally 1.5 nm (chapter 1). Therefore, it is an excellent fit for the tunnels in the mesoporous silica microspheres, which are 2.0 ± 0.25 nm in diameter.

3.2 Materials and Methods

SA-D-K_6L_9-SA was synthesized, purified, and characterized, as described in chapter 1.

3.2.1 MSNs Synthesis

The synthesis of MSNs was performed according to a published procedure.[67] 480 mg of cetyltrimethylammonium bromide (CTAB), 4.8 ml NH_4OH (28-30%), 20 ml of ethyl acetate are added to 300 ml deionized (DI) water. The mixture is stirred at room temperature for 10 min to give a clear solution. 0.50 ml of tetraethylorthosilicate (TEOs) is added while stirring vigorously. The reaction mixture was stirred at 60 °C for 15 h, and then cooled to room temperature. The nanoparticles were further ripened for 12 h at room temperature. The resulting product was collected by centrifugation (10000 rpm, 10 min), washed with DI water twice, and then coated with a monolayer of APTES ((3-aminopropyl)triethoxysilane). The product was then washed with pure ethanol for three times. This procedure will give an average particle size of 100 ± 10 nm. Different sizes can be synthesized by means of shorter or longer reaction times at 60 °C.[68-69]

3.2.2 Peptide Loading

18.2mg of SA-D-K_6L_9-AS peptide was dissolved in 2.5ml of a mixture of acetonitrile: H_2O (1:2). 9.6mg of MSN was added to the solution. The suspension was sonicated for 20min, then shaken gently overnight. After 24h the mixture was centrifugated at 10,000 rpm, and then washed with DI water three times. The solid was lyophilized to give 6.7mg white particle solid.

3.2.3 MSN Coating with Polysilazane

The principles of polysilazane coating chemistry are shown in Figure 3.4. Designer polysilazanes are formed from (organic) dichlorosilanes in liquid NH_3.[70-72] They can be used to synthesize coatings around MSN that were previously loaded with a lytic peptide. The coating procedure comprises dispersing of loaded MSN in n-heptane under argon and addition of 5% by

weight of polysilazane to the mixture, followed by stirring at 25°C. The polysilazane coating acts as gatekeeper and prevents the leaching of the lytic peptides during extravasation of cell-mediated transport. It is noteworthy that the residual Si-H groups can react with virtually any protic (-NH, -OH, -SH, -COOH) group under formation of a covalent silicon- heteroatom bond. This alternative to classic "click" chemistry[73] is very useful when designing nanocontainers for drug delivery. When in contact with H_2O, Si-H reacts to Si-OH (silanol), making the MSN hydrophilic and negatively charged.[74]

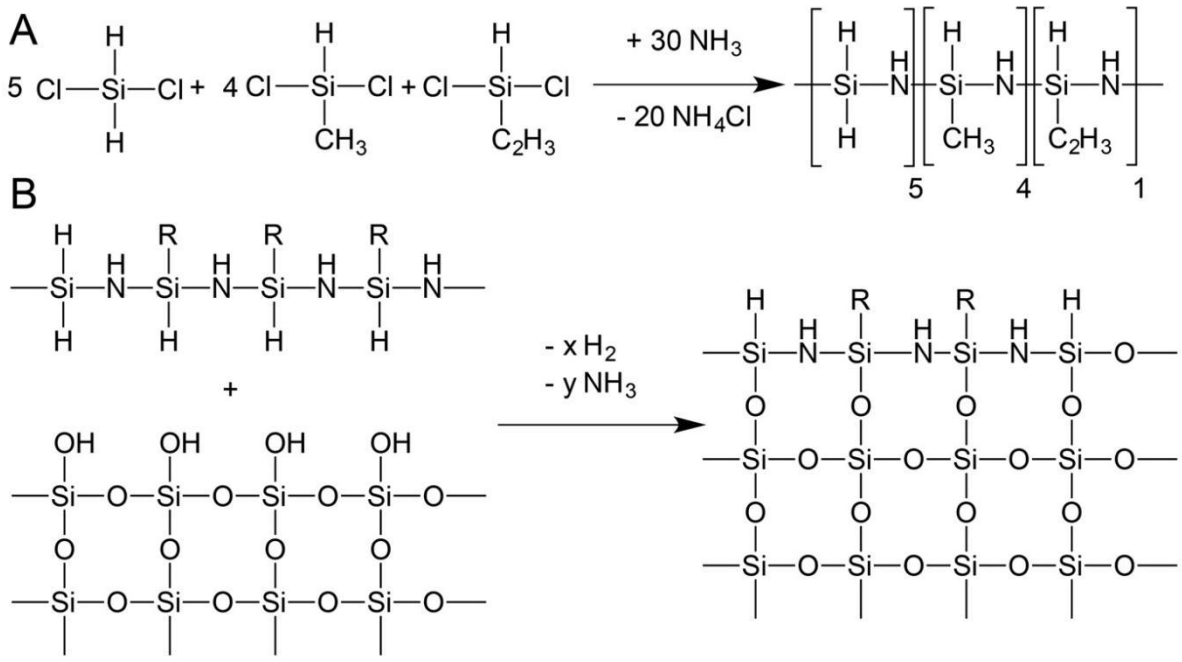

Figure 3.4, A: Formation of a statistical polysilazane copolymer from dichlorosilanes in liquid ammonia. [70-72] B: Coating of a polysiloxane (MSN) with a polysilazane.

It is noteworthy that the residual Si-H groups can react with any protic group or molecule, leading to covalent attachment. Si-H reacts with water to Si-OH (hydrophilic silanol groups).[71]

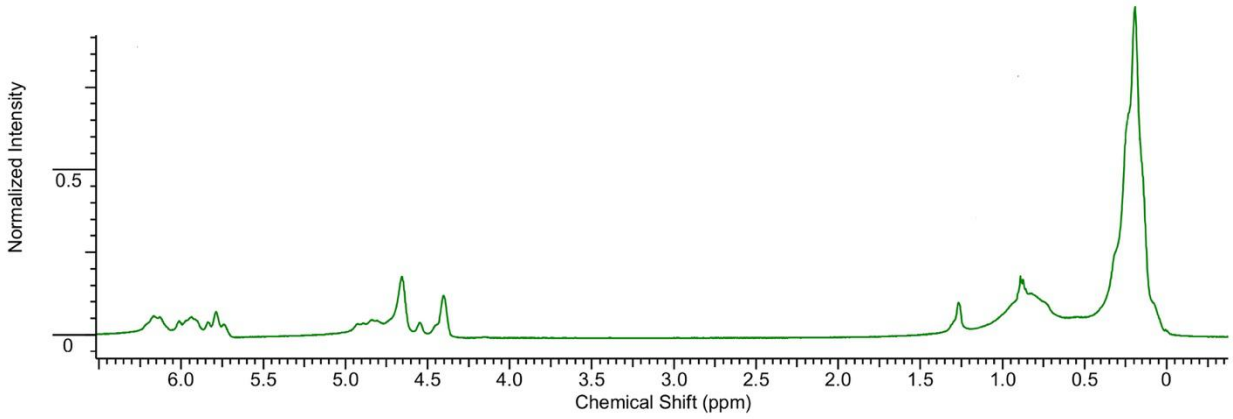

Figure 3.5, ^{1}H NMR of $[SiH_2NH]_5[SiHCH_3NH]_4[SiHC_2H_3NH]$

3.2.4 Coating Procedure of MSN with Polysilazane Designer Copolymer

6.6mg of peptide loaded MSN was added to 3.0 ml of n-hexane containing 6.0mg of polysilzane designer copolymer (see Figure 3.4 for the exact structure). The mixture was shaken gently overnight. After the reaction was completed, the mixture was centrifuged and washed twice with hexane, once with ethanol, and twice with DI water. The solid was lyophilized to give 6.2mg of write product.

3.2.5 TEM and STEM

The resulting mesoporous silica nano/microparticles were dried in high vacuum and characterized by Transmission Electron Microscopy (TEM) and Scanning Transmission Electron Microscopy (STEM). TEM and STEM characterization was performed at the Microscopy and Analytical Imaging Laboratory of The University of Kansas.[75]

3.2.6 Thermogravimetry (TGA) Measurements

1.42 mg of peptide loaded MSN was used for thermogravimetry analysis (Shimazu TGA-50). The range of temperature was selected from 25°C to 600°C. The temperature increased by 5°C per min. All samples were heated in a nitrogen atmosphere.

1.84mg of peptide loaded MSN with designer polysilazane copolymer coating was analyzed by means of TGA. The range of temperature was selected from 25°C to 800°C. The temperature increased by 5°C per min. All samples were heated in a nitrogen atmosphere.

3.2.7 MTT Assay

GL26 cells[77] were cultured in a T-25 flask in RPMI medium, which contains 10% FBS. After the flask reaches about 80% confluency, cells were re-plated on a 96-well plate with a density of 10,000/cm^2 and cultured at 37°C overnight in a cell culture incubator.

C17.2 neural progenitor cells (NPCs)[8] were a gift from Dr. V. Ourednik (Iowa State University) to Dr. Deryl L. Troyer, DVM (Kansas State University, Anatomy & Physiology). NPCs were originally developed by Dr. Evan Snyder.[78] These cells were maintained in DMEM supplemented with 10% FBS (Sigma-Aldrich), 5% horse serum (Invitrogen), 1% glutamine (Invitrogen), and 1% penicillin/streptomycin (Invitrogen). 4T1 cells[79] were cultured in the same medium and according to the same procedure. Data was processed by Graphpad Prism 5.0.[80]

3.3 Results

3.3.1 MSN Characterization

The synthesized mesoporous silica nano/microparticles were dried in high vacuum and characterized by Transmission Electron Microscopy (TEM) and Scanning Transmission Electron Microscopy (STEM). As Figure 3.6 shows, the resulting mesoporous particles have low polydispersity. Figure 3.6 shows that the final MSNs have an average particle size of about 100nm and inner channel diameters of about 5nm.

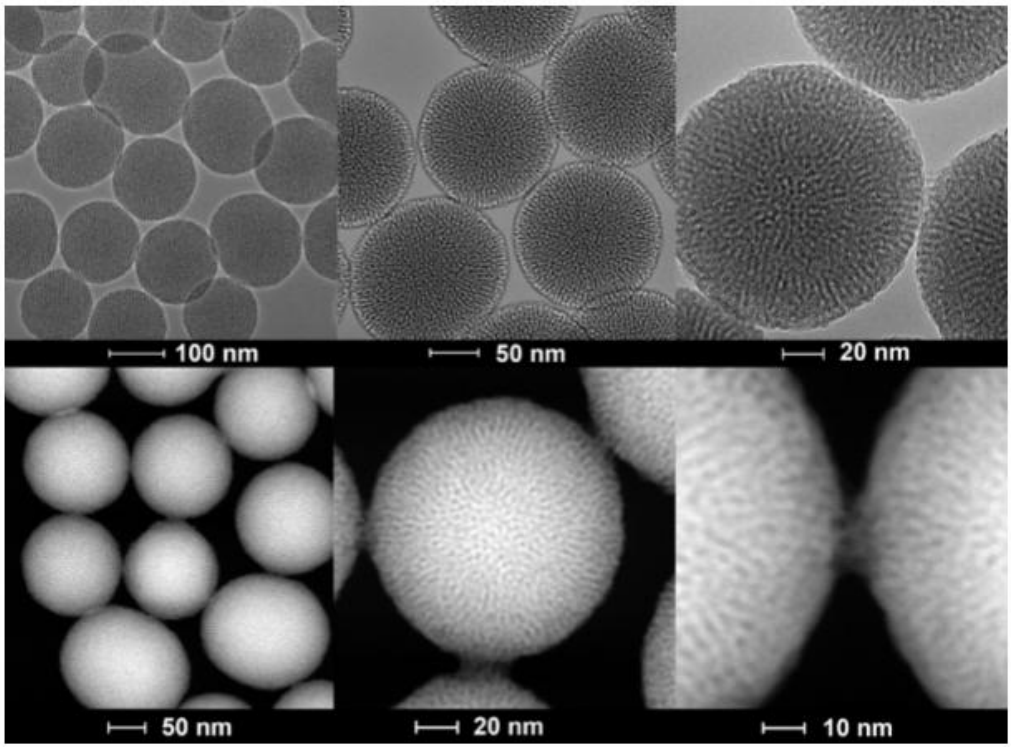

Figure 3.6, Transmission Electron Microscopy (TEM, upper row), and Scanning Transmission Electron Microscopy (STEM, lower row), of the synthesized MSNs (before peptide loading and synthesis of a gate-keeper polysilazane layer).

It is of importance for biological applications of mesoporous silica materials that the toxicity of the material mainly results from the remaining CTAB (Cetyl trimethylammonium bromide).[3-4] Therefore, we have confirmed in cell tests that the washing procedures were indeed

adequate. The exterior surface of the mesoporous silica particles is covered by a monolayer of APTES ((3-Aminopropyl) triethoxysilane). APTES acts as an anchor for the polysilazane copolymer layer that was synthesized around the MSN after loading.

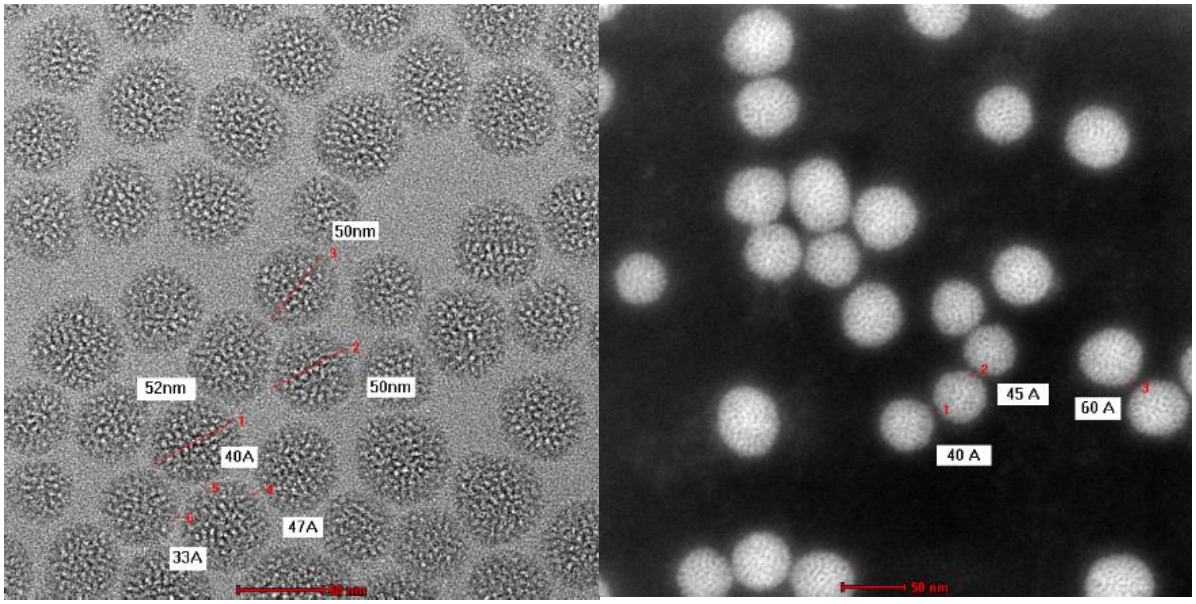

Figure 3.7, Transmission Electron Microscopy (TEM, left), and Scanning Transmission Electron Microscopy (STEM, right), of the synthesized MSNs: determination of channel diameters.

Figure 3.7 shows a TEM of MSNs that were coated with a designer polysilazane copolymer following the experimental procedure described above. The absence of clearly discernible channels is apparent. This observation is consistent with the formation of a gatekeeper layer that blocks the channels.

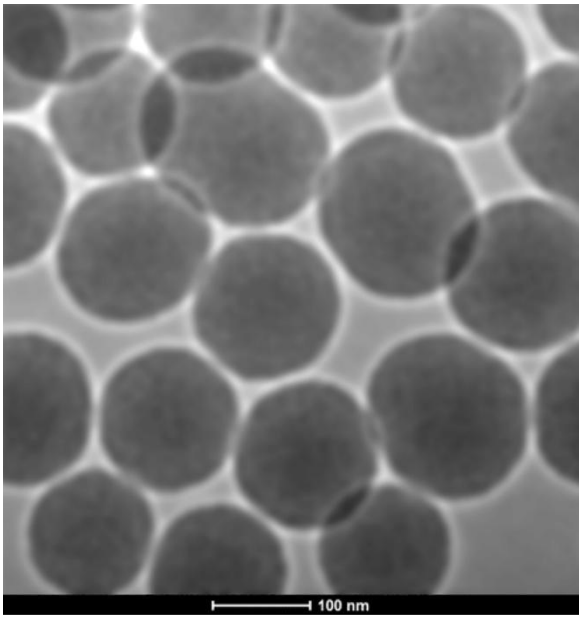

Figure 3.8, Transmission Electron Microscopy (TEM) of the synthesized MSNs after peptide loading and synthesis of a gate-keeper polysilazane layer.

The synthetic Scheme for the loading the MSNs with SA-D-K_6L_9-AS, followed by coating with a designer polysilazane copolymer, is shown below.

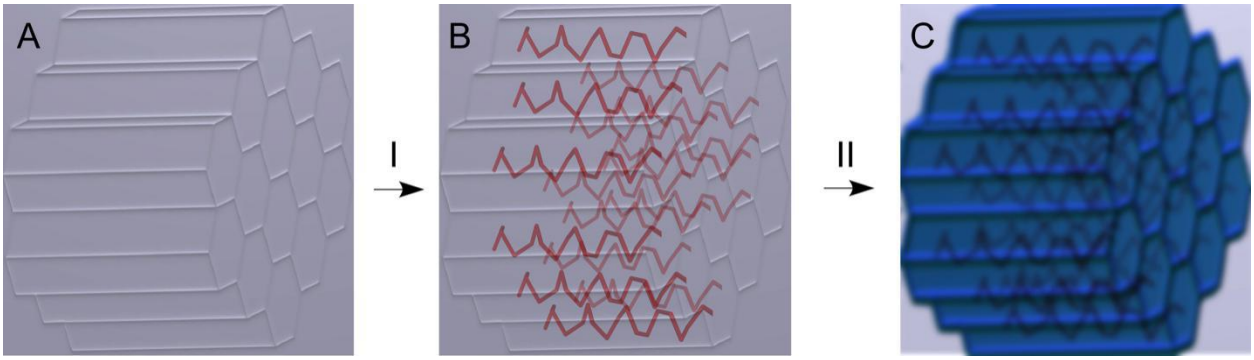

Figure 3.9, Loading the MSNs with SA-D-K_6L_9-AS, followed by coating with a designer polysilazane copolymer

I: loading of SA-D-K_6L_9-AS in acetonitrile/water (2:1), II: Coating of SA-D-K_6L_9-AS loaded MSNs with the polysilazane designer copolymer $[SiH_2NH]_5[SiHCH_3NH]_4[SiHC_2H_3NH]$.

3.3.2 Analysis of Peptide-Loaded and Polysilazane-Coated MSNs by Means of Thermogravimetry (TGA)

"Thermogravimetric Analysis is a technique in which the mass of a substance is monitored as a function of temperature or time as the sample specimen is subjected to a controlled temperature program in a controlled atmosphere."[81] Here, we have compared the weight loss of freshly synthesized MSNs that were stored in a desiccator at room temperature previous to TGA, with SA-D-K_6L_9-AS loaded MSNs that were stored under the same conditions. Both samples were slowly heated to 600 °C under nitrogen (rate: 5 °C per minute). SA-D-K_6L_9-AS also analyzed by TGA in order to verify that the polymer can be converted to gaseous products under the reaction conditions.

As shown in Figure 3.10, the loss of (mostly) absorbed water from the freshly synthesized MSNs was 10 ± 1 % at 300 °C. A slow thermal weight loss of 6± 1 % continues to 600 °C. The SA-D-K_6L_9-AS loaded MSNs shows essentially the same weight loss curve during heating, except that the loss of water is about 7 ± 1 % when after heating from RT to 300 °C. This somewhat smaller weight loss was attributed to the competition of SA-D-K_6L_9-AS and H_2O in the MSN channels. Absorption of SA-D-K_6L_9-AS is able to displace a fraction of the MSN-bound H_2O. However, SA-D-K_6L_9-AS is not as easily removable by means of heating than water. From the weight difference between the freshly synthesized MSNs and the SA-D-K_6L_9-AS loaded MSNs at 200 °C, we have estimated a loading efficacy of the MSNs with SA-D-K_6L_9-AS of 5 ± 1 %. Contrary to the MSNs, the peptide SA-D-K_6L_9-AS shows a significant decrease in mass from 150-400 °C, from 98.5% to 28.1%, which can be used in calculation for peptide loaded MSN. The percentage of peptide loaded MSN dropped from 92.1% to 86.7%. Thus, approximately 5 ± 1 %. Peptide was loaded into the MSNs. It is noteworthy that both approaches

for estimating the SA-D-K_6L_9-AS content of the MSNs lead, principally, to the same result. Therefore, we have assumed for the experiments described below that the loading of the MSNs with SA-D-K_6L_9-AS is 5 ± 1 %. This estimate is in good agreement with the literature on MSN. A recent review reports that the loading efficacy of MSNs ranges from 2% to maximally 10% for a very wide range of cargos (e.g. small molecule drugs, peptides, RNA).[82] Therefore, our findings are in the anticipated range for MSN-based delivery agents.

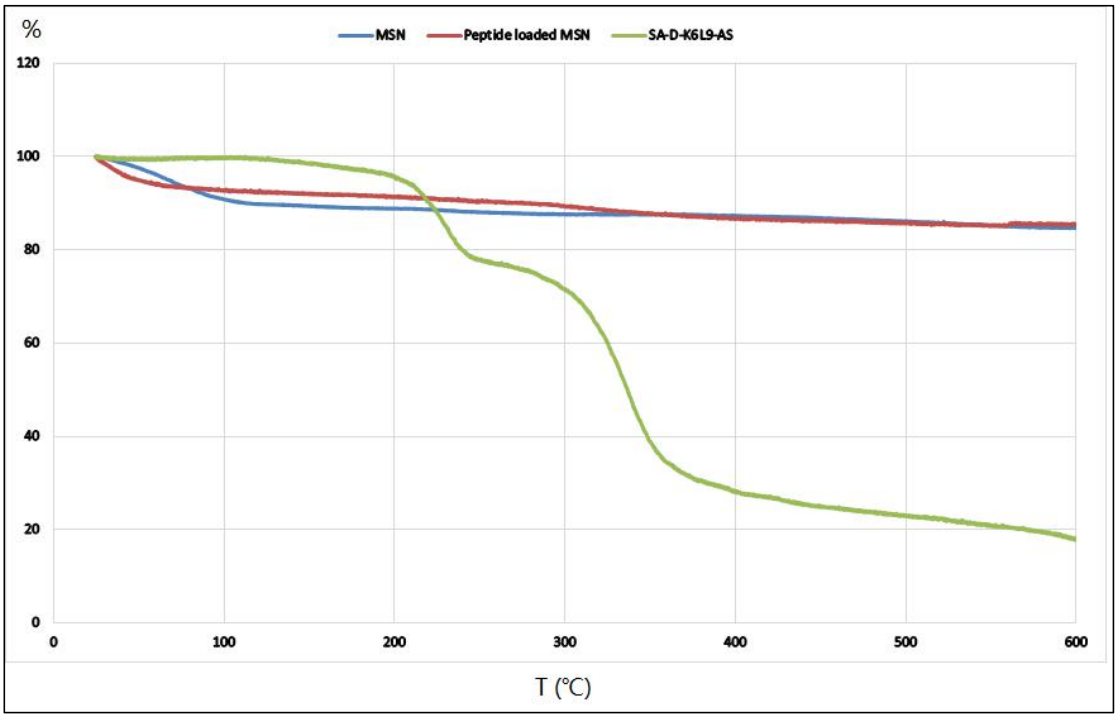

Figure 3.10, Thermogravimetry (TGA) analysis of freshly synthesized MSNs (blue curve), SA-D-K_6L_9-AS loaded MSNs (red curve) and SA-D-K_6L_9-AS peptide only.
The heating rate was 5 °C per minute. All samples were heated in a nitrogen atmosphere.

As shown in Figure 3.10 and 3.11, the weight loss of the SA-D-K_6L_9-AS loaded MSNs that were loaded with SA-D-K_6L_9-AS and then coated with the polysilazane copolymer $[SiH_2NH]_5[SiHCH_3NH]_4[SiHC_2H_3NH]$ was about 25 ± 1 %. This weight loss exceeds the 13 ± 1 % that was observed for the peptide-loaded MSNs by 12 ± 1 %. Based on this finding, we

estimate the weight of the gatekeeper layer on the peptide-loaded MSNs to 12 ± 5 %. Further studies will be conducted in the Bossmann group in order to fully understand the chemistry of the novel polysilazane designer polymers and especially the consequences of this chemistry wuth respect to weight loss during TGA.

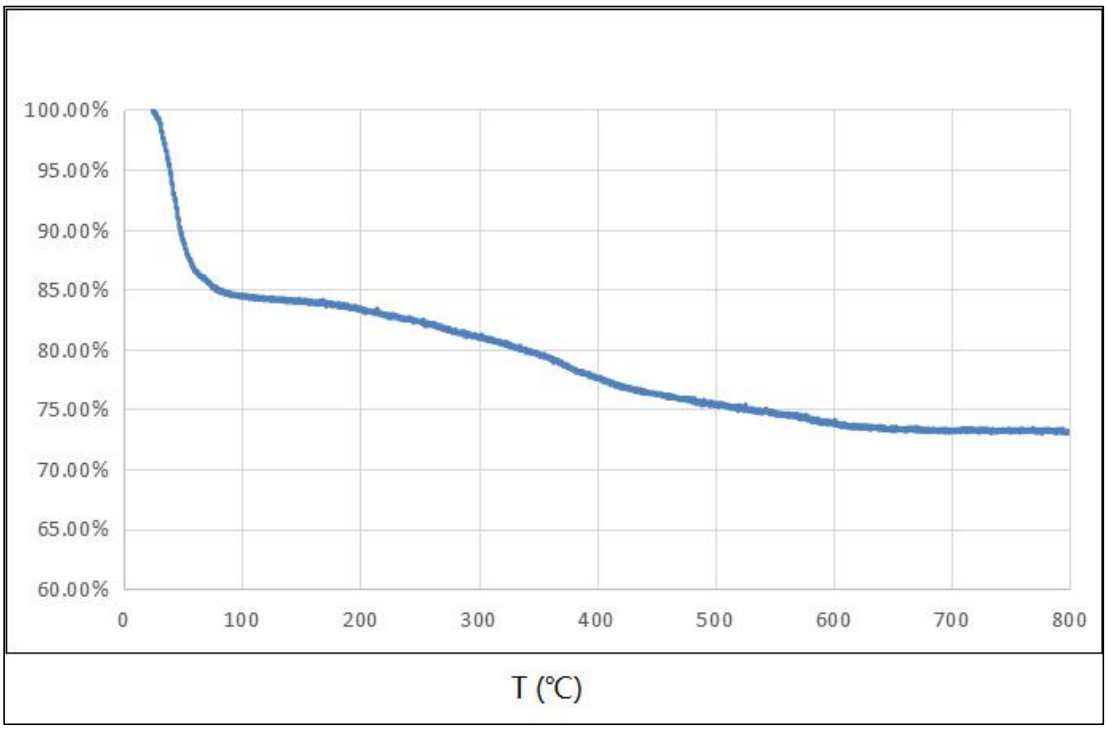

Figure 3.11, Thermogravimetry (TGA) analysis of SA-D-K_6L_9-AS loaded MSNs (blue curve) that were coated with the polysilazane copolymer $[SiH_2NH]_5[SiHCH_3NH]_4[SiHC_2H_3NH]$.
The heating rate was 5 °C per minute. The sample was heated in a nitrogen atmosphere.

3.3.3 In-Vitro Experiments

3.3.3.1 Selection of Cells

Neural Stem Cells (NSC) have been successfully used as transport cells for nanoparticles in cancer therapy. These cells actively migrate to solid tumors, following a gradient of cytokines/chemokines. [8, 83] NSC's are able to take up nanoparticles swiftly and reach tumors and metastases within days in mouse experiments. Upon arrival at the tumor, they integrate with the tumor tissue. The polymeric gatekeeper that was designed here undergoes slow hydrolysis after cellular uptake, resulting in the release of SA-K_6L_9-AS.[82] It is our working hypothesis that the release of the therapeutic peptide will begin slowly, because of the slow dissolution of the polysilazane copolymer at the MSNs surfaces. This slow release will most likely favor apoptosis of the transport cell, because SA-K_6L_9-AS targets the mitochondria and is already either in the endosome or the cytoplasm of the transport cell. Furthermore, if the MSNs are still in an endosome after endosomal uptake, SA-K_6L_9-AS will be able to facilitate endosomal escape through membrane destabilization. Once the mitochondria are targeted, apoptosis will be inevitable.[84]

For the purpose of drug delivery, apoptosis (programmed cell death in which the cell will be dissected by the caspase cascade) is the far more efficient cell death, because the bystander cells will be able to take up the formed apoptotic bodies and the MSNs.[85] In this context it is noteworthy that SA-K_6L_9-AS was designed not to exhibit a caspase cleavage motif.

Glioblastoma multiforme (GBM) tumors are grade four astrocytomas that actively recruit neural stem cells.[83] Relatively recently, attention was drawn to this form of brain cancer when Senator from Massachusetts Ted Kennedy died from glioblastoma. Of the estimated 17,000 primary brain tumors diagnosed in the United States each year, approximately 60% are gliomas.

More than half of the patients will die within a year, more than 90% within three years. Composed of a heterogenous mixture of poorly differentiated neoplastic astrocytes, glioblastomas primarily affect adults.[86] As in the initial evaluation of against gliomas, murine GL26 cells were used for the in-vitro experiments reported here.[77]

Murine 4T1 cells[79] were used as well, because they are employed in a highly metastatic breast cancer model (4T1 cells in BALB/c mice) that is studied in the Troyer and Bossmann groups at Kansas State University.[87-89] The use of 4T1 enables to broaden this study, which is based on the finding that SA-K_6L_9-AS is capable of targeting virtually any cell membrane.

3.3.3.2 Determination of Cell Viabilities by Mean of the MTT Assay

The MTT assay is a colorimetric metabolic assay.[90] Mitochondrial reductase and virtually all NAD(P)H-dependent cellular oxidoreductases are capable of reducing the tetrazolium dye MTT 3-(4,5-dimethylthiazol-2-yl)-2,5-diphenyltetrazolium bromide to formane, which has a purple color and can be detected by means of integrating the visible absorption spectroscopy from 570 nm to 650 nm.

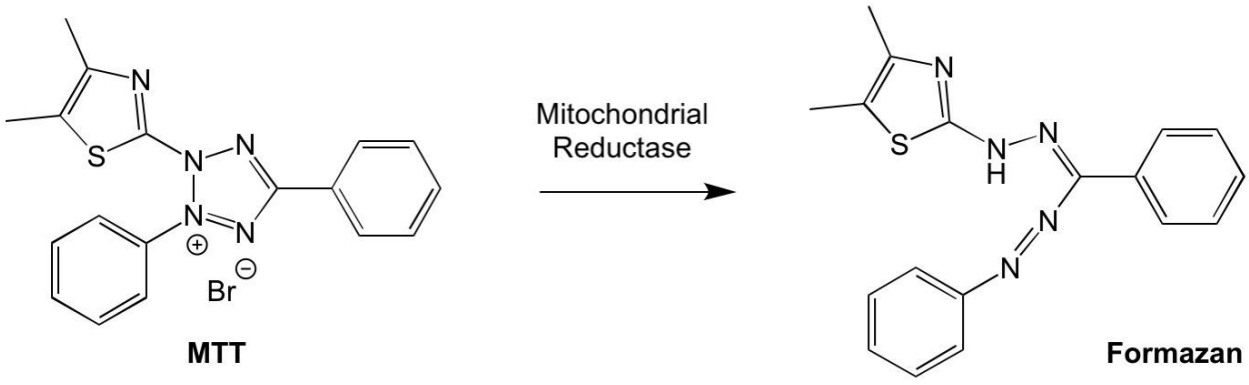

Figure 3.12, The chemistry of the MTT assay.

The paradigm of using the MTT assay is that cytotoxic materials will reduce the metabolic activity of the investigated cells. Therefore, less formazan will be formed per unit of time, compared to a group of healthy control cells.

3.3.3.2.1 Incubation of Neural Stem Cells with SA-K_6L_9-AS-loaded MSNs and Controls

The first set of experiments was concerned with the cytotoxicity of SA-K_6L_9-AS loaded MSNs to neural stem cells. NSC were incubated with various concentrations of SA-K_6L_9-AS loaded MSNs. This was followed by measuring cell viabilities vs. a group of NSC that were not exposed to SA-K_6L_9-AS loaded MSNs. The results obtained after 3h of incubation are summarized in Figure 3.13 in comparison to the cell viabilities that were observed after incubation with approx. the same concentration of SA-K_6L_9-AS, assuming 5 percent MSN loading by weight with SA-K_6L_9-AS.

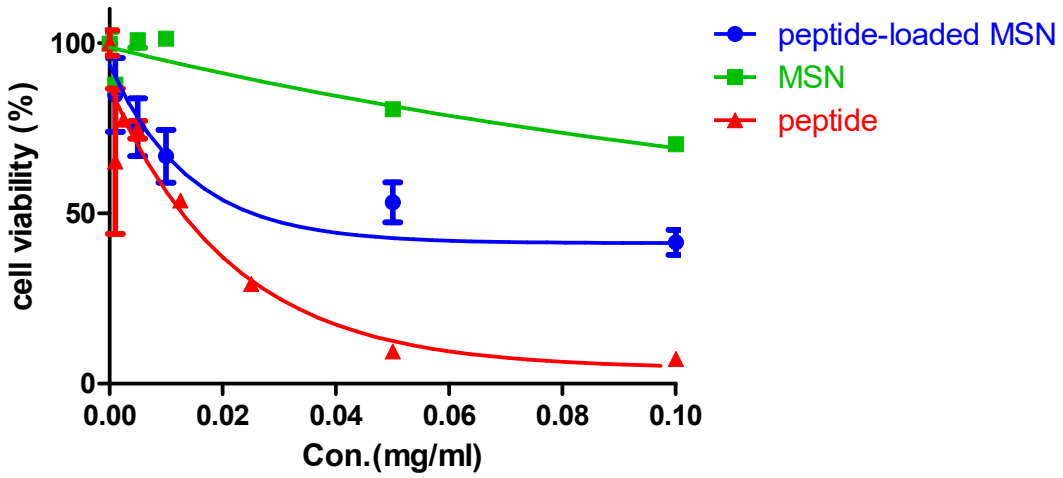

Figure 3.13, Cell viabilities of murine neural stem cells (NSC) that were incubated for 3 h with unloaded MSNs (green), SA-K_6L_9-AS loaded MSNs (blue), and free SA-K_6L_9-AS (red), as determined by means of the MTT assay.

The first important result from the cell viability studies is that MSNs were of low cytotoxicity. This finding is in agreement with the literature.[82] This makes them ideal transport containers for a wide variety of treatment modalities, including therapeutic peptide sequences. The second observation is that peptide-loaded MSNs are less cytotoxic than the same amount of free SA-K_6L_9-AS after 3h of incubation. This is a clear indication that the desorption of SA-K_6L_9-AS from the MSNs proceeds relatively slowly. It is our hypothesis that the driving force for the observed release of SA-K_6L_9-AS from the MSNs inner framework is the competitive binding of cations (mainly potassium, which has a concentration of 139 mmols in the cytosol of mammalian cells[91]) to the negatively charged silica sites. This process occurs after the SA-K_6L_9-AS-loaded MSNs were taken up by the cells, most likely via endocytosis.[92] The decrease in pH that occurs in endosomes may contribute to the release of SA-K_6L_9-AS from the MSNs. In this case, SA-K_6L_9-AS will facilitate endosomal escape by destabilizing the endosomal membrane.

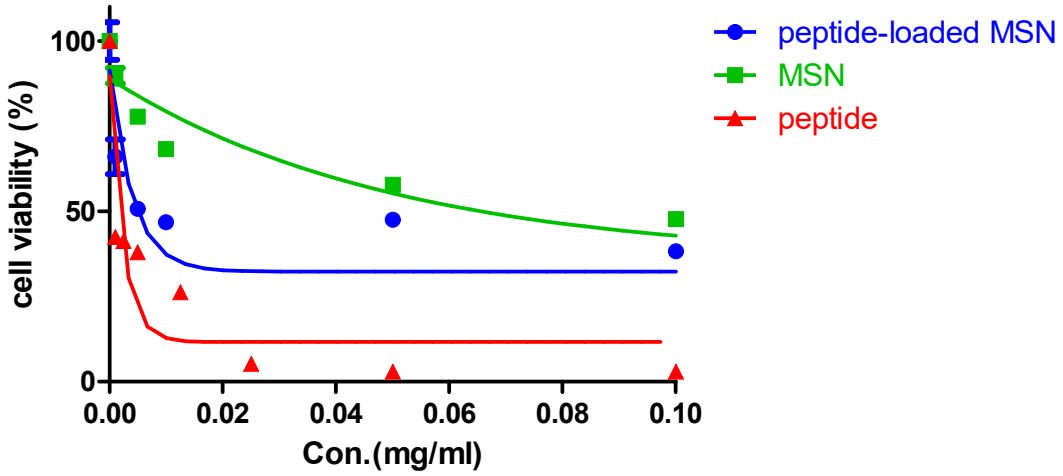

Figure 3.14, Cell viabilities of murine neural stem cells (NSC) that were incubated for 24 h with unloaded MSNs (green), SA-K_6L_9-AS loaded MSNs (blue), and free SA-K_6L_9-AS (red), as determined by means of the MTT assay.

After 24 of incubation of neural stem cells with unloaded MSNs , SA-K_6L_9-AS loaded MSNs, and free SA-K_6L_9-AS, principally the same results were obtained than after 3 h of incubation. Free MSNs exhibited relatively low cytotoxicity. Free SA-K_6L_9-AS was more effective than SA-K_6L_9-AS loaded MSNs. It appears that 24h were not sufficient to permit the complete release of SA-K_6L_9-AS from the MSNs.

3.3.3.2.2 Incubation of Murine Glioma Cells with SA-K_6L_9-AS-loaded MSNs and Controls

As shown in Figure 3.15, almost the same cytotoxicity was observed for unloaded MSNs, SA-K_6L_9-AS loaded MSNs, and free SA-K_6L_9-AS against GL26 cells, than previously observed for NSC. After 3h of incubation, unloaded MSN were even less toxic for GL26 cells, compared to NSC. Also in this case, SA-K_6L_9-AS loaded MSNs were less efficient against GL26 cells than free SA-K_6L_9-AS. This finding is in agreement with the results described in chapter 1: SA-K_6L_9-AS exhibits universal toxicity against virtually all mammalian cell types.

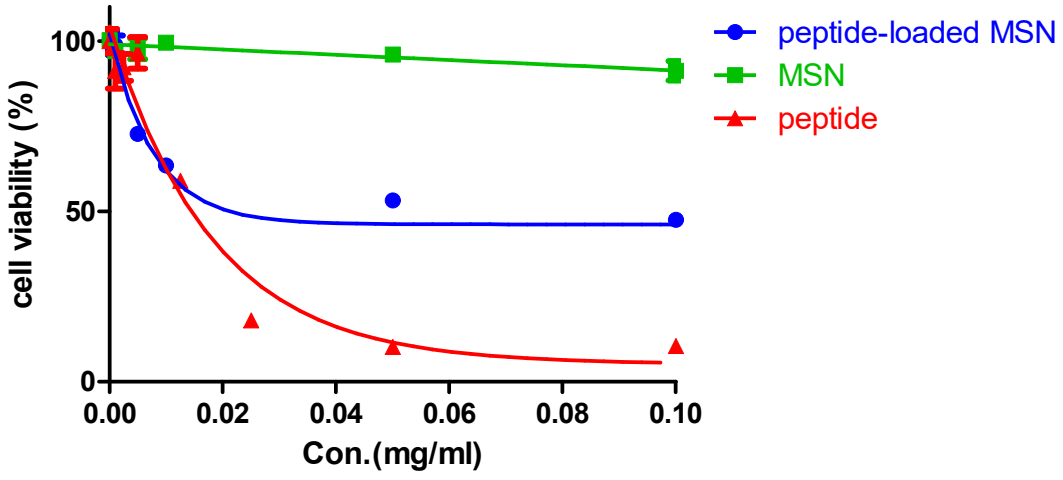

Figure 3.15, Cell viabilities of murine GL26 cells that were incubated for 3 h with unloaded MSNs (green), SA-K_6L_9-AS loaded MSNs (blue), and free SA-K_6L_9-AS (red) MSN, as determined by means of the MTT assay.

Interestingly, after 24 h of incubation, the cytotoxicity of SA-K_6L_9-AS loaded MSNs towards GL26 cells did increase slightly, indicating enhanced release of SA-K_6L_9-AS. This could have been caused by the increased intracellular pH (pH_i) in malignant glioma cells as a result of increased activities of the type I sodium/hydrogen exchanger (NHE1).[93] Increased intracellular pH leads to faster dissolution of the MSNs, thus releasing more SA-K_6L_9-AS per unit of time.[82]

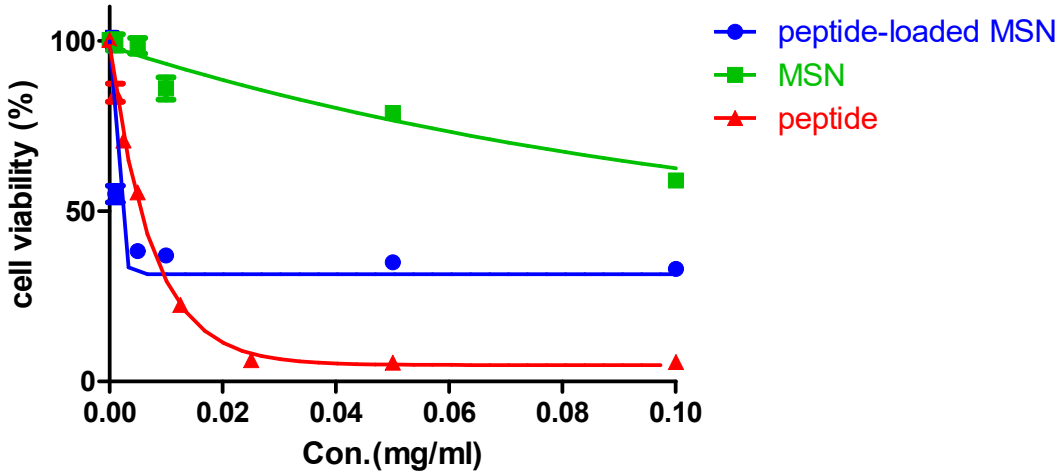

Figure 3.16, Cell viabilities of murine GL26 cells that were incubated for 24 h with unloaded MSNs (green), SA-K_6L_9-AS loaded MSNs (blue), and free SA-K_6L_9-AS (red) MSN, as determined by means of the MTT assay.

3.3.3.2.3 Incubation of Murine Breast Cancer Cells with SA-K_6L_9-AS-loaded MSNs and Controls

Apparently, incubation of 4T1 cells with SA-K_6L_9-AS loaded MSNs for 3h was insufficient to release significant amounts of SA-K_6L_9-AS. Therefore, as shown in Figure 3.17, the observed cytotoxicity for free MSN and SA-K_6L_9-AS loaded MSNs was virtually the same. However, free SA-K_6L_9-AS displayed a similar cytotoxicity towards 4T1 cells than towards GL26 cells or NSC. This result was somewhat unexpected. It may be an indication of different metabolisms in 4T1 cells (murine breast cancer) and GL26 cells (murine glioma). However, after

24 h of incubation, sufficient amounts of SA-K_6L_9-AS were released from the MSNs to display cytotoxicity. Interestingly, the toxicity of free MSNs against both cancer cell lines is somewhat lower than against NSC. The corresponding median lethal doses (LC_{50} values)[94] for all cell viability assays described here are summarized in Table 3.1.

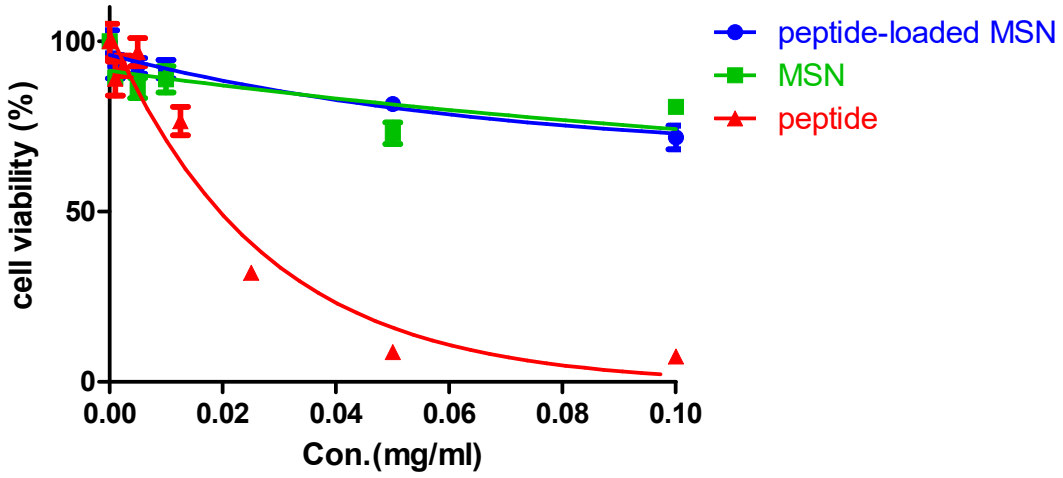

Figure 3.17, Cell viabilities of murine 4T1 cells that were incubated for 3 h with unloaded MSNs (green), SA-K_6L_9-AS loaded MSNs (blue), and free SA-K_6L_9-AS (red) MSN, as determined by means of the MTT assay.

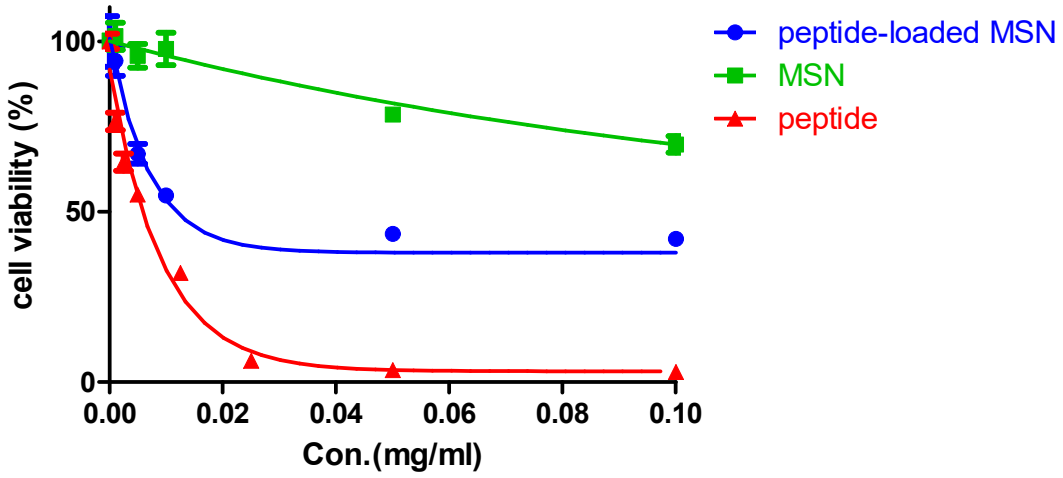

Figure 3.18, Cell viabilities of murine GL26 cells that were incubated for 24 h with unloaded MSNs (green), SA-K_6L_9-AS loaded MSNs (blue), and free SA-K_6L_9-AS (red) MSN, as determined by means of the MTT assay.

	LC_{50} values (mg/ml)		
	MSNs	peptide	Peptide-loaded MSN
NSC 3h	0.1023 (R^2 = 0.9242)	0.01494 (R^2 = 0.7900)	0.009787 (R^2 = 0.7659)
NSC 24h	0.03495 (R^2 = 0.9145)	0.001637 (R^2 = 0.8336)	0.002815 (R^2 = 0.7672)
GL26 3h	1.389 (R^2 = 0.8448)	0.01262 (R^2 = 0.9348)	0.005461 (R^2 = 0.9554)
GL24 24h	0.07924 (R^2 = 0.9539)	0.005213 (R^2 = 0.9937)	0.0006627 (R^2 = 0.9401)
4T1 3h	0.1138 (R^2 = 0.7946)	0.01897 (R^2 = 0.9285)	0.04869 (R^2 = 0.8648)
4T1 24h	0.08531 (R^2 = 0.9316)	0.006349 (R^2 = 0.9734)	0.004927 (R^2 = 0.9284)

Table 3.1, LC_{50} values (mg/ml) for free MSNs, SA-K_6L_9-AS, and SA-K_6L_9-AS loaded MSNs after 3 h and 24 h of incubation against neural stem cells (NSC), murine glioma (GL26) and murine breast cancer (4T1) cell lines. LC_{50} values were determined by means of fitting with Graphpad prism 5.0[80], non-linear fits (one phase decays) were applied.

3.3.3.2.4 Summary of the *In-Vitro* Evaluation of SA-K_6L_9-AS loaded MSNs vs. Controls

All experiments reported here have indicated that a slow release of SA-K_6L_9-AS from MSNs is possible, which occurs either during endocytosis or after the SA-K_6L_9-AS loaded MSNs have been released into the cytoplasm by means of endosomal escape.[92] From the vantage point of looking for a suitable material for neural stem cell-mediated drug transport to tumors and metastases, the rate of SA-K_6L_9-AS from the MSNs is too high to permit their safe transport without killing the transport cell before reaching the target. In mice, this process takes up to three days.[8] Therefore, a gatekeeper is mandatory to delay the release of SA-K_6L_9-AS from the MSNs. For this purpose, the use of *polysilazane-coated SA-K_6L_9-AS-loaded MSNs* was explored in the cell experiments described below.

3.3.3.3 The Use of Polysilazane Designer Copolymers as Gatekeepers

Our hypothesis is that the polysilazane copolymer $[SiH_2NH]_5[SiHCH_3NH]_4[SiHC_2H_3NH]$ slowly dissolves upon contact with aqueous medium, thus releasing soluble $Si(OH)_4$, ammonia, molecular hydrogen, methanol and acetaldehyde. The soluble silica is readily absorbed by the cells[82], all other reaction products are discharged. This slow release reaction will facilitate the protection from SA-K_6L_9-AS release from the MSNs while the gatekeeper layer is still intact. Upon resolution of this layer, the release of SA-K_6L_9-AS from the MSNs is observed.

3.3.3.3.1 Incubation of Neural Stem Cells with Polysilazane-Coated SA-K_6L_9-AS-loaded MSNs and Controls

In analogy to the set of experiments reported above, the first set of experiments was concerned with the cytotoxicity of polysilazane-coated SA-K_6L_9-AS loaded MSNs to neural stem cells. NSC were incubated with various concentrations of SA-K_6L_9-AS loaded MSNs. This was followed by measuring cell viabilities vs. a group of NSC that were not exposed to SA-K_6L_9-AS loaded MSNs. The results were, again, compared to the cell viabilities that were observed after incubation with approx. the same concentration of SA-K_6L_9-AS. After 24 h of incubation, free MSN and free peptide displayed the anticipated cytotoxity. The presence of the gatekeeper polysilazane layer decreased the cytotoxicity of polysilazane-coated SA-K_6L_9-AS loaded MSNs to neural stem cells slightly. Although this result is not optimal with respect to developing a cell-mediated approach to treating solid tumors, it nevertheless shows proof-of-principle.

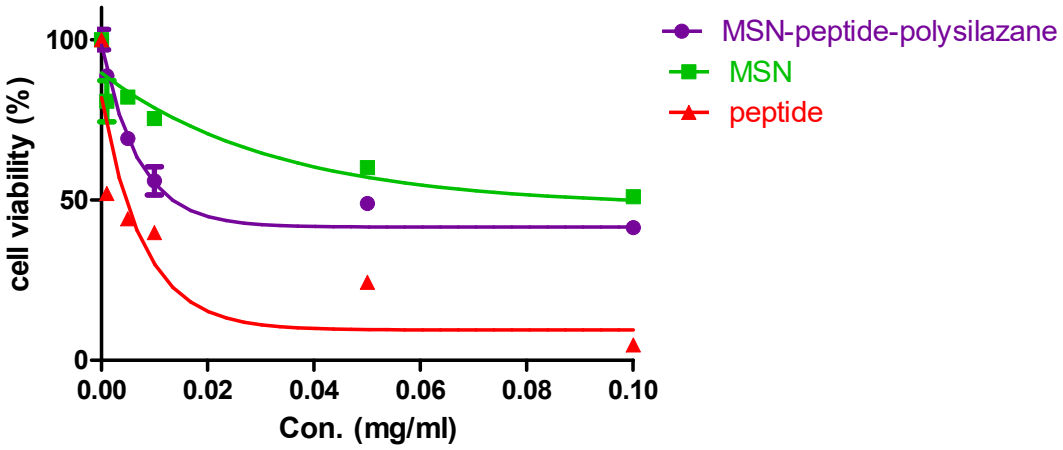

Figure 3.19, Cell viabilities of murine neural stem cells that were incubated for 24 h with unloaded MSNs (green), polysilazane-coated SA-K_6L_9-AS loaded MSNs (purple), and free SA-K_6L_9-AS (red) MSN, as determined by means of the MTT assay.

It is noteworthy that after 72h of incubation, polysilazane-coated SA-K_6L_9-AS loaded MSNs were more cytotoxic to murine neural stem cells that the free peptide, especially in the lower concentration range. This may have been caused by enhanced uptake of the polysilazane-coated SA-K_6L_9-AS loaded MSNs into the MSNs, followed by biocorrosion of the gatekeeper layer and, potentially, parts of the MSNs. This experiment clearly proved that a timed release of SA-K_6L_9-AS from polysilazane-coated SA-K_6L_9-AS loaded MSNs is principally possible. We regard this result as proof-of-concept that polysilazane coating of MSNs is a viable strategy for delayed drug delivery.

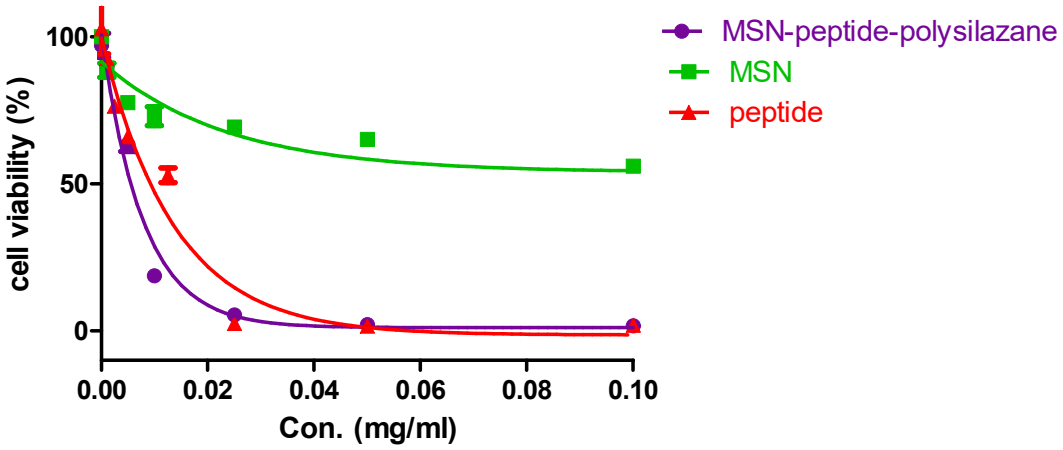

Figure 3.20, Cell viabilities of murine neural stem cells that were incubated for 24 h with unloaded MSNs (green), polysilazane-coated SA-K_6L_9-AS loaded MSNs (purple), and free SA-K_6L_9-AS (red) MSN, as determined by means of the MTT assay.

3.3.3.3.2 Incubation of GL26 Cells with Polysilazane-Coated SA-K_6L_9-AS-loaded MSNs and Controls

The same trend is discernible against GL26 cells, although both, free MSNs and polysilazane-coated SA-K_6L_9-AS loaded MSNs were less cytotoxic against murine glioma cells, compared to murine neural stem cells (Figure 3.21 and 3.22). However, also in this set of experiments, the concept of timed release using a polysilazane gatekeeper layer was clearly demonstrated, as the comparison of cell viabilities after 24 h and 72 h of incubation with polysilazane-coated SA-K_6L_9-AS loaded MSNs demonstrated. In that case, SA-K_6L_9-AS release from MSNs was virtually not complete after 72 h. However, significant amounts of therapeutic peptide were delivered utilizing polysilazane-coated SA-K_6L_9-AS loaded MSNs.

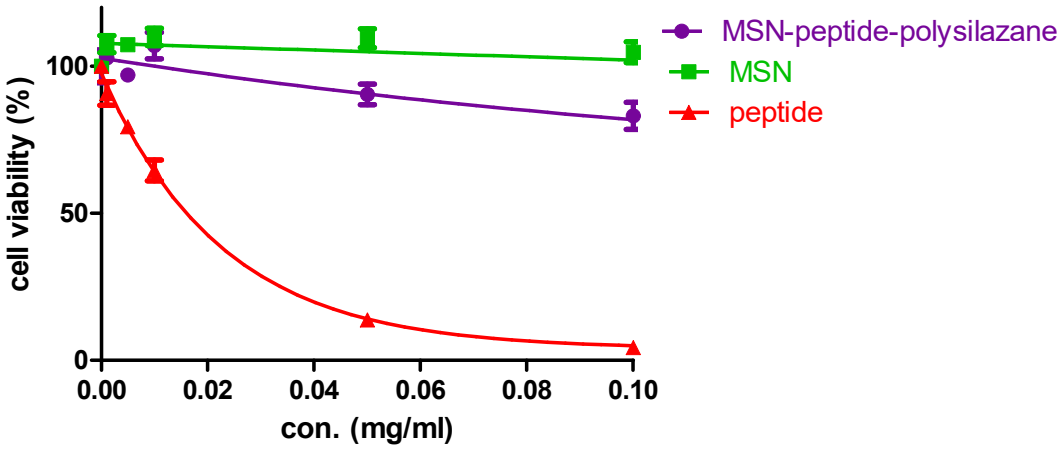

Figure 3.21, Cell viabilities of murine GL26 cells that were incubated for 24 h with unloaded MSNs (green), polysilazane-coated SA-K_6L_9-AS loaded MSNs (purple), and free SA-K_6L_9-AS (red) MSN, as determined by means of the MTT assay.

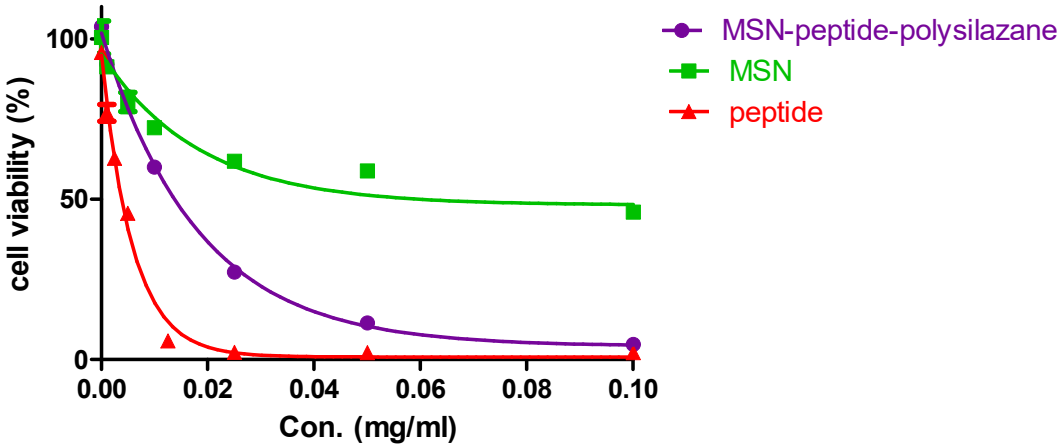

Figure 3.22, Cell viabilities of murine GL 26 cells that were incubated for 72 h with unloaded MSNs (green), polysilazane-coated SA-K_6L_9-AS loaded MSNs (purple), and free SA-K_6L_9-AS (red) MSN, as determined by means of the MTT assay.

3.3.3.3.3 Incubation of 4T1 Cells with Polysilazane-Coated SA-K_6L_9-AS-loaded MSNs and Controls

As this has been already observed when studying the behavior of SA-K_6L_9-AS loaded MSNs, SA-K_6L_9-AS release from polysilazane-coated SA-K_6L_9-AS-loaded MSNs in murine 4T1 proceeded very similar to murine GL26 cells. Although only a minor fraction of SA-K_6L_9-AS was released after 24 h from coated MSNs, virtually complete release of SA-K_6L_9-AS was observed after 72 h of incubation. In that case, the efficacy of free SA-K_6L_9-AS and polysilazane-coated SA-K_6L_9-AS-loaded MSNs was essentially the same. This finding can be regarded as another proof-of-concept that polysilazane gatekeeper layers around MSNs can work reliably under physiological conditions. The corresponding median lethal doses (LC_{50} values)[94] for all cell viability assays described here are summarized in Table 3.2.

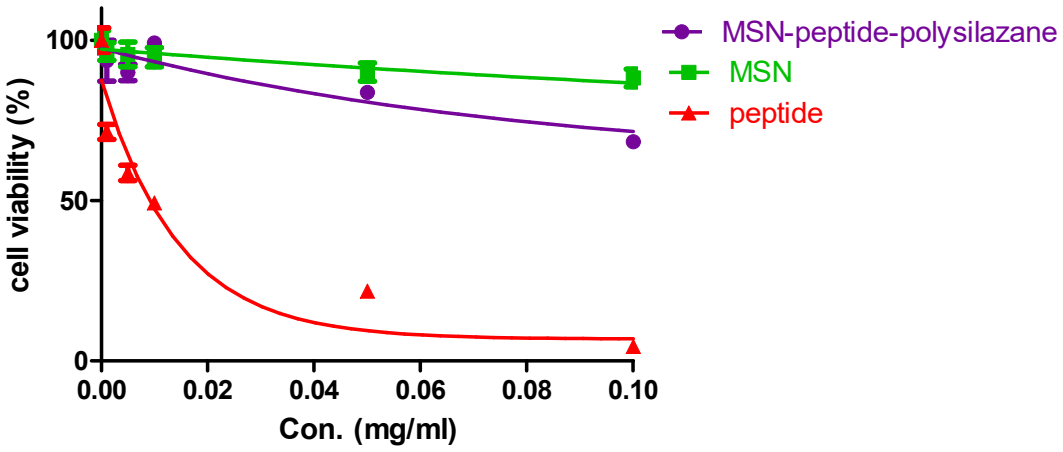

Figure 3.23, Cell viabilities of murine 4T1 cells that were incubated for 24 h with unloaded MSNs (green), polysilazane-coated SA-K_6L_9-AS loaded MSNs (purple), and free SA-K_6L_9-AS (red) MSN, as determined by means of the MTT assay.

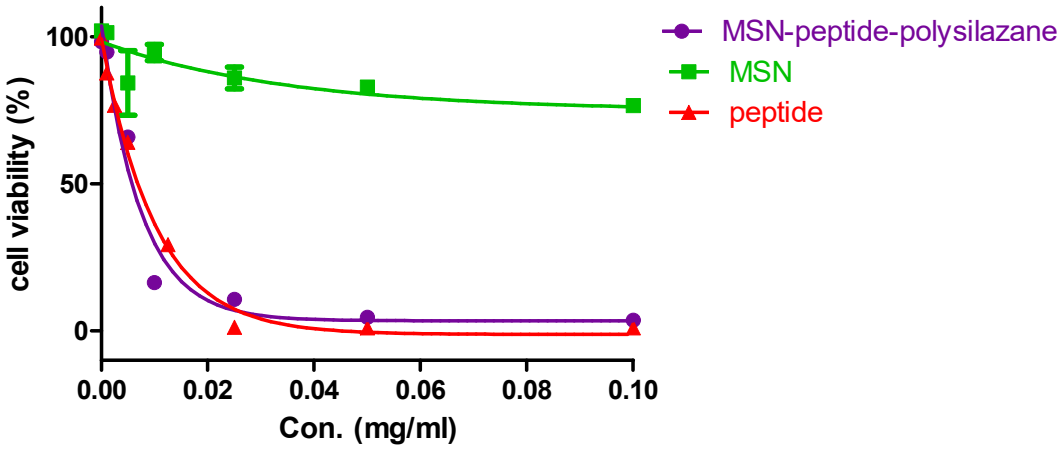

Figure 3.24, Cell viabilities of murine 4T1 cells that were incubated for 72 h with unloaded MSNs (green), polysilazane-coated SA-K_6L_9-AS loaded MSNs (purple), and free SA-K_6L_9-AS (red) MSN, as determined by means of the MTT assay.

	LC_{50} values (mg/ml)		
	MSN	peptide	MSN-peptide-polysilazane
NSC 24h	0.02285 (R^2 = 0.8790)	0.005493 (R^2 = 0.8400)	0.004855 (R^2 = 0.9474)
NSC 72h	0.03495 (R^2 = 0.9145)	0.001637 (R^2 = 0.8336)	0.002815 (R^2 = 0.7672)
GL26 24h	~159.8	0.01569 (R^2 = 0.9904)	0.1063 (R^2 = 0.8309)
GL24 72h	0.01274 (R^2 = 0.9085)	0.004043 (R^2 = 0.9896)	0.01262 (R^2 = 0.9931)
4T1 24h	0.1498 (R^2 = 0.7749)	0.01008 (R^2 = 0.9386)	0.05766 (R^2 = 0.8331)
4T1 72h	0.02439 (R^2 = 0.5096)	0.007050 (R^2 = 0.9923)	0.005181 (R^2 = 0.9699)

Table 3.2, LC_{50} values (mg/ml) for free MSNs, SA-K_6L_9-AS, and polysilazane-coated SA-K_6L_9-AS loaded MSNs after 24 h and 72h of incubation against neural stem cells (NSC), murine glioma (GL26) and murine breast cancer (4T1) cell lines. LC_{50} values were determined by means of fitting with Graphpad prism 5.0[80], non-linear fits (one phase decays) were applied.

3.4 Conclusions and Outlook

This research reported here has demonstrated the feasibility of using polysilazane designer copolymers are gate-keepers of mesoporous silica (nan)particles that were designed for the purpose of drug delivery. Contrary to conventional gatekeepers[82], which can be pH-sensitive, redox-sensitive, or in response to external stimuli (e.g. light or magnetic fields)[82], we are taking advantage of the slow biocorrosion of a biocompatible inorganic polymer. Polysilazane designer copolymers are able to facilitate sufficiently fast uptake, as indicated by the *in-vitro* experiments discussed here. After endocytosis, the therapeutic peptide SA-K_6L_9-AS is slowly released from the polysilazane-coated SA-K_6L_9-AS loaded MSNs. Since this peptide is targeting mammalian cell membranes, which it destabilizes and then partially dissolves according to the carpet mechanism[95], its slow release will enhance the rate of endosomal escape.[92] Once SA-K_6L_9-AS reaches the cytoplasm, it is able to target the mitochondria, as demonstrated by means of confocal laser microscopy in chapter 1 of this thesis. Targeting the mitochondria activates various pathways of programmed cell death (apoptosis).[84]

The hallmark of apoptotic cell death is a caspase storm, which dissects the mammalian cell into apoptotic bodies, which are then taken up by neighboring cells.[85] The biochemical mechanism of apoptosis offers the advantage of delivering the whole cargo comprised of SA-K_6L_9-AS and MSN-bound SA-K_6L_9-AS to the bystander cells. If this process is correctly timed to take place after the transport cell has reached the targeted tumor tissue, sufficient amounts of SA-K_6L_9-AS could be delivered during apoptosis of the delivery cell to cause necrosis of tumor and stroma cells, which will result in the release of neoantigens.[96] However, either the thickness and/or chemical composition of the gatekeeper polysilazane layer or the choice of transport cell (e.g. a defensive cell) will have to be optimized to make this process more efficient. Currently,

the toxicity of MSNs towards murine neural stem cells is somewhat too high to facilitate efficient cell transport to tumors and metastases after administering the transport cells to the blood stream. Nevertheless, the *in-vitro* experiments performed here have clearly indicated the potential of using mesoporous silica (nano)particles with polysilazane copolymers as gatekeepers for cell-based drug delivery and timed release.

3.5 References

1. Pasqua, L.; Leggio, A.; Sisci, D.; Ando, S.; Morelli, C., Mesoporous Silica Nanoparticles in Cancer Therapy: Relevance of the Targeting Function. *Mini Rev Med Chem* **2016,** *16* (9), 743-53.
2. Yamamoto, E.; Kuroda, K., Colloidal mesoporous silica nanoparticles. *Bull. Chem. Soc. Jpn.* **2016,** *89* (5), 501-539.
3. Roggers, R.; Kanvinde, S.; Boonsith, S.; Oupicky, D., The Practicality of Mesoporous Silica Nanoparticles as Drug Delivery Devices and Progress Toward This Goal. *AAPS PharmSciTech* **2014,** *15* (5), 1163-1171.
4. Tao, Z., Mesoporous silica-based nanodevices for biological applications. *RSC Adv.* **2014,** *4* (36), 18961-18980.
5. Colilla, M.; Vallet-Regi, M., Smart drug delivery from silica nanoparticles. *RSC Smart Mater.* **2013,** *3* (Smart Materials for Drug Delivery, Volume 2), 63-89.
6. Rosenholm, J. M.; Mamaeva, V.; Sahlgren, C.; Linden, M., Nanoparticles in targeted cancer therapy: mesoporous silica nanoparticles entering preclinical development stage. *Nanomedicine (London, U. K.)* **2012,** *7* (1), 111-120.
7. Argyo, C.; Weiss, V.; Braeuchle, C.; Bein, T., Multifunctional Mesoporous Silica Nanoparticles as a Universal Platform for Drug Delivery. *Chem. Mater.* **2014,** *26* (1), 435-451.
8. Rachakatla, R. S.; Balivada, S.; Seo, G.-M.; Myers, C. B.; Wang, H.; Samarakoon, T. N.; Dani, R.; Pyle, M.; Kroh, F. O.; Walker, B.; Leaym, X.; Koper, O. B.; Chikan, V.; Bossmann, S. H.; Tamura, M.; Troyer, D. L., Attenuation of Mouse Melanoma by A/C Magnetic Field after Delivery of Bi-Magnetic Nanoparticles by Neural Progenitor Cells. *ACS Nano* **2010,** *4* (12), 7093-7104.
9. Jain, R. K.; Stylianopoulos, T., Delivering nanomedicine to solid tumors. *Nat Rev Clin Oncol* **2010,** *7* (11), 653-64.
10. Thomsen, S.; Pearce, J. A.; Giustini, A.; Hoopes, P. J., Nanoparticles in Medicine: Selected Observations and Experimental Caveats. *Proc SPIE Int Soc Opt Eng* **2013,** *8584*, 858402.

11. He, Q.; Zhang, Z.; Gao, F.; Li, Y.; Shi, J., In vivo Biodistribution and Urinary Excretion of Mesoporous Silica Nanoparticles: Effects of Particle Size and PEGylation. *Small* **2011,** *7* (2), 271-280.
12. Huang, X.; Li, L.; Liu, T.; Hao, N.; Liu, H.; Chen, D.; Tang, F., The Shape Effect of Mesoporous Silica Nanoparticles on Biodistribution, Clearance, and Biocompatibility in Vivo. *ACS Nano* **2011,** *5* (7), 5390-5399.
13. Stirland, D. L.; Matsumoto, Y.; Toh, K.; Kataoka, K.; Bae, Y. H., Analyzing spatiotemporal distribution of uniquely fluorescent nanoparticles in xenograft tumors. *J Control Release* **2016,** *227*, 38-44.
14. Basel, M. T.; Balivada, S.; Wang, H.; Shrestha, T. B.; Seo, G. M.; Pyle, M.; Abayaweera, G.; Dani, R.; Koper, O. B.; Tamura, M.; Chikan, V.; Bossmann, S. H.; Troyer, D. L., Cell-delivered magnetic nanoparticles caused hyperthermia-mediated increased survival in a murine pancreatic cancer model. *Int. J. Nanomed.* **2012,** *7*, 297-306.
15. Seo, G. M.; Rachakatla, R. S.; Balivada, S.; Pyle, M.; Shrestha, T. B.; Basel, M. T.; Myers, C.; Wang, H.; Tamura, M.; Bossmann, S. H.; Troyer, D. L., A self-contained enzyme activating prodrug cytotherapy for preclinical melanoma. *Mol Biol Rep* **2012,** *39* (1), 157-65.
16. Basel, M. T.; Balivada, S.; Shrestha, T. B.; Seo, G. M.; Pyle, M. M.; Tamura, M.; Bossmann, S. H.; Troyer, D. L., A cell-delivered and cell-activated SN38-dextran prodrug increases survival in a murine disseminated pancreatic cancer model. *Small* **2012,** *8* (6), 913-20.
17. Wendel, S. O.; Menon, S.; Alshetaiwi, H.; Shrestha, T. B.; Chlebanowski, L.; Hsu, W.-W.; Bossmann, S. H.; Narayanan, S.; Troyer, D. L., Cell Based Drug Delivery: *Micrococcus luteus* Loaded Neutrophils as Chlorhexidine Delivery Vehicles in a Mouse Model of Liver Abscesses in Cattle. *PLoS ONE* **2015,** *10* (5), e0128144.
18. Huang, D.-M.; Hung, Y.; Ko, B.-S.; Hsu, S.-C.; Chen, W.-H.; Chien, C.-L.; Tsai, C.-P.; Kuo, C.-T.; Kang, J.-C.; Yang, C.-S.; Mou, C.-Y.; Chen, Y.-C., Highly efficient cellular labeling of mesoporous nanoparticles in human mesenchymal stem cells: implication for stem cell tracking. *FASEB J.* **2005,** *19* (14), 2014-2016.

19. Liu, H.-M.; Wu, S.-H.; Lu, C.-W.; Yao, M.; Hsiao, J.-K.; Hung, Y.; Lin, Y.-S.; Mou, C.-Y.; Yang, C.-S.; Huang, D.-M.; Chen, Y.-C., Mesoporous silica nanoparticles improve magnetic labeling efficiency in human stem cells. *Small* **2008,** *4* (5), 619-626.
20. Hsiao, J.-K.; Tsai, C.-P.; Chung, T.-H.; Hung, Y.; Yao, M.; Liu, H.-M.; Mou, C.-Y.; Yang, C.-S.; Chen, Y.-C.; Huang, D.-M., Mesoporous silica nanoparticles as a delivery system of gadolinium for effective human stem cell tracking. *Small* **2008,** *4* (9), 1445-1452.
21. Huang, X.; Zhang, F.; Wang, H.; Niu, G.; Choi, K. Y.; Swierczewska, M.; Zhang, G.; Gao, H.; Wang, Z.; Zhu, L.; Choi, H. S.; Lee, S.; Chen, X., Mesenchymal stem cell-based cell engineering with multifunctional mesoporous silica nanoparticles for tumor delivery. *Biomaterials* **2013,** *34* (7), 1772-1780.
22. Zhang, L.; Wang, Y.; Tang, Y.; Jiao, Z.; Xie, C.; Zhang, H.; Gu, P.; Wei, X.; Yang, G.-Y.; Gu, H.; Zhang, C., High MRI performance fluorescent mesoporous silica-coated magnetic nanoparticles for tracking neural progenitor cells in an ischemic mouse model. *Nanoscale* **2013,** *5* (10), 4506-4516.
23. Cheng, Y.; Morshed, R.; Cheng, S.-H.; Tobias, A.; Auffinger, B.; Wainwright, D. A.; Zhang, L.; Yunis, C.; Han, Y.; Chen, C.-T.; Lo, L.-W.; Aboody, K. S.; Ahmed, A. U.; Lesniak, M. S., Nanoparticle-Programmed Self-Destructive Neural Stem Cells for Glioblastoma Targeting and Therapy. *Small* **2013,** *9* (24), 4123-4129.
24. He, D.; He, X.; Wang, K.; Cao, J.; Zhao, Y., A light-responsive reversible molecule-gated system using thymine-modified mesoporous silica nanoparticles. *Langmuir* **2012,** *28* (8), 4003-4008.
25. Ferris, D. P.; Zhao, Y.-L.; Khashab, N. M.; Khatib, H. A.; Stoddart, J. F.; Zink, J. I., Light-operated mechanized nanoparticles. *J. Am. Chem. Soc.* **2009,** *131* (5), 1686-1688.
26. Croissant, J.; Zink, J. I., Nanovalve-Controlled Cargo Release Activated by Plasmonic Heating. *J. Am. Chem. Soc.* **2012,** *134* (18), 7628-7631.
27. Knezevic, N. Z.; Trewyn, B. G.; Lin, V. S. Y., Light- and pH-Responsive Release of Doxorubicin from a Mesoporous Silica-Based Nanocarrier. *Chem. - Eur. J.* **2011,** *17* (12), 3338-3342, S3338/1-S3338/6.
28. Liu, R.; Zhang, Y.; Feng, P., Multiresponsive Supramolecular Nanogated Ensembles. *J. Am. Chem. Soc.* **2009,** *131* (42), 15128-15129.

29. Dobay, M. P.; Schmidt, A.; Mendoza, E.; Bein, T.; Raedler, J. O., Cell Type Determines the Light-Induced Endosomal Escape Kinetics of Multifunctional Mesoporous Silica Nanoparticles. *Nano Lett.* **2013,** *13* (3), 1047-1052.
30. Vahrmeijer, A. L.; Hutteman, M.; van der Vorst, J. R.; van de Velde, C. J. H.; Frangioni, J. V., Image-guided cancer surgery using near-infrared fluorescence. *Nat. Rev. Clin. Oncol.* **2013,** *10* (9), 507-518.
31. Yang, X.; Liu, X.; Liu, Z.; Pu, F.; Ren, J.; Qu, X., Near-Infrared Light-Triggered, Targeted Drug Delivery to Cancer Cells by Aptamer Gated Nanovehicles. *Adv. Mater. (Weinheim, Ger.)* **2012,** *24* (21), 2890-2895.
32. Giri, S.; Trewyn, B. G.; Stellmaker, M. P.; Lin, V. S. Y., Stimuli-responsive controlled-release delivery system based on mesoporous silica nanorods capped with magnetic nanoparticles. *Angew. Chem., Int. Ed.* **2005,** *44* (32), 5038-5044.
33. Aznar, E.; Marcos, M. D.; Martinez-Manez, R.; Sancenon, F.; Soto, J.; Amoros, P.; Guillem, C., pH- and Photo-Switched Release of Guest Molecules from Mesoporous Silica Supports. *J. Am. Chem. Soc.* **2009,** *131* (19), 6833-6843.
34. Ruiz-Hernandez, E.; Baeza, A.; Vallet-Regi, M., Smart Drug Delivery through DNA/Magnetic Nanoparticle Gates. *ACS Nano* **2011,** *5* (2), 1259-1266.
35. Baeza, A.; Guisasola, E.; Ruiz-Hernandez, E.; Vallet-Regi, M., Magnetically Triggered Multidrug Release by Hybrid Mesoporous Silica Nanoparticles. *Chem. Mater.* **2012,** *24* (3), 517-524.
36. Basel, M. T.; Shrestha, T. B.; Bossmann, S. H.; Troyer, D. L., Cells as delivery vehicles for cancer therapeutics. *Ther. Delivery* **2014,** *5* (5), 555-567.
37. Liu, R.; Zhang, Y.; Zhao, X.; Agarwal, A.; Mueller, L. J.; Feng, P., pH-Responsive Nanogated Ensemble Based on Gold-Capped Mesoporous Silica through an Acid-Labile Acetal Linker. *J. Am. Chem. Soc.* **2010,** *132* (5), 1500-1501.
38. Cheng, S.-H.; Liao, W.-N.; Chen, L.-M.; Lee, C.-H., pH-controllable release using f unctionalized mesoporous silica nanoparticles as an oral drug delivery system. *J. Mater. Chem.* **2011,** *21* (20), 7130-7137.
39. Ambrogio, M. W.; Thomas, C. R.; Zhao, Y.-L.; Zink, J. I.; Stoddart, J. F., Mechanized Silica Nanoparticles: A New Frontier in Theranostic Nanomedicine. *Acc. Chem. Res.* **2011,** *44* (10), 903-913.

40. Xing, L.; Zheng, H.; Cao, Y.; Che, S., Coordination Polymer Coated Mesoporous Silica Nanoparticles for pH-Responsive Drug Release. *Adv. Mater. (Weinheim, Ger.)* **2012,** *24* (48), 6433-6437.
41. Kato, Y.; Ozawa, S.; Miyamoto, C.; Maehata, Y.; Suzuki, A.; Maeda, T.; Baba, Y., Acidic extracellular microenvironment and cancer. *Cancer Cell Int* **2013,** *13* (1), 89.
42. Giret, S.; Man, M. W. C.; Carcel, C., Mesoporous-Silica-Functionalized Nanoparticles f or Drug Delivery. *Chem. - Eur. J.* **2015,** *21* (40), 13850-13865.
43. Ma, X.; Nguyen, K. T.; Borah, P.; Ang, C. Y.; Zhao, Y., Functional Silica Nanoparticles for Redox-Triggered Drug/ssDNA Co-delivery. *Adv. Healthcare Mater.* **2012,** *1* (6), 690-697.
44. Kim, H.; Kim, S.; Park, C.; Lee, H.; Park, H. J.; Kim, C., Glutathione-induced intracellular release of guests from mesoporous silica nanocontainers with cyclodextrin gatekeepers. *Adv Mater* **2010,** *22* (38), 4280-3.
45. Cui, Y.; Dong, H.; Cai, X.; Wang, D.; Li, Y., Mesoporous silica nanoparticles capped with disulfide-linked PEG gatekeepers for glutathione-mediated controlled release. *ACS Appl Mater Interfaces* **2012,** *4* (6), 3177-83.
46. Mas, N.; Agostini, A.; Mondragon, L.; Bernardos, A.; Sancenon, F.; Marcos, M. D.; Martinez-Manez, R.; Costero, A. M.; Gil, S.; Merino-Sanjuan, M.; Amoros, P.; Orzaez, M.; Perez-Paya, E., Enzyme-Responsive Silica Mesoporous Supports Capped with Azopyridinium Salts for Controlled Delivery Applications. *Chem. - Eur. J.* **2013,** *19* (4), 1346-1356.
47. Liu, J.; Du, X.; Zhang, X., Enzyme-Inspired Controlled Release of Cucurbit[7]uril Nanovalves by Using Magnetic Mesoporous Silica. *Chem. - Eur. J.* **2011,** *17* (3), 810-815, S810/1-S810/16.
48. Patel, K.; Angelos, S.; Dichtel, W. R.; Coskun, A.; Yang, Y.-W.; Zink, J. I.; Stoddart, J. F., Enzyme-Responsive Snap-Top Covered Silica Nanocontainers. *J. Am. Chem. Soc.* **2008,** *130* (8), 2382-2383.
49. Slowing, I.; Trewyn, B. G.; Lin, V. S. Y., Effect of Surface Functionalization of MCM-41-Type Mesoporous Silica Nanoparticles on the Endocytosis by Human Cancer Cells. *J. Am. Chem. Soc.* **2006,** *128* (46), 14792-14793.

50. Agostini, A.; Mondragon, L.; Pascual, L.; Aznar, E.; Coll, C.; Martinez-Manez, R.; Sancenon, F.; Soto, J.; Marcos, M. D.; Amoros, P.; Costero, A. M.; Parra, M.; Gil, S., Design of Enzyme-Mediated Controlled Release Systems Based on Silica Mesoporous Supports Capped with Ester-Glycol Groups. *Langmuir* **2012,** *28* (41), 14766-14776.

51. Bernardos, A.; Mondragon, L.; Aznar, E.; Marcos, M. D.; Martinez-Manez, R.; Sancenon, F.; Soto, J.; Barat, J. M.; Perez-Paya, E.; Guillem, C.; Amoros, P., Enzyme-Responsive Intracellular Controlled Release Using Nanometric Silica Mesoporous Supports Capped with "Saccharides". *ACS Nano* **2010,** *4* (11), 6353-6368.

52. Bernardos, A.; Aznar, E.; Marcos, M. D.; Martinez-Manez, R.; Sancenon, F.; Soto, J.; Barat, J. M.; Amoros, P., Enzyme-Responsive Controlled Release Using Mesoporous Silica Supports Capped with Lactose. *Angew. Chem., Int. Ed.* **2009,** *48* (32), 5884-5887, S5884/1-S5884/7.

53. Coll, C.; Mondragon, L.; Martinez-Manez, R.; Sancenon, F.; Marcos, M. D.; Soto, J.; Amoros, P.; Perez-Paya, E., Enzyme-Mediated Controlled Release Systems by Anchoring Peptide Sequences on Mesoporous Silica Supports. *Angew. Chem., Int. Ed.* **2011,** *50* (9), 2138-2140, S2138/1-S2138/7.

54. de la Torre, C.; Mondragon, L.; Coll, C.; Sancenon, F.; Marcos, M. D.; Martinez-Manez, R.; Amoros, P.; Perez-Paya, E.; Orzaez, M., Cathepsin-B induced controlled release from peptide-capped mesoporous silica nanoparticles. *Chem. - Eur. J.* **2014,** *20* (47), 15309-15314.

55. Wang, H.; Udukala, D. N.; Samarakoon, T. N.; Basel, M. T.; Kalita, M.; Abayaweera, G.; Manawadu, H.; Malalasekera, A.; Robinson, C.; Villanueva, D.; Maynez, P.; Bossmann, L.; Riedy, E.; Barriga, J.; Wang, N.; Li, P.; Higgins, D. A.; Zhu, G.; Troyer, D. L.; Bossmann, S. H., Nanoplatforms for highly sensitive fluorescence detection of cancer-related proteases. *Photochem. Photobiol. Sci.* **2014,** *13* (2), 231-240.

56. Udukala, D. N.; Wang, H.; Wendel, S. O.; Malalasekera, A. P.; Samarakoon, T. N.; Yapa, A. S.; Abayaweera, G.; Basel, M. T.; Maynez, P.; Ortega, R.; Toledo, Y.; Bossmann, L.; Robinson, C.; Janik, K. E.; Koper, O. B.; Li, P.; Motamedi, M.; Higgins, D. A.; Gadbury, G.; Zhu, G.; Troyer, D. L.; Bossmann, S. H., Early breast cancer screening using iron/iron oxide-based nanoplatforms with sub-femtomolar limits of detection. *Beilstein J. Nanotechnol.* **2016,** *7*, 364-373.

57. Piktel, E.; Niemirowicz, K.; Wątek, M.; Wollny, T.; Deptuła, P.; Bucki, R., Recent insights in nanotechnology-based drugs and formulations designed for effective anti-cancer therapy. *Journal of nanobiotechnology* **2016,** *14* (1), 39.

58. Yang, Y.; Yu, C., Advances in silica based nanoparticles for targeted cancer therapy. *Nanomedicine: Nanotechnology, Biology and Medicine* **2016,** *12* (2), 317-332.

59. Ma, B.; He, L.; You, Y.; Mo, J.; Chen, T., Controlled synthesis and size effects of multifunctional mesoporous silica nanosystem for precise cancer therapy. *Drug delivery* **2018,** *25* (1), 293-306.

60. Papo, N.; Braunstein, A.; Eshhar, Z.; Shai, Y., Suppression of Human Prostate Tumor Growth in Mice by a Cytolytic D-, L-Amino Acid Peptide: Membrane Lysis, Increased Necrosis, and Inhibition of Prostate-Specific Antigen Secretion. *Cancer Res.* **2004,** *64* (16), 5779-5786.

61. Soengas, M. S.; Lowe, S. W., Apoptosis and melanoma chemoresistance. *Oncogene* **2003,** *22* (20), 3138-3151.

62. Bracci, L.; Schiavoni, G.; Sistigu, A.; Belardelli, F., Immune-based mechanisms of cytotoxic chemotherapy: implications for the design of novel and rationale-based combined treatments against cancer. *Cell Death Differ.* **2014,** *21* (1), 15-25.

63. Sauter, B.; Albert, M. L.; Francisco, L.; Larsson, M.; Somersan, S.; Bhardwaj, N., Consequences of cell death: exposure to necrotic tumor cells, but not primary tissue cells or apoptotic cells, induces the maturation of immunostimulatory dendritic cells. *J. Exp. Med.* **2000,** *191* (3), 423-433.

64. Papo, N.; Braunstein, A.; Eshhar, Z.; Shai, Y., Suppression of human prostate tumor growth in mice by a cytolytic d-, l-amino acid peptide: membrane lysis, increased necrosis, and inhibition of prostate-specific antigen secretion. *Cancer research* **2004,** *64* (16), 5779-5786.

65. Papo, N.; Seger, D.; Makovitzki, A.; Kalchenko, V.; Eshhar, Z.; Degani, H.; Shai, Y., Inhibition of tumor growth and elimination of multiple metastases in human prostate and breast xenografts by systemic inoculation of a host defense–like lytic peptide. *Cancer research* **2006,** *66* (10), 5371-5378.

66. Makovitzki, A.; Fink, A.; Shai, Y., Suppression of human solid tumor growth in mice by intratumor and systemic inoculation of histidine-rich and pH-dependent host defense–like lytic peptides. *Cancer research* **2009,** *69* (8), 3458-3463.

67. Pasqua, L.; Cundari, S.; Ceresa, C.; Cavaletti, G., Recent development, applications, and perspectives of mesoporous silica particles in medicine and biotechnology. *Current medicinal chemistry* **2009,** *16* (23), 3054-3063.

68. Knežević, N. Ž.; Durand, J.-O., Large pore mesoporous silica nanomaterials for application in delivery of biomolecules. *Nanoscale* **2015,** *7* (6), 2199-2209.

69. Liu, Y.; Chen, Q.; Xu, M.; Guan, G.; Hu, W.; Liang, Y.; Zhao, X.; Qiao, M.; Chen, D.; Liu, H., single peptide ligand-functionalized uniform hollow mesoporous silica nanoparticles achieving dual-targeting drug delivery to tumor cells and angiogenic blood vessel cells. *International journal of nanomedicine* **2015,** *10*, 1855.

70. Birot, M.; Pillot, J.-P.; Dunogues, J., Comprehensive Chemistry of Polycarbosilanes, Polysilazanes, and Polycarbosilazanes as Precursors of Ceramics. *Chem. Rev. (Washington, D. C.)* **1995,** *95* (5), 1443-77.

71. Laine, R. M.; Blum, Y. D.; Tse, D.; Glaser, R., Synthetic routes to oligosilazanes and polysilazanes. Polysilazane precursors to silicon nitride. *ACS Symp. Ser.* **1988,** *360* (Inorg. Organomet. Polym.), 124-42.

72. Soum, A. In *Polysilazanes*, Kluwer Academic Publishers: 2000; pp 323-349.

73. Hein, C. D.; Liu, X.-M.; Wang, D., Click Chemistry, a Powerful Tool for Pharmaceutical Sciences. *Pharmaceutical research* **2008,** *25* (10), 2216-2230.

74. Yu, J. Therapeutic Peptides Against Cancer: Synthesis and Optimized Delivery. Kansas State University, Manhattan, KS, 2017.

75. https://mai.ku.edu/.

76. https://www.thermofisher.com/us/en/home/references/protocols/cell-culture/mtt-assay-protocol/vybrant-mtt-cell-proliferation-assay-kit.html.

77. http://www.dtp.nci.nih.gov/.

78. Ourednik, J.; Ourednik, V.; Lynch, W. P.; Schachner, M.; Snyder, E. Y., Neural stem cells display an inherent mechanism for rescuing dysfunctional neurons. *Nat. Biotechnol.* **2002,** *20* (11), 1103-1110.

79. https://www.atcc.org/products/all/CRL-2539.aspx.

80. https://www.graphpad.com/support/prism-5-updates/.

81. https://www.perkinelmer.com/lab-solutions/resources/docs/faq_beginners-guide-to-thermogravimetric-analysis_009380c_01.pdf.

82. Watermann, A.; Brieger, J., Mesoporous Silica Nanoparticles as Drug Delivery Vehicles in Cancer. *Nanomaterials* **2017,** *7* (7), 189.

83. Bagó, J. R.; Okolie, O.; Dumitru, R.; Ewend, M. G.; Parker, J. S.; Vander Werff, R.; Underhill, T. M.; Schmid, R. S.; Miller, C. R.; Hingtgen, S. D., Tumor-homing cytotoxic human induced neural stem cells for cancer therapy. *Science translational medicine* **2017,** *9* (375), eaah6510.

84. Zhang, J. Y., Apoptosis-based anticancer drugs. *Nat Rev Drug Discov* **2002,** *1* (2), 101-2.

85. Fink, S. L.; Cookson, B. T., Apoptosis, pyroptosis, and necrosis: mechanistic description of dead and dying eukaryotic cells. *Infect. Immun.* **2005,** *73* (4), 1907-1916.

86. http://www.gfmer.ch/ Geneva Foundation for Medical Education and Research.

87. Alshetaiwi, H. S.; Balivada, S.; Shrestha, T. B.; Pyle, M.; Basel, M. T.; Bossmann, S. H.; Troyer, D. L., Luminol-based bioluminescence imaging of mouse mammary tumors. *J. Photochem. Photobiol., B* **2013,** *127*, 223-228.

88. Curto, S.; Faridi, P.; Prakash, P.; Shrestha, T. B.; Pyle, M.; Troyer, D.; Maurmann, L.; Bossmann, S. H., An integrated platform for small-animal hyperthermia investigations under ultra-high-field MRI guidance. *Int J Hyperthermia* **2017**, 1-11.

89. Malalasekera, A. P.; Wang, H.; Samarakoon, T. N.; Udukala, D. N.; Yapa, A. S.; Ortega, R.; McLaurin, E. J.; Shrestha, T. B.; Alshetaiwi, H.; Troyer, D. L.; Bossmann, S. H., A nanobiosensor for the detection of arginase activity. *Nanomedicine* **2017,** *13* (2), 383-390.

90. Riss, T. L.; Moravec, R. A.; Niles, A. L.; Duellman, S.; Benink, H. A.; Worzella, T. J.; Minor, L., Cell viability assays. **2016**.

91. Goodsell, D. S., Inside a living cell. *Trends in biochemical sciences* **1991,** *16*, 203-206.

92. Doherty, G. J.; McMahon, H. T., Mechanisms of endocytosis. *Annual review of biochemistry* **2009,** *78*, 857-902.

93. Hegde, M.; Roscoe, J.; Cala, P.; Gorin, F., Amiloride kills malignant glioma cells independent of its inhibition of the sodium-hydrogen exchanger. *Journal of Pharmacology and Experimental Therapeutics* **2004,** *310* (1), 67-74.

94. Tong, W.; Welsh, W. J.; Shi, L.; Fang, H.; Perkins, R., Structure-activity relationship approaches and applications. *Environ Toxicol Chem* **2003,** *22* (8), 1680-95.
95. Pouny, Y.; Rapaport, D.; Mor, A.; Nicolas, P.; Shai, Y., Interaction of antimicrobial dermaseptin and its fluorescently labeled analogs with phospholipid membranes. *Biochemistry* **1992,** *31* (49), 12416-23.
96. Gamrekelashvili, J.; Greten, T. F.; Korangy, F., Immunogenicity of necrotic cell death. *Cell. Mol. Life Sci.* **2015,** *72* (2), 273-283.

Appendix A - TOCSY-NOESY walk: identification of SALK*L*LK*K*L*LK*KLL*K*LLA

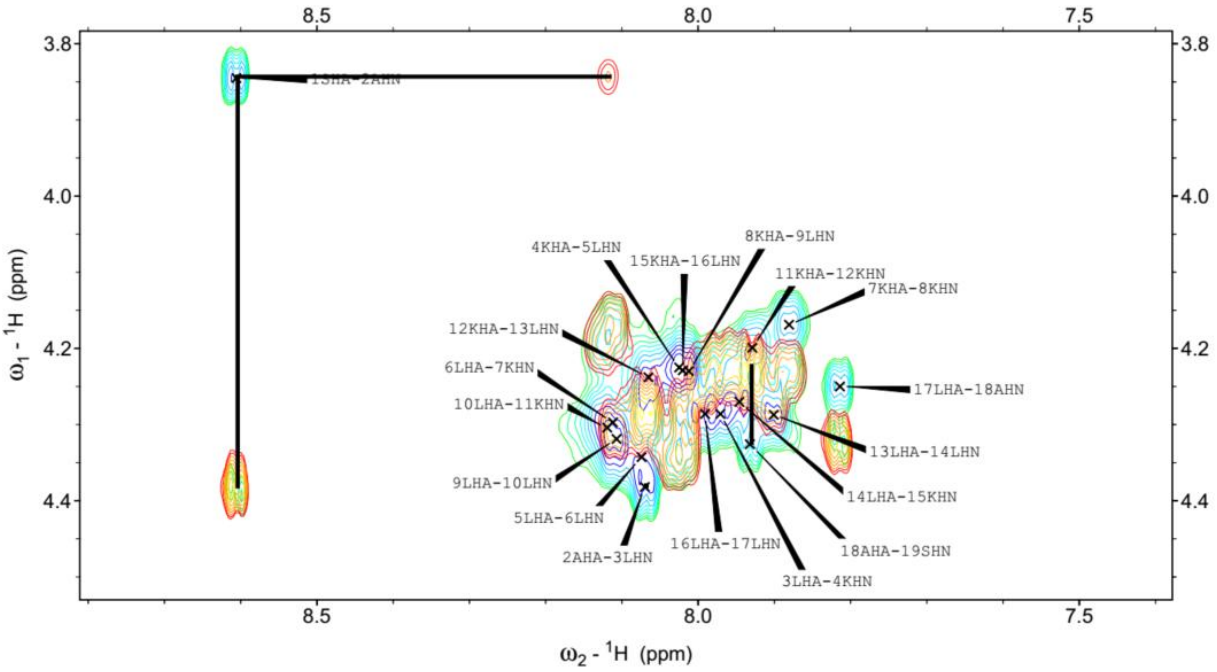

TOCSY-NOESY walk: residue 1-2.

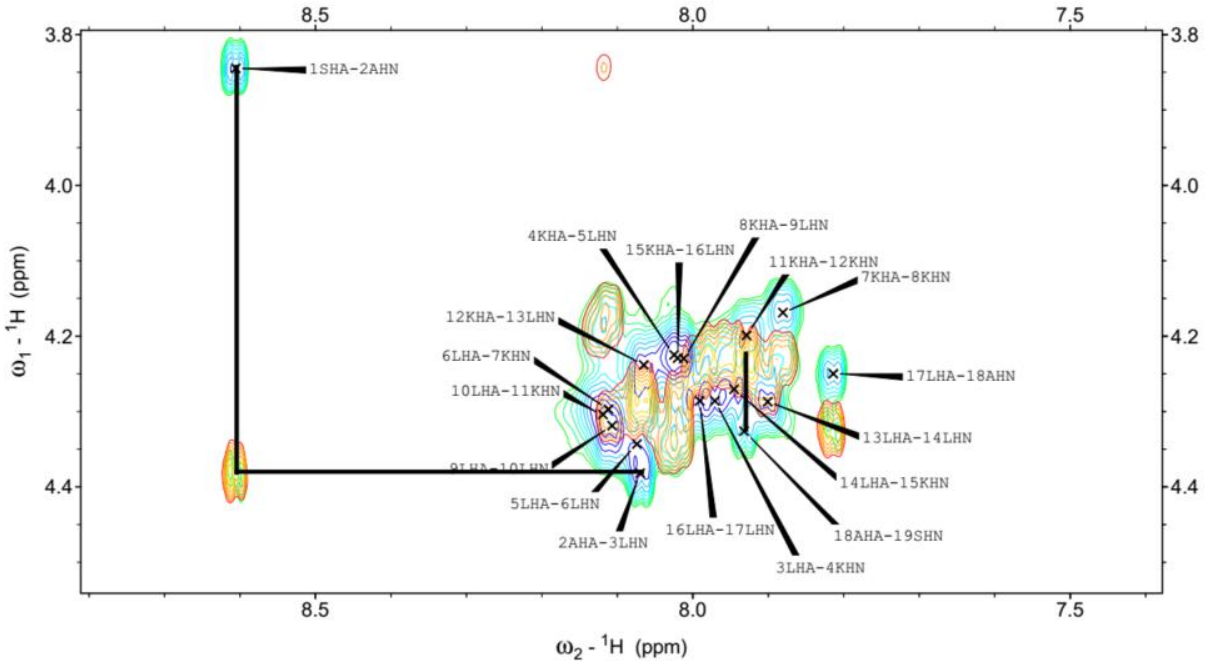

TOCSY-NOESY walk: residue 2.

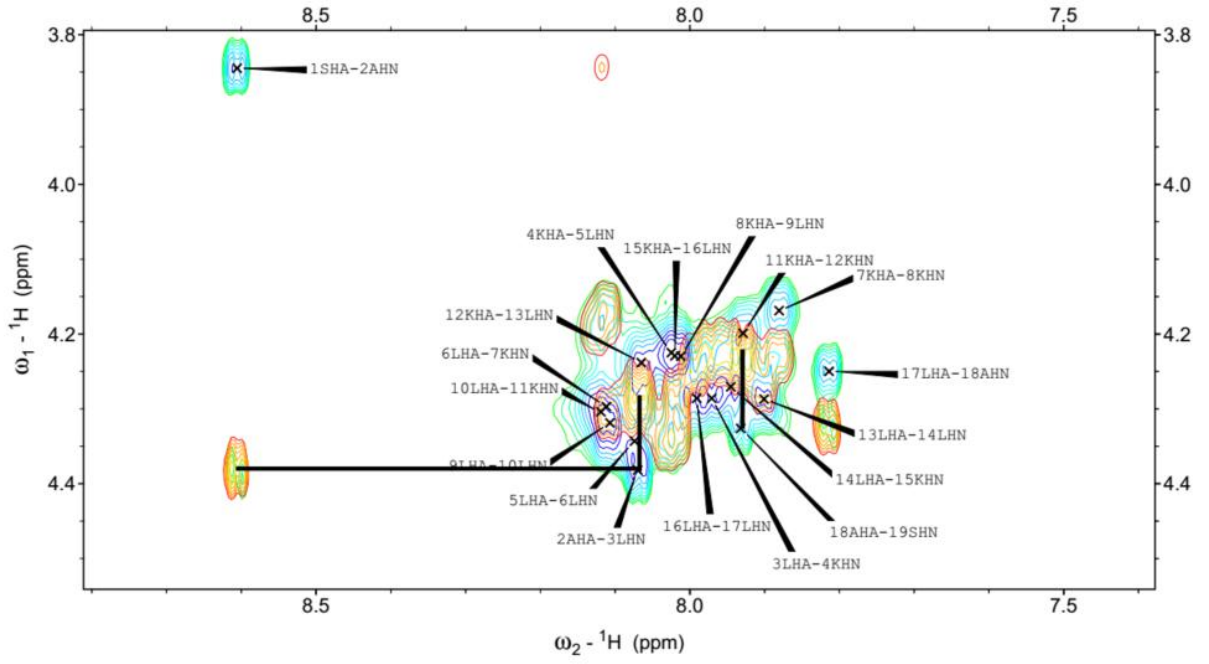

TOCSY-NOESY walk: residue 2-3.

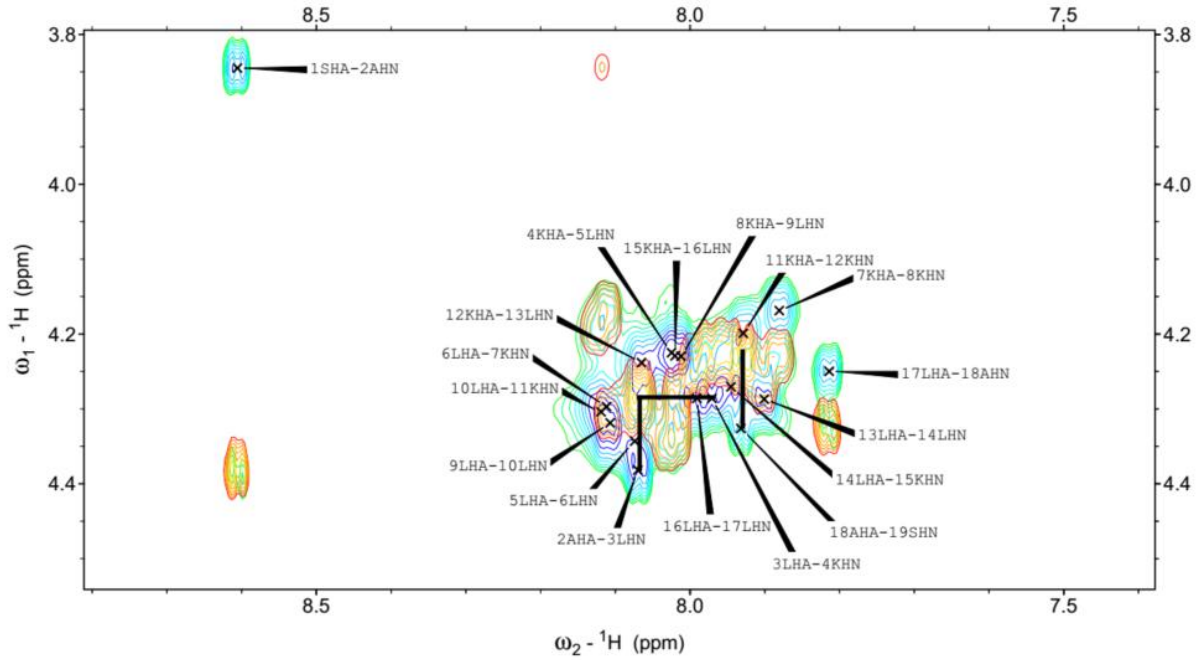

TOCSY-NOESY walk: residue 3.

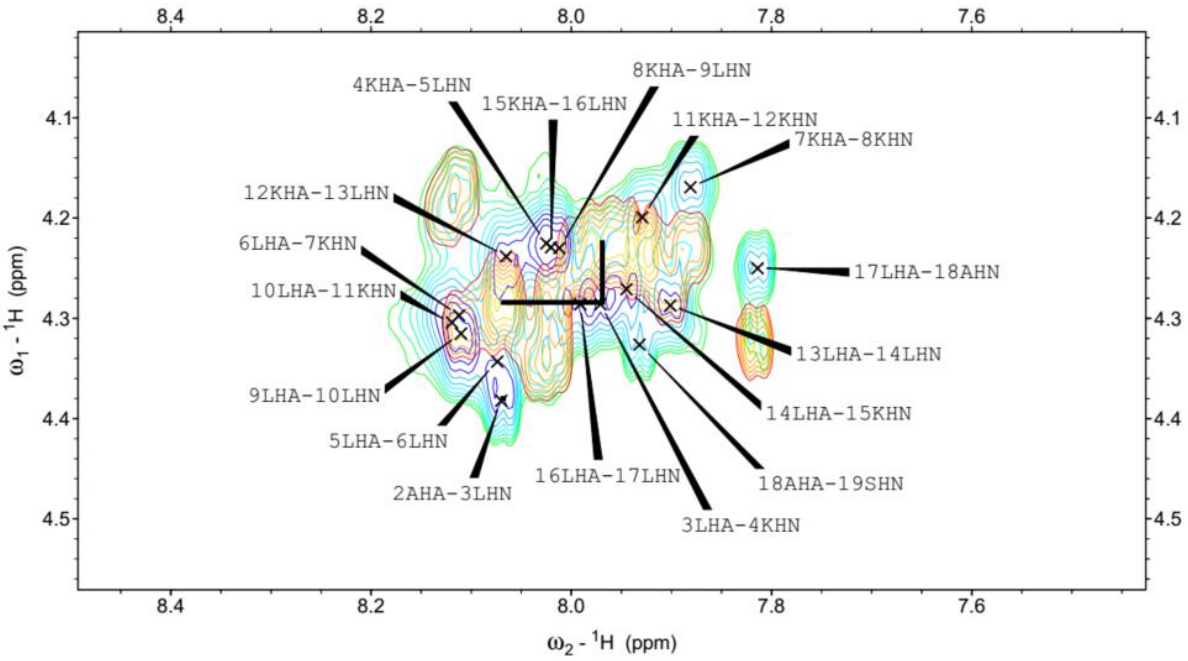

TOCSY-NOESY walk: residue 3-4.

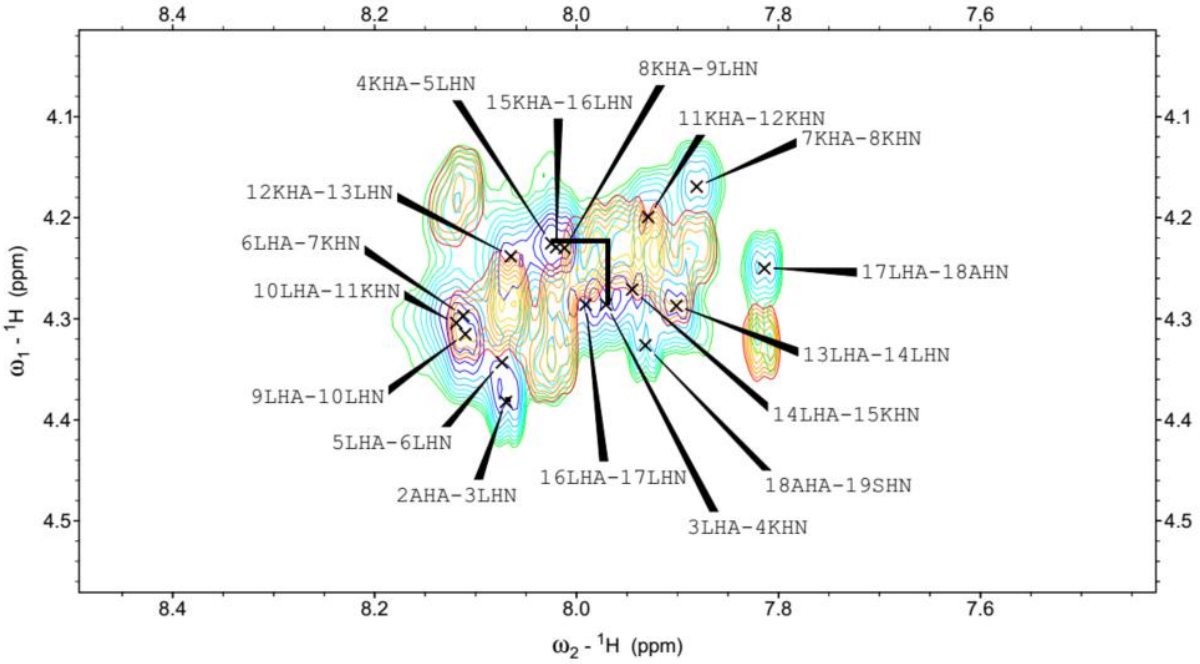

TOCSY-NOESY walk: residue 4.

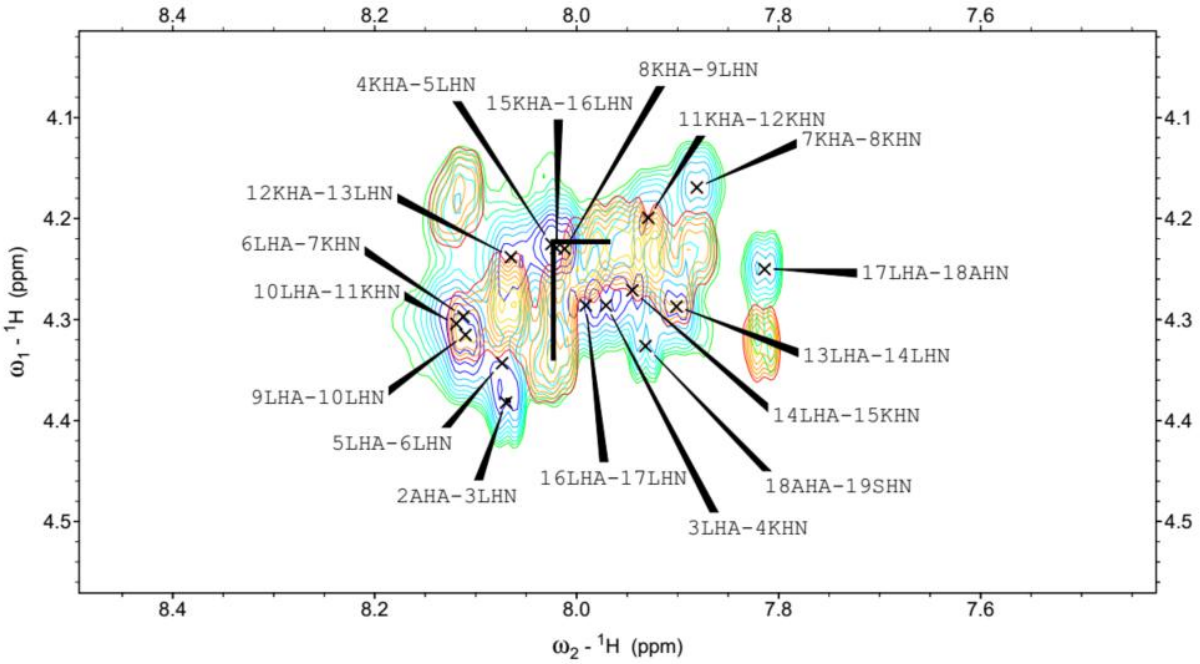

TOCSY-NOESY walk: residue 4-5.

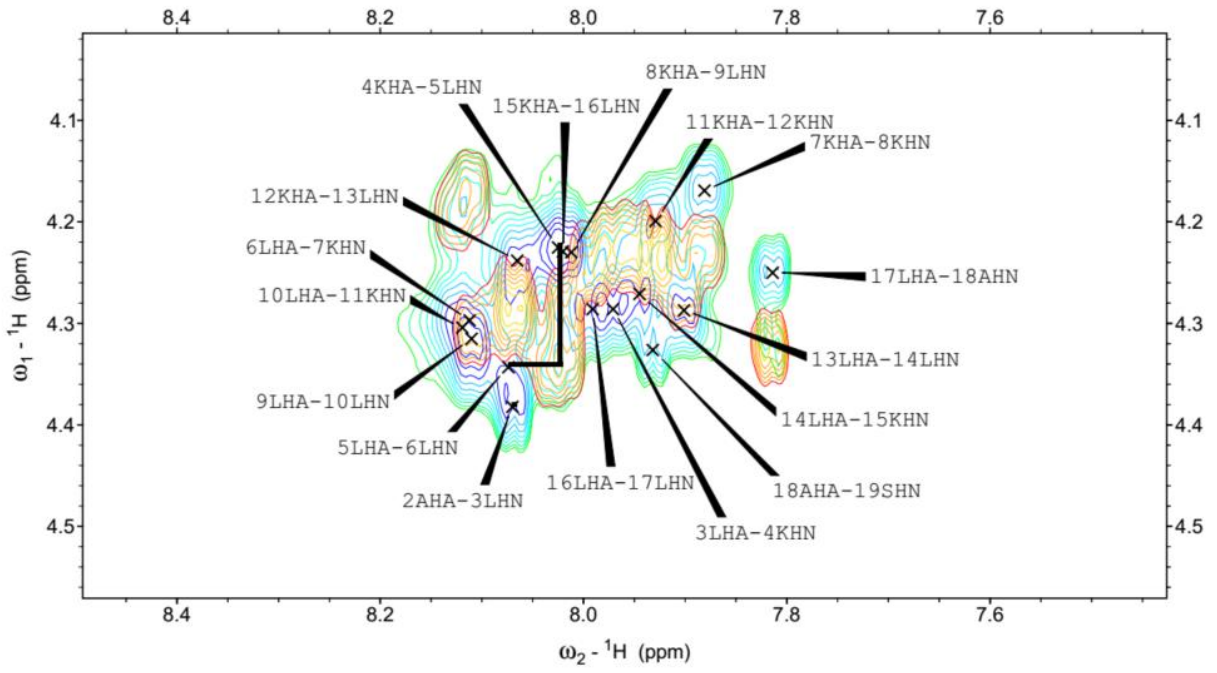

TOCSY-NOESY walk: residue 5.

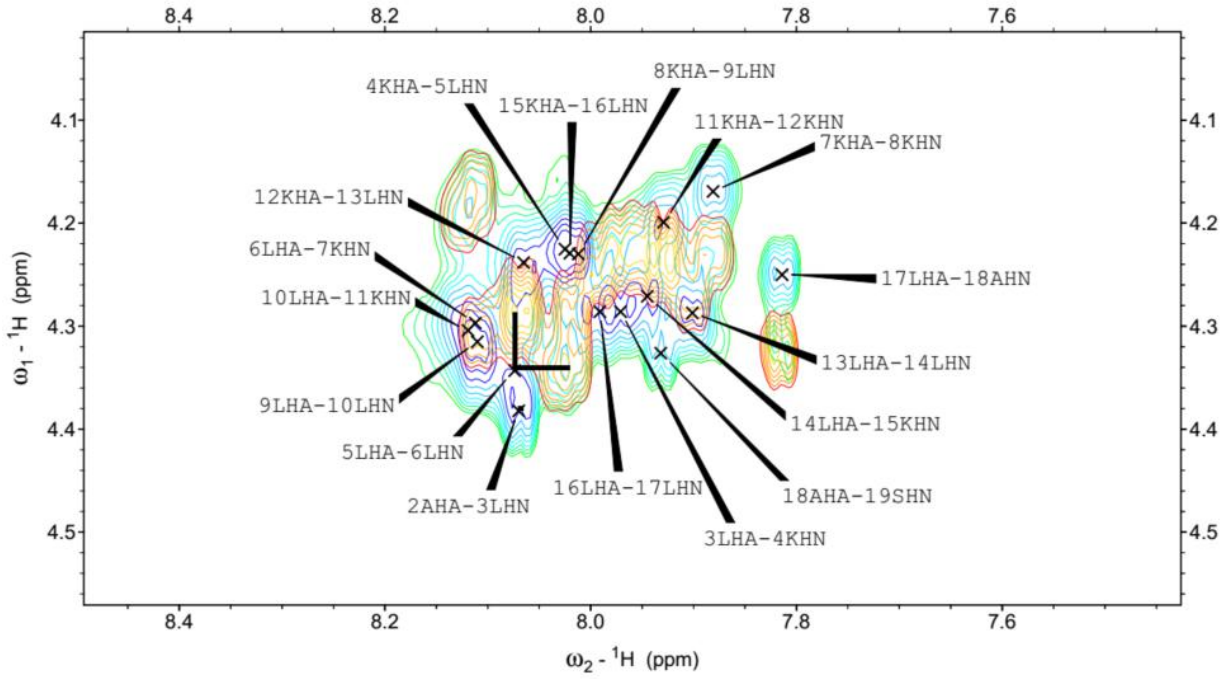

TOCSY-NOESY walk: residue 5-6.

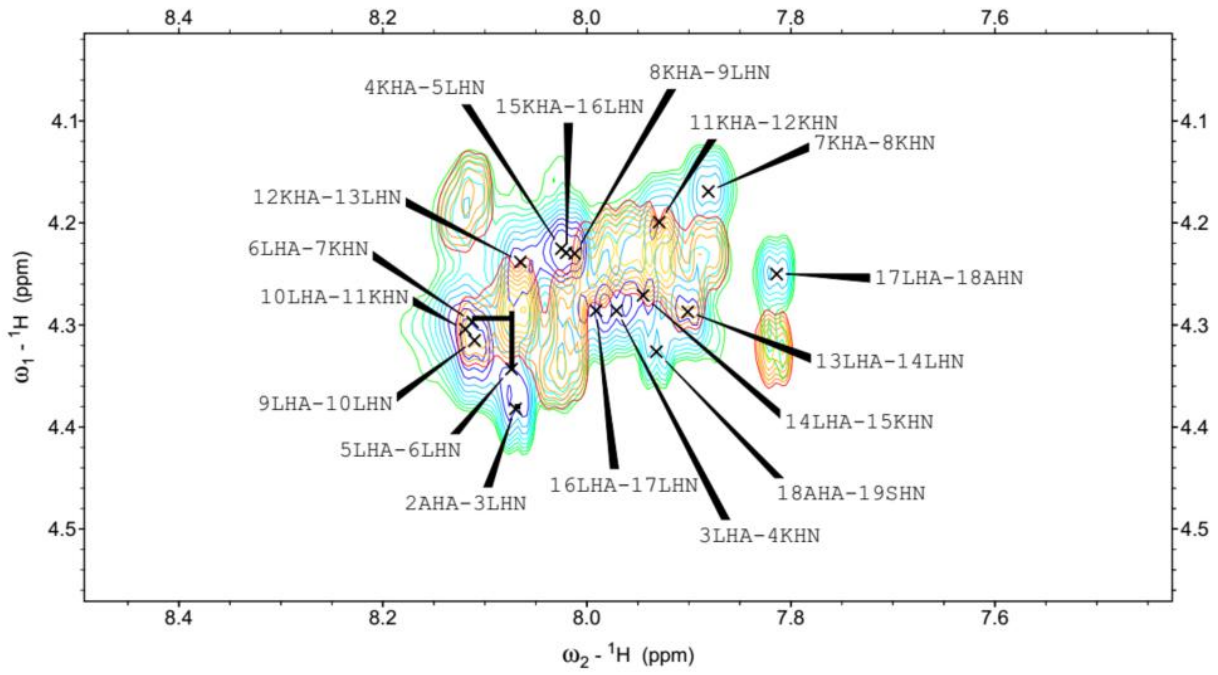

TOCSY-NOESY walk: residue 6.

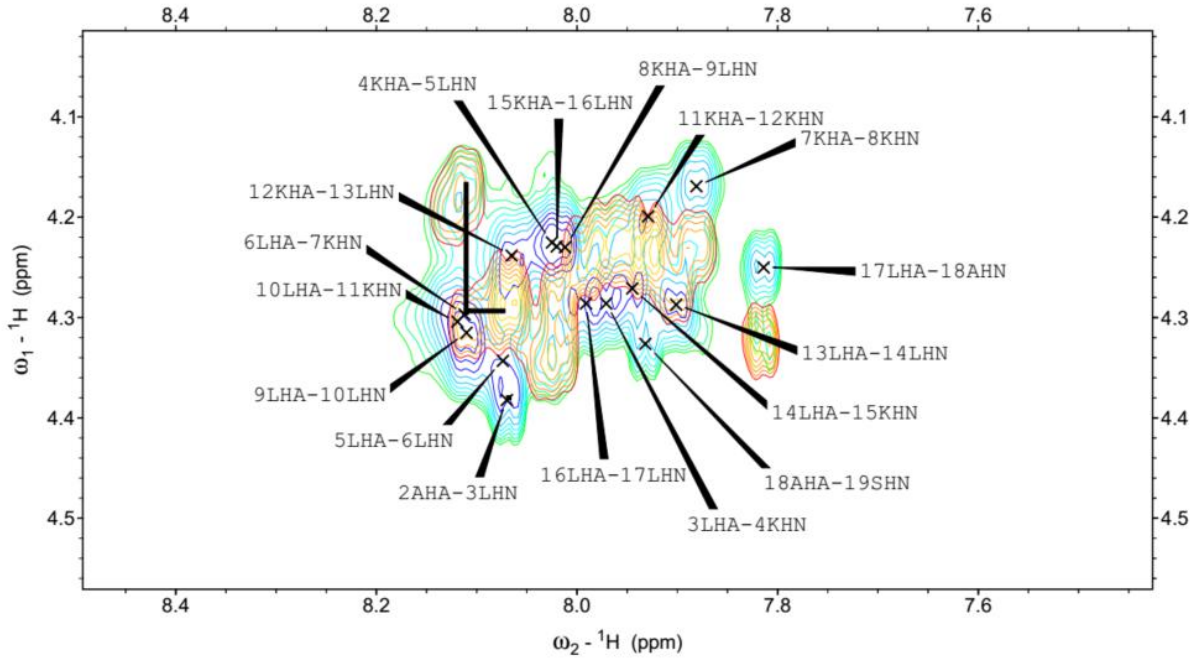

TOCSY-NOESY walk: residue 6-7.

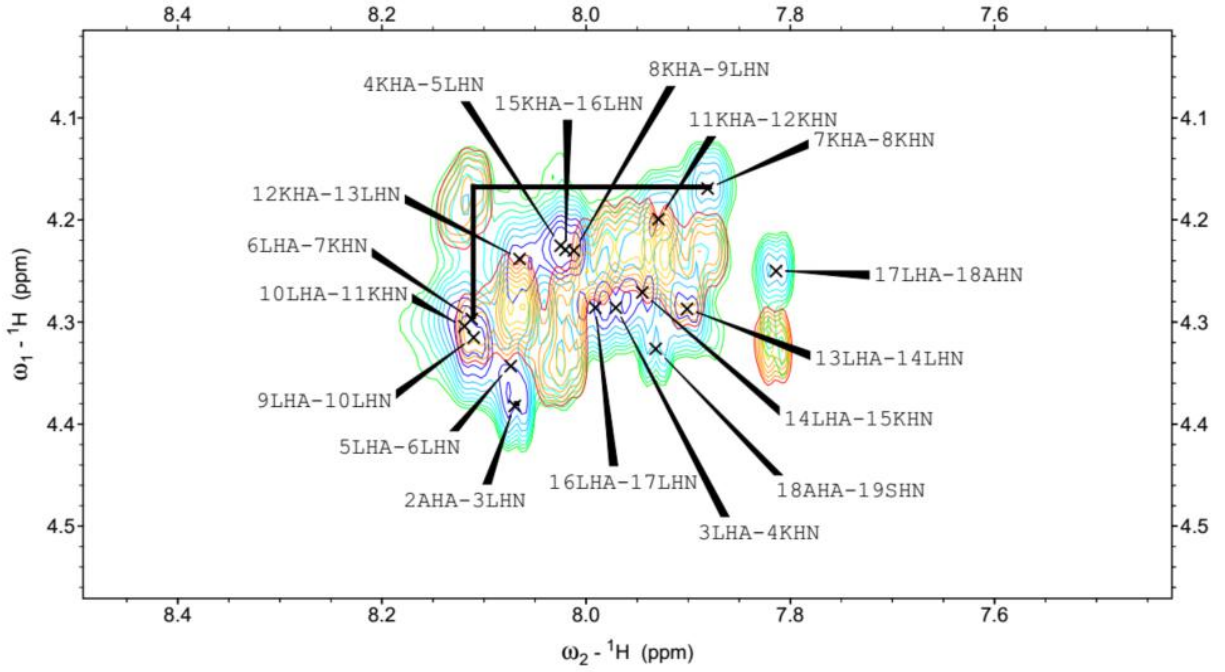

TOCSY-NOESY walk: residue 7.

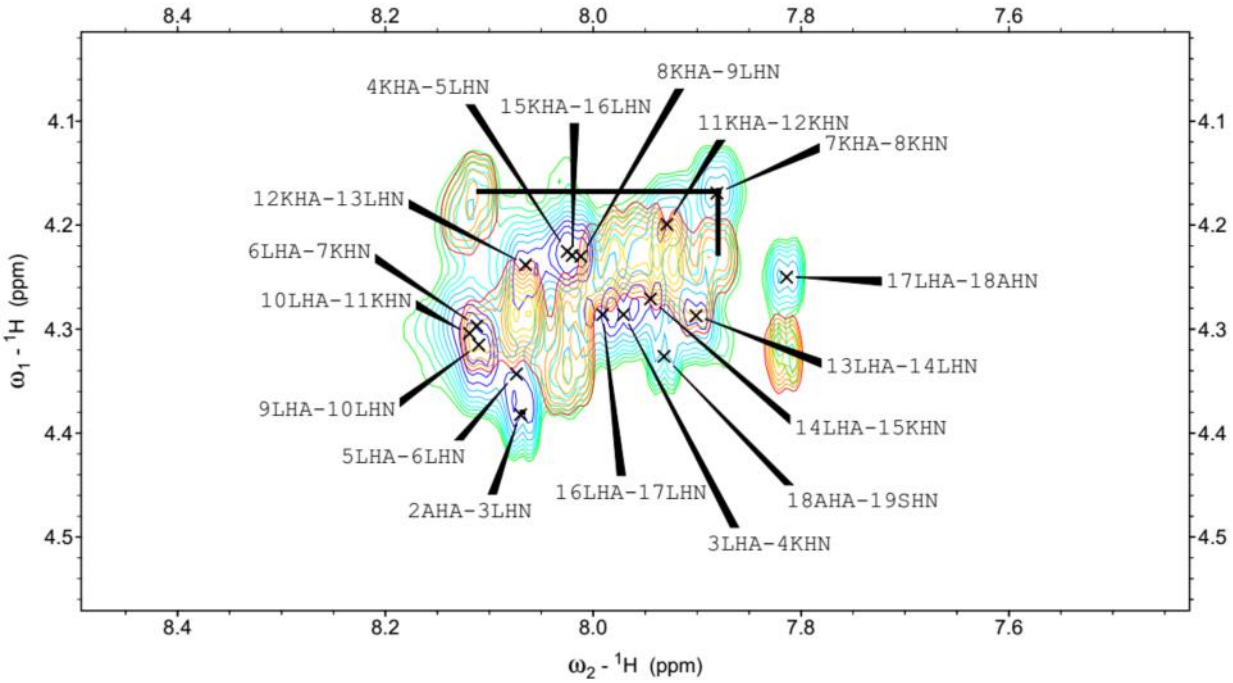

TOCSY-NOESY walk: residue 7-8.

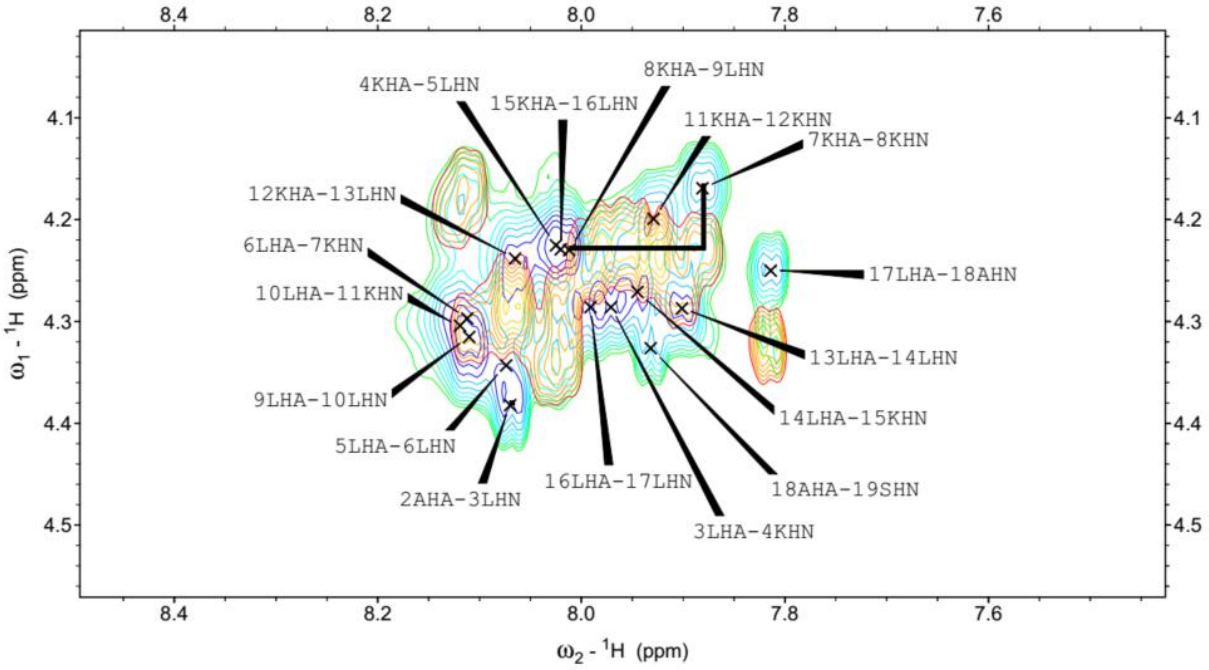

TOCSY-NOESY walk: residue 8.

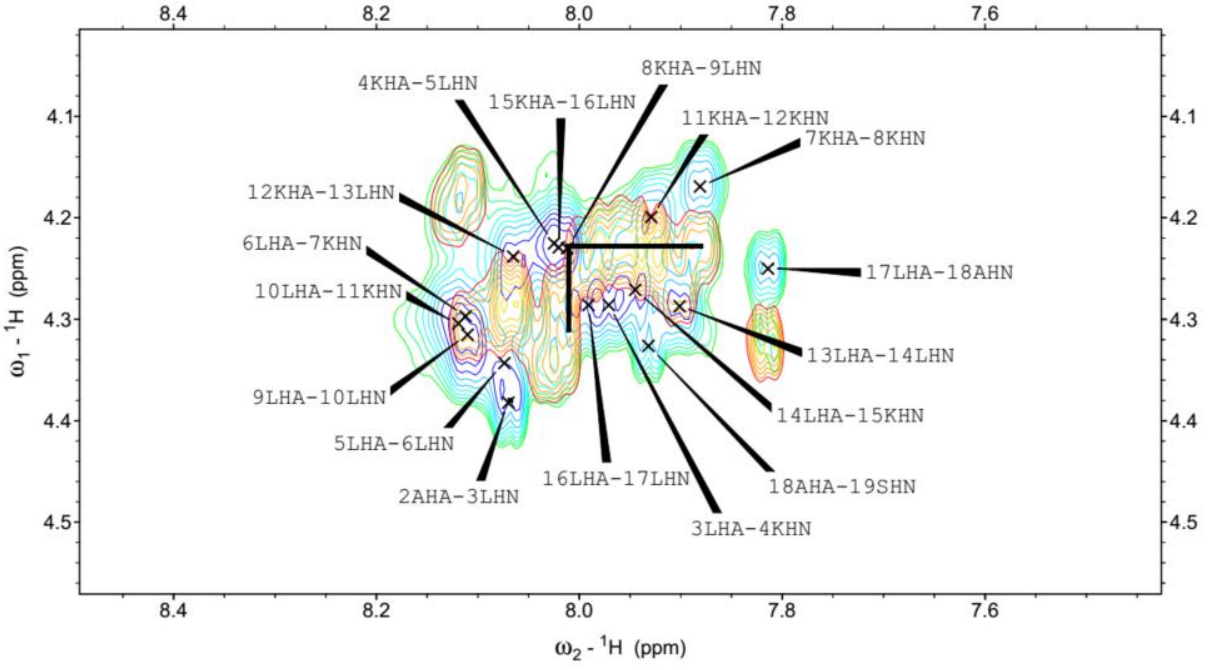

TOCSY-NOESY walk: residue 8-9.

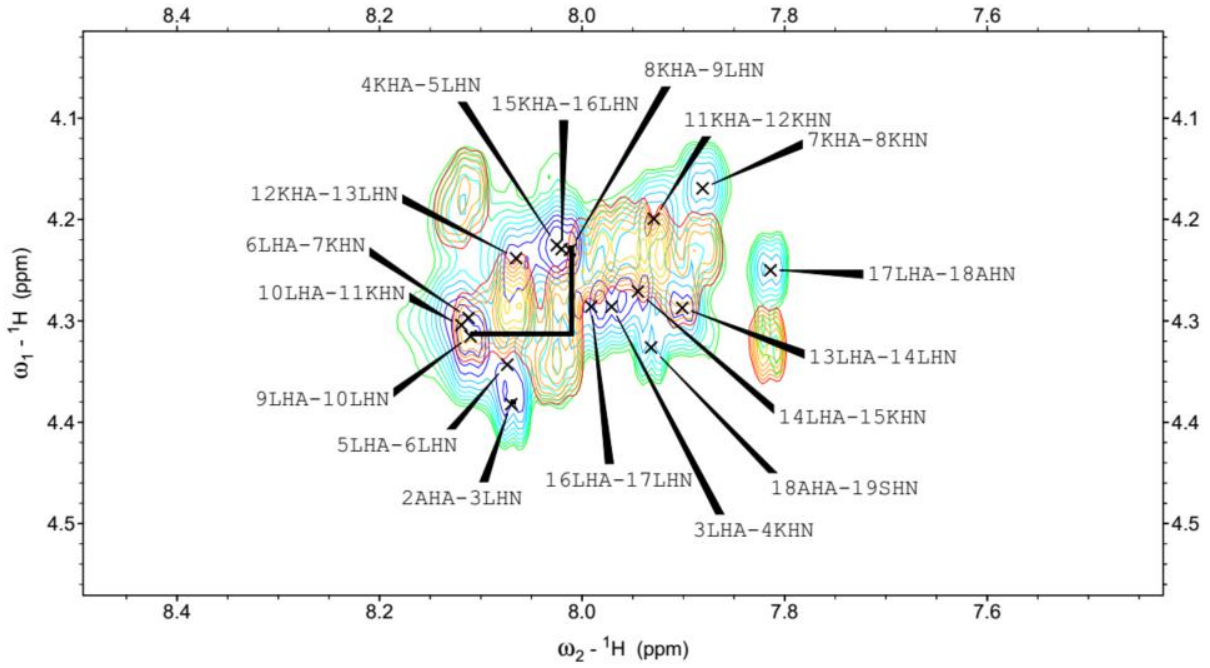

TOCSY-NOESY walk: residue 9.

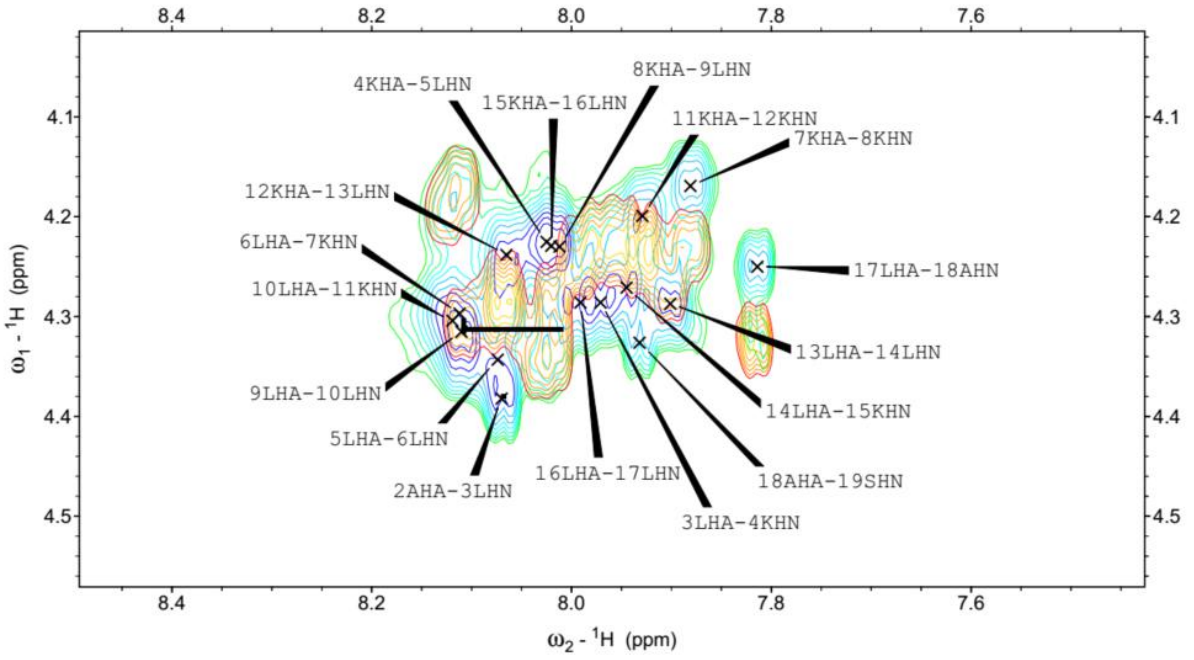

TOCSY-NOESY walk: residue 9-10.

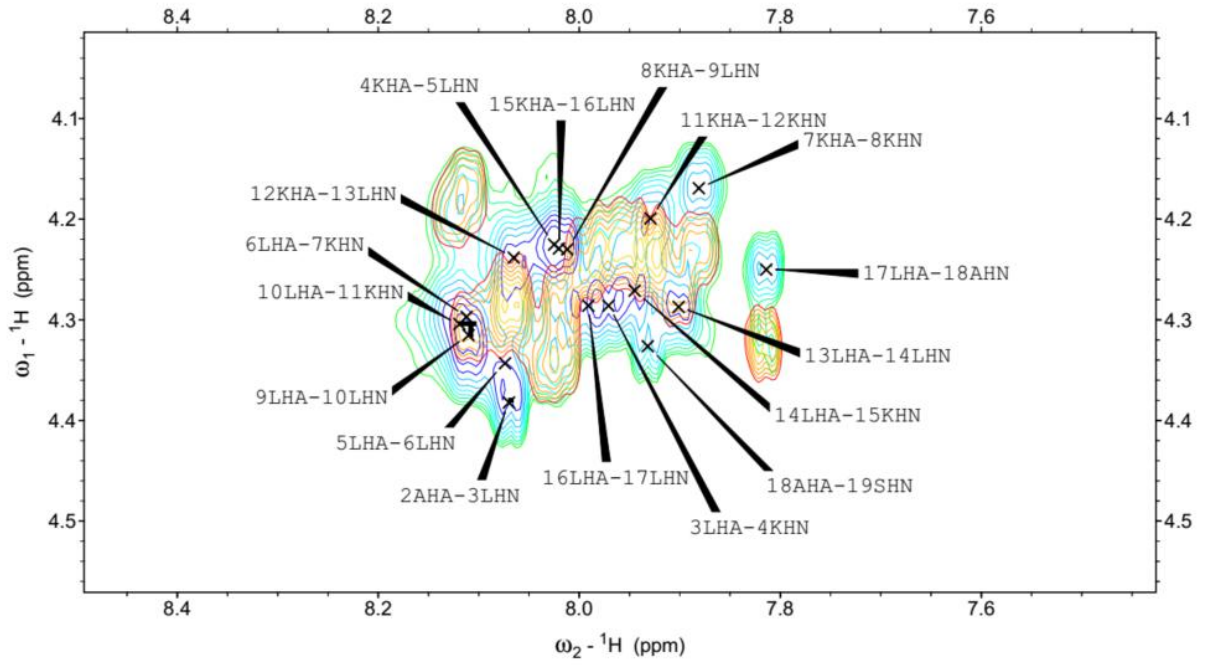

TOCSY-NOESY walk: residue 10.

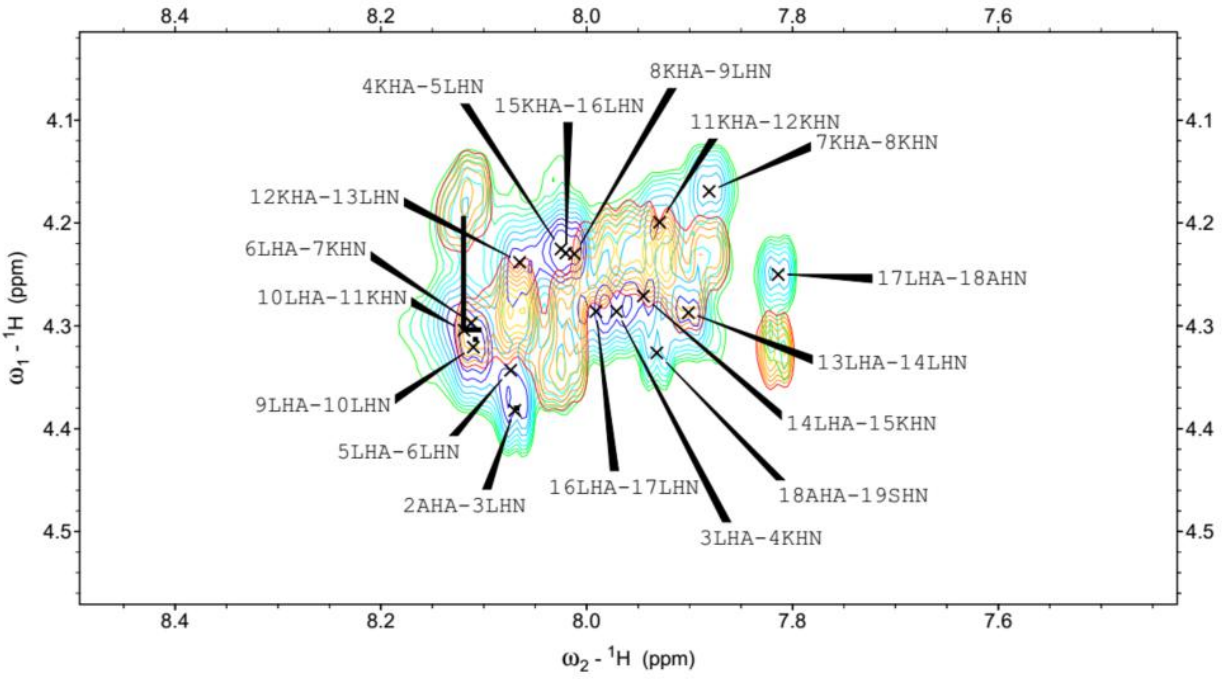

TOCSY-NOESY walk: residue 10-11.

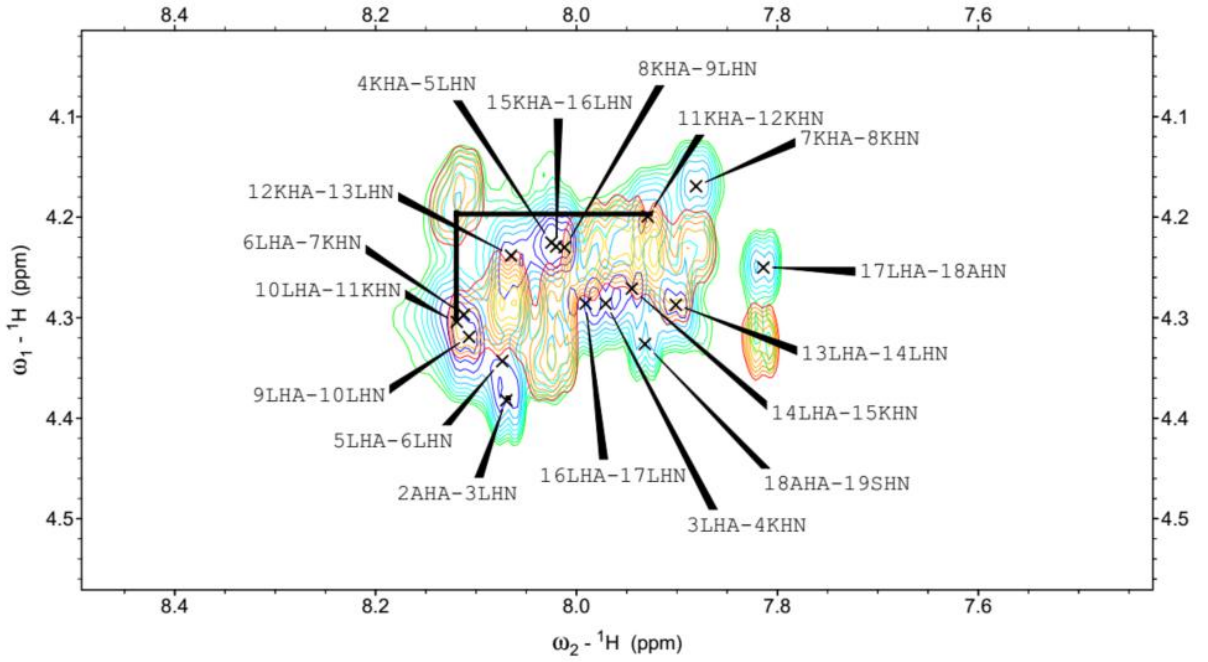

TOCSY-NOESY walk: residue 11.

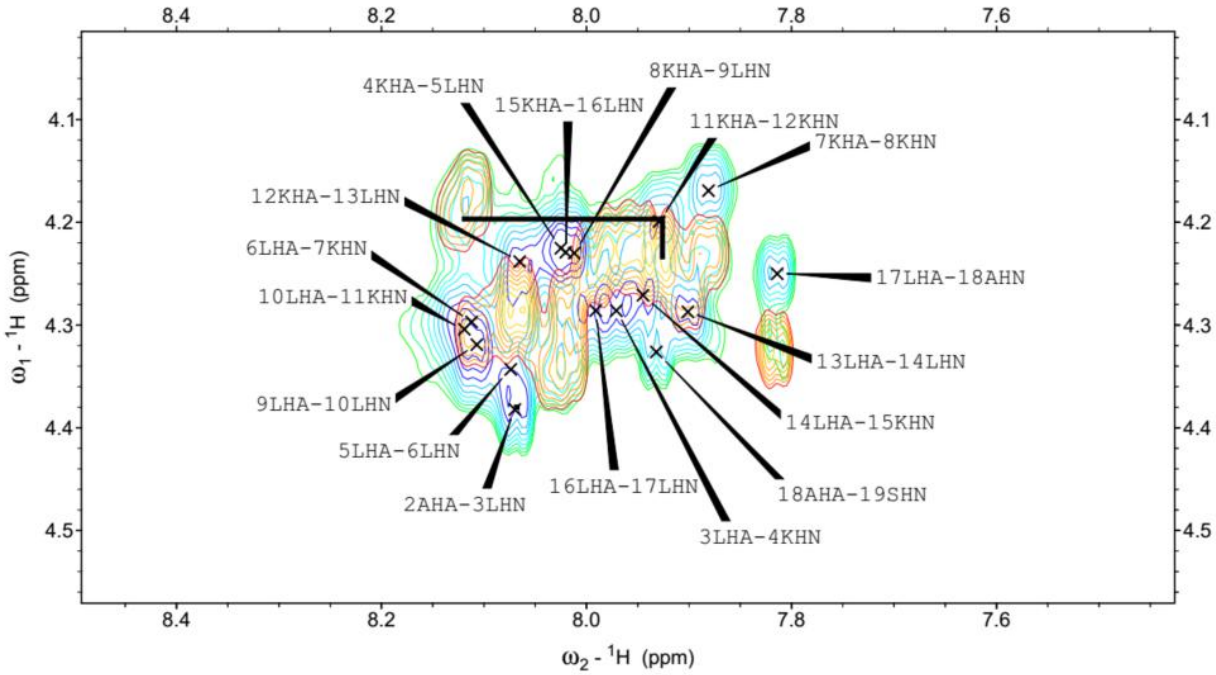

TOCSY-NOESY walk: residue 11-12.

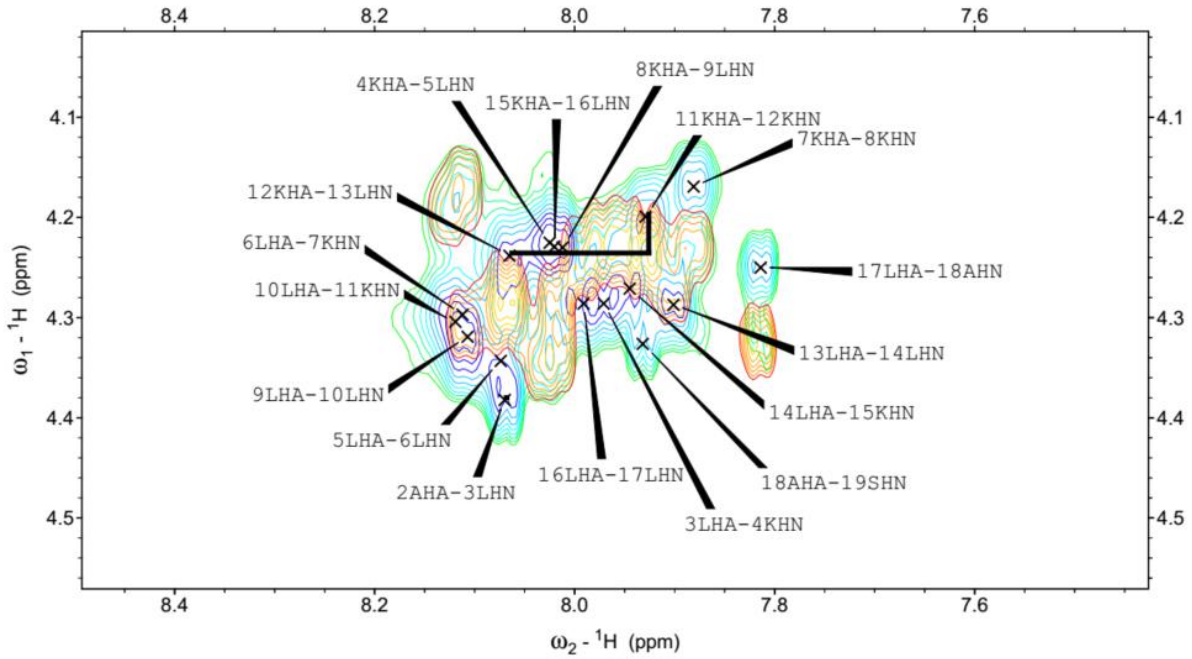

TOCSY-NOESY walk: residue 12.

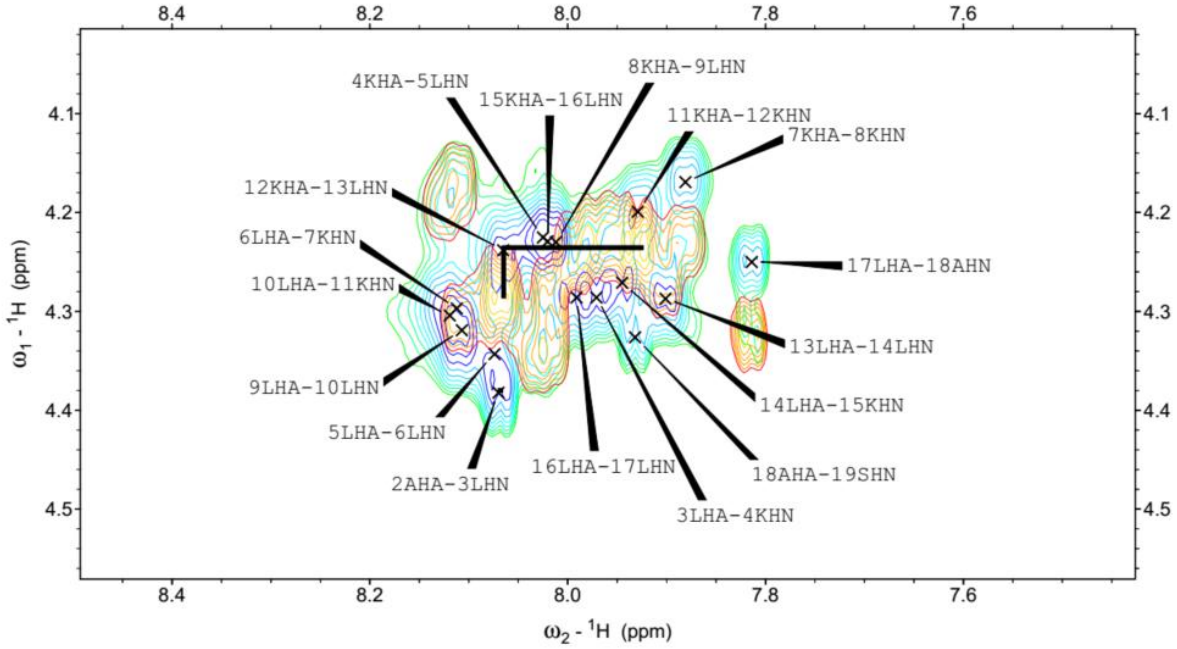

TOCSY-NOESY walk: residue 12-13.

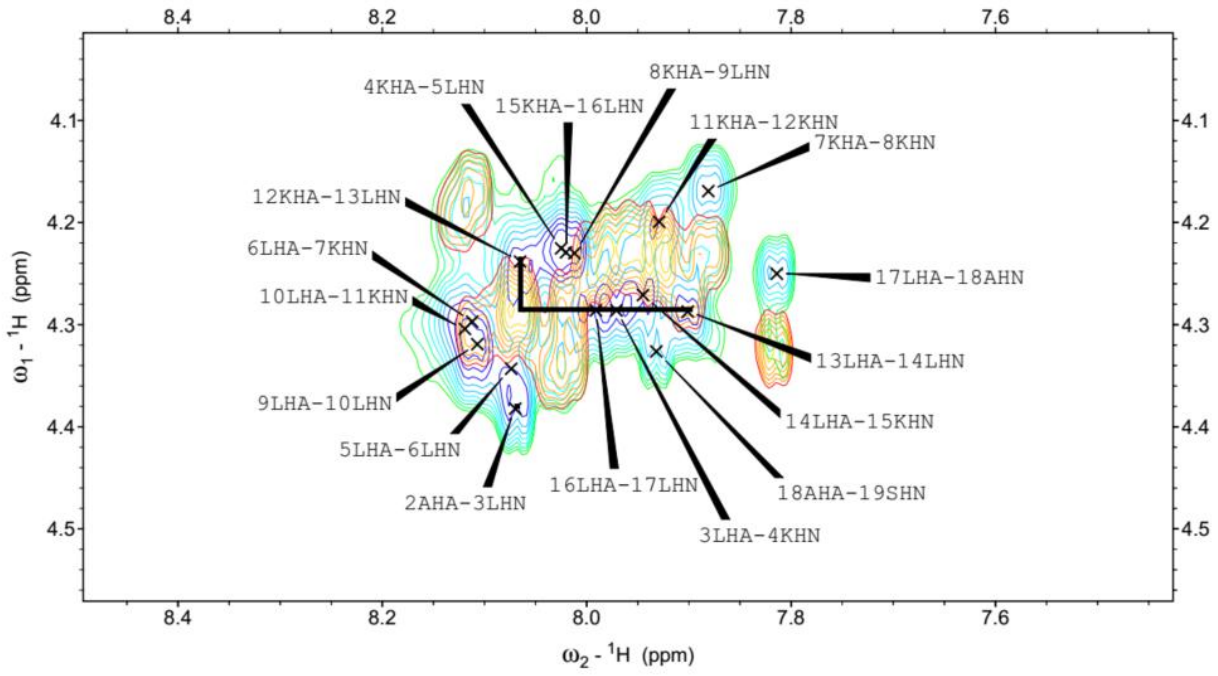

TOCSY-NOESY walk: residue 13.

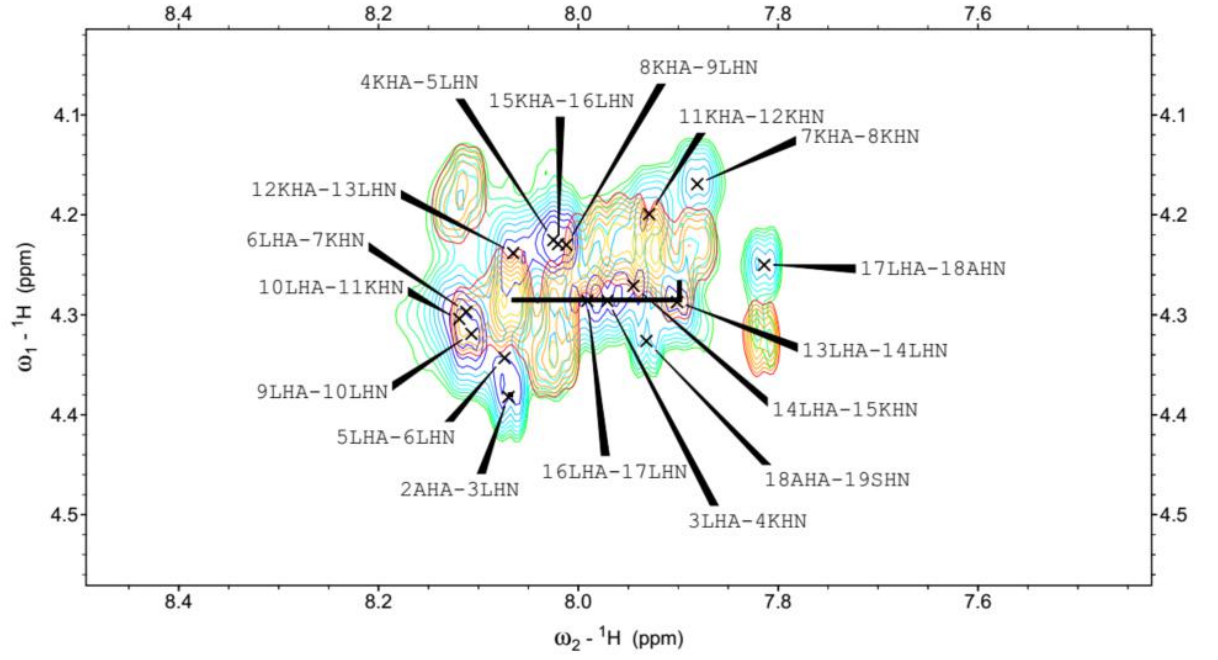

TOCSY-NOESY walk: residue 13-14.

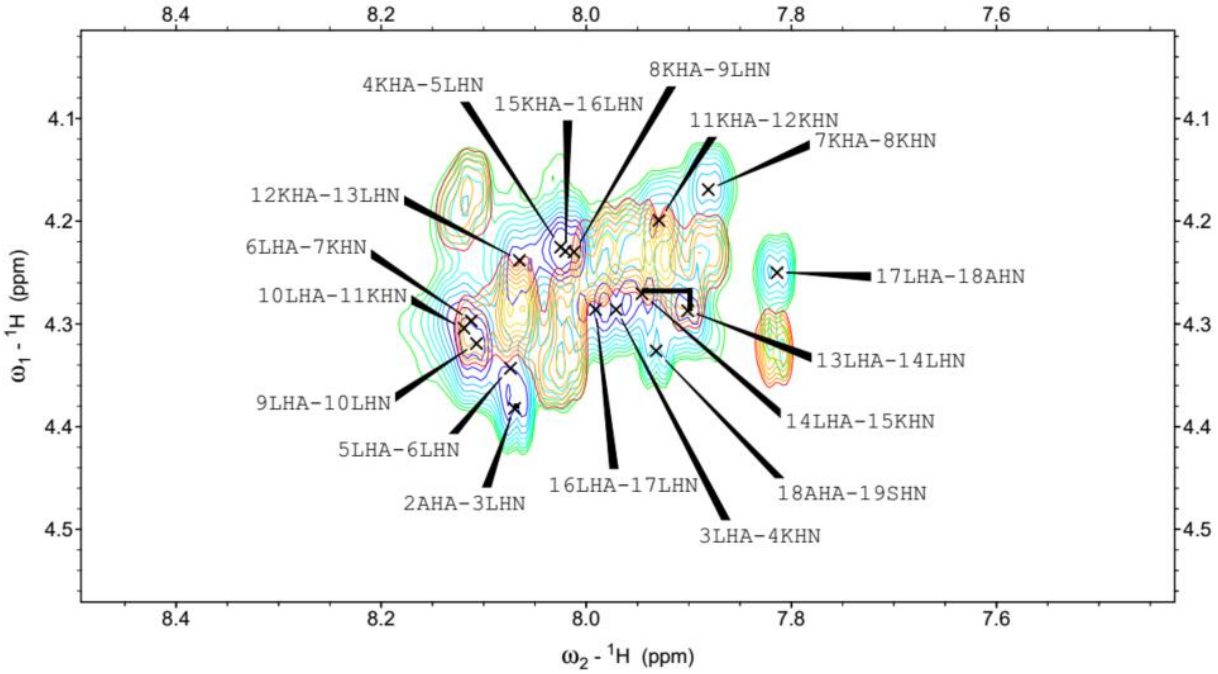

TOCSY-NOESY walk: residue 14.

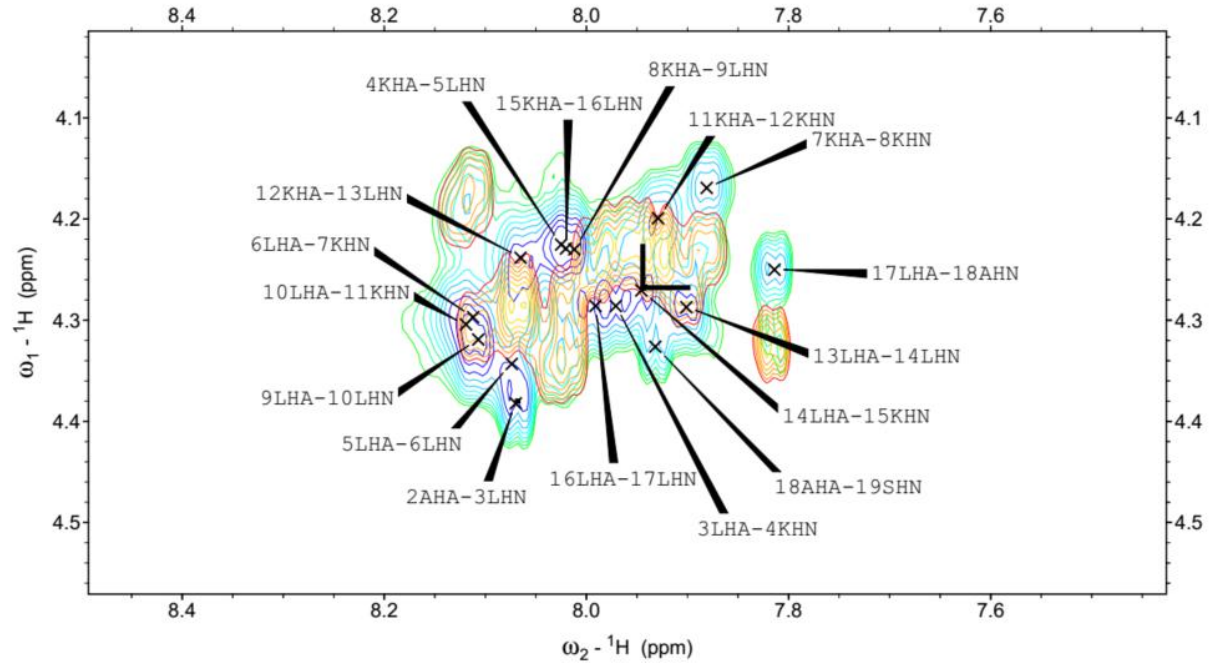

TOCSY-NOESY walk: residue 14-15.

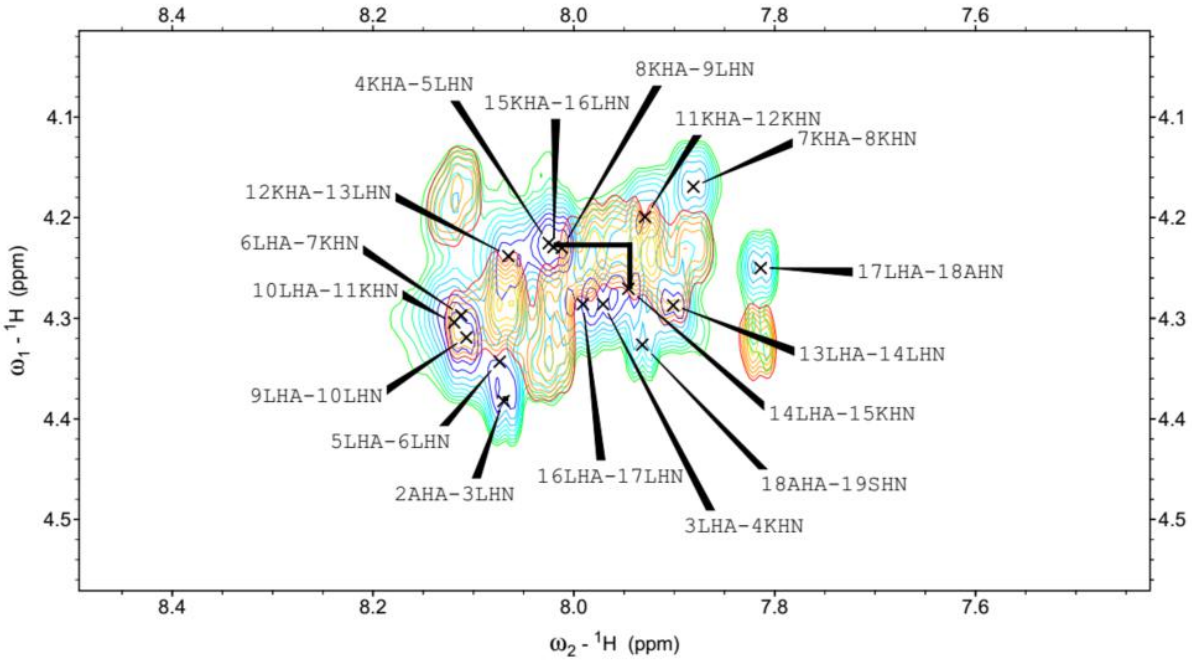

TOCSY-NOESY walk: residue 15.

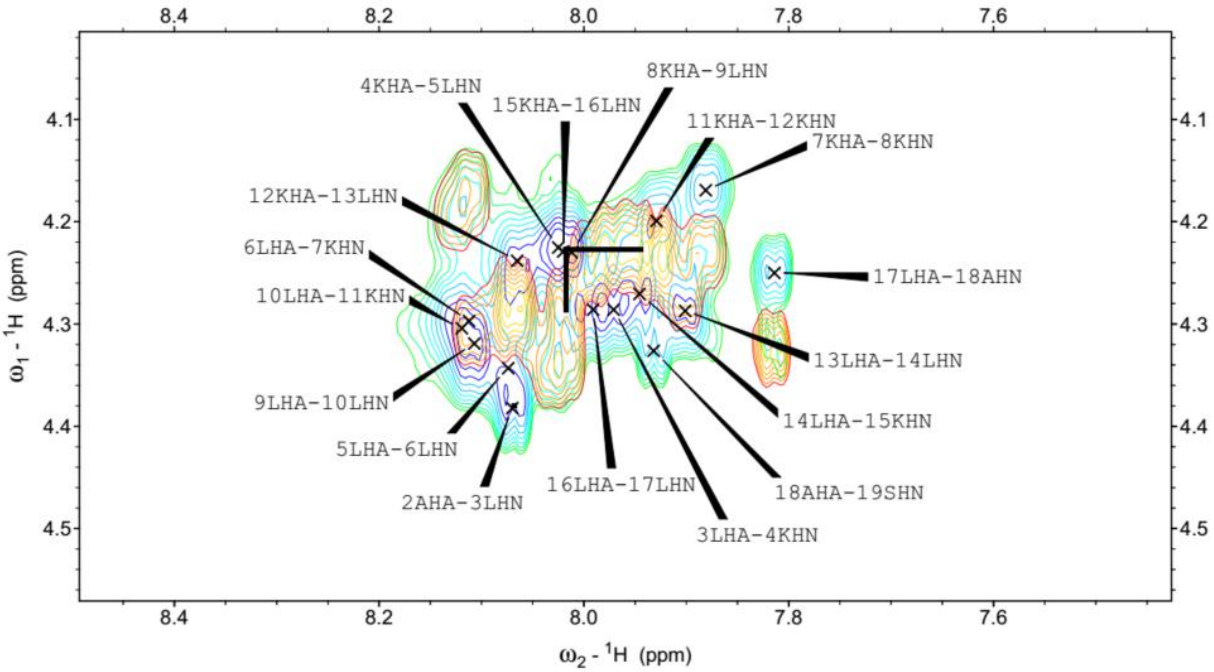

TOCSY-NOESY walk: residue 15-16.

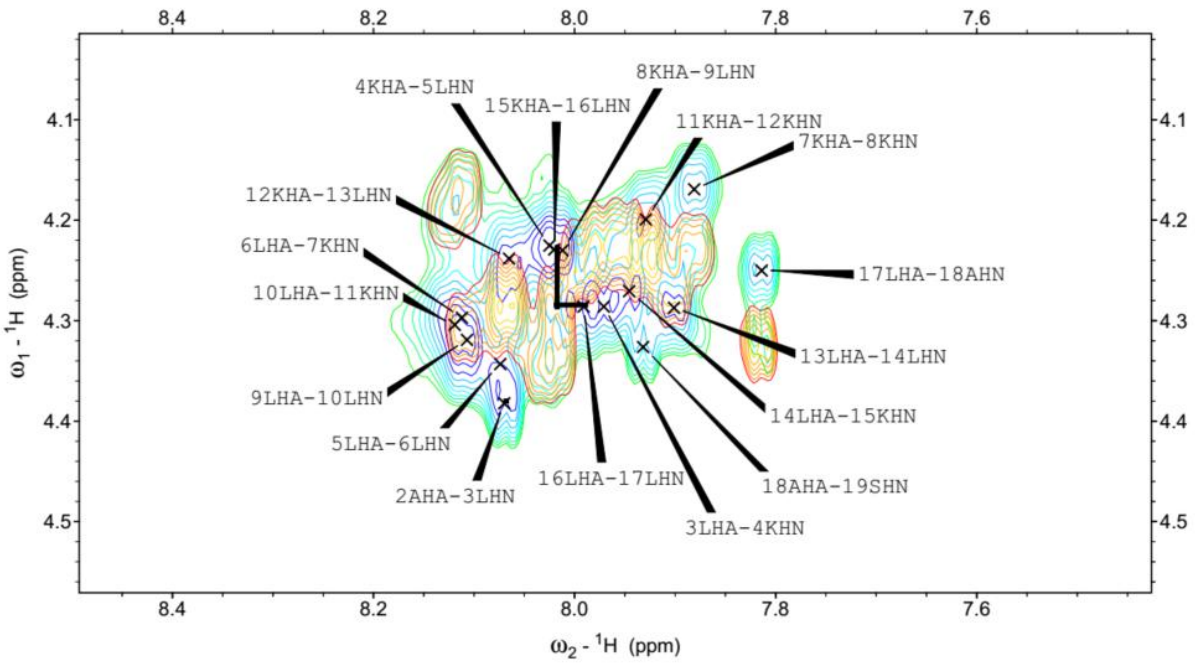

TOCSY-NOESY walk: residue 16.

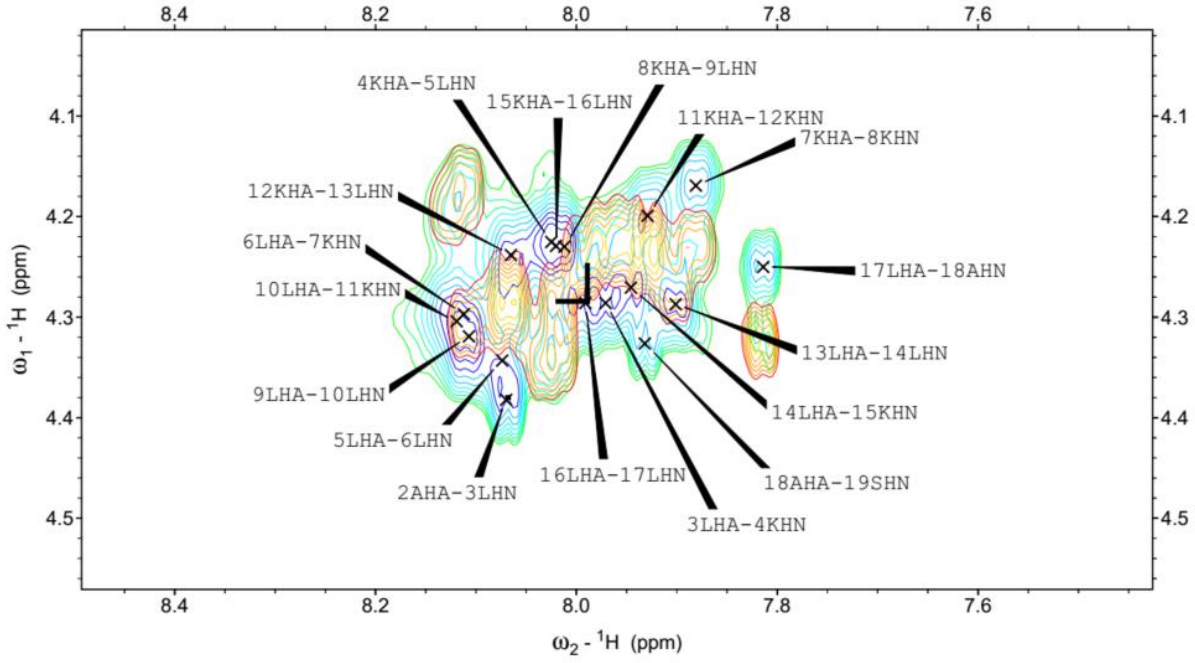

TOCSY-NOESY walk: residue 16-17.

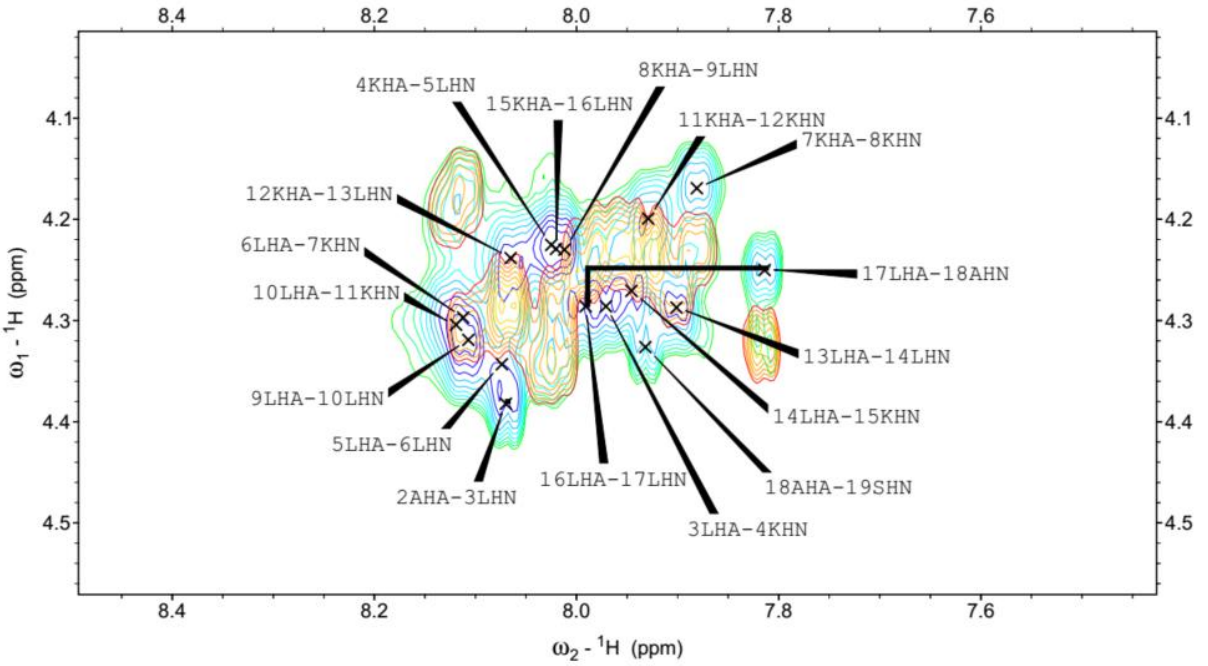

TOCSY-NOESY walk: residue 17.

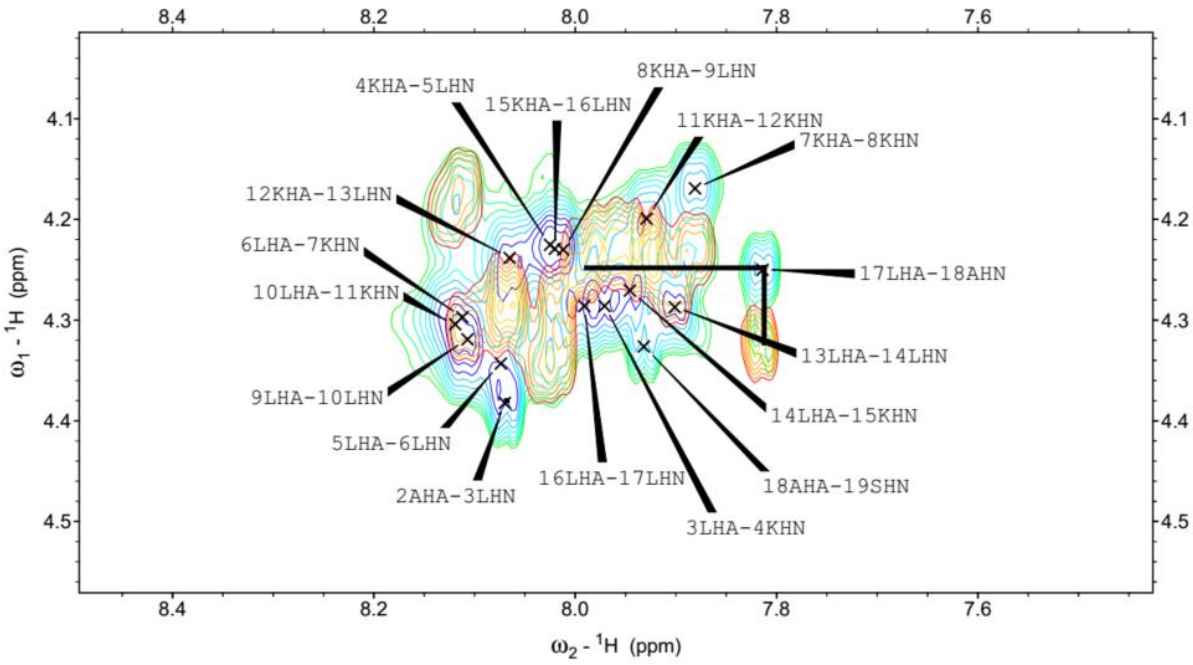

TOCSY-NOESY walk: residue 17-18.

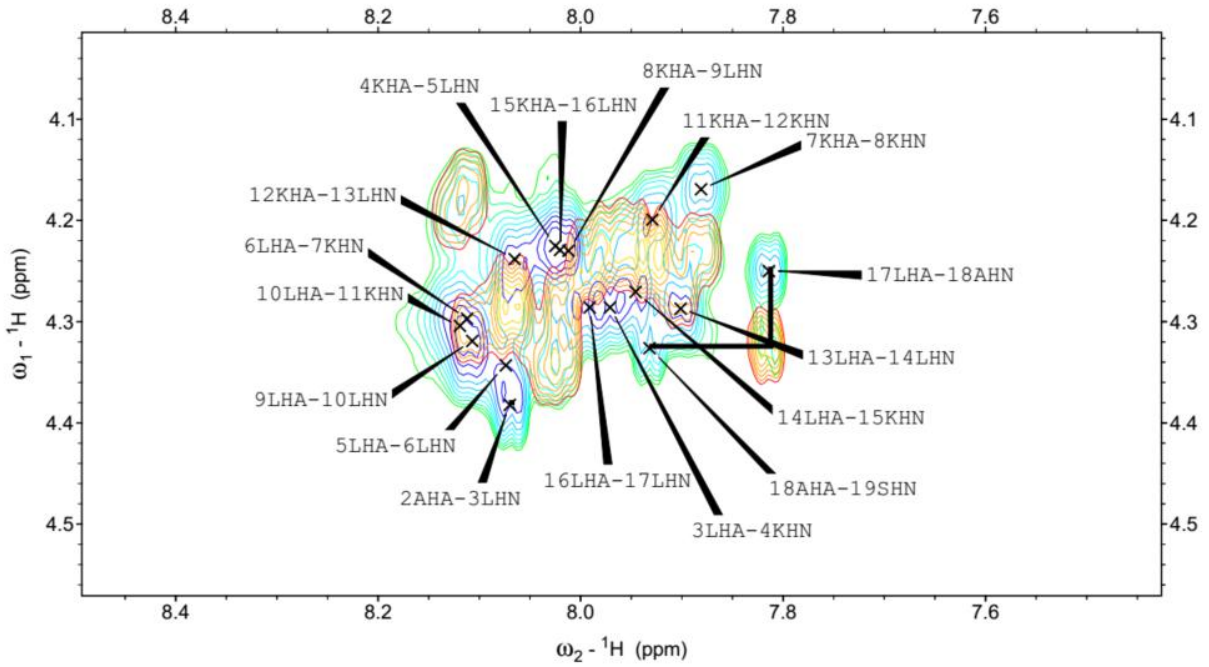

TOCSY-NOESY walk: residue 18.

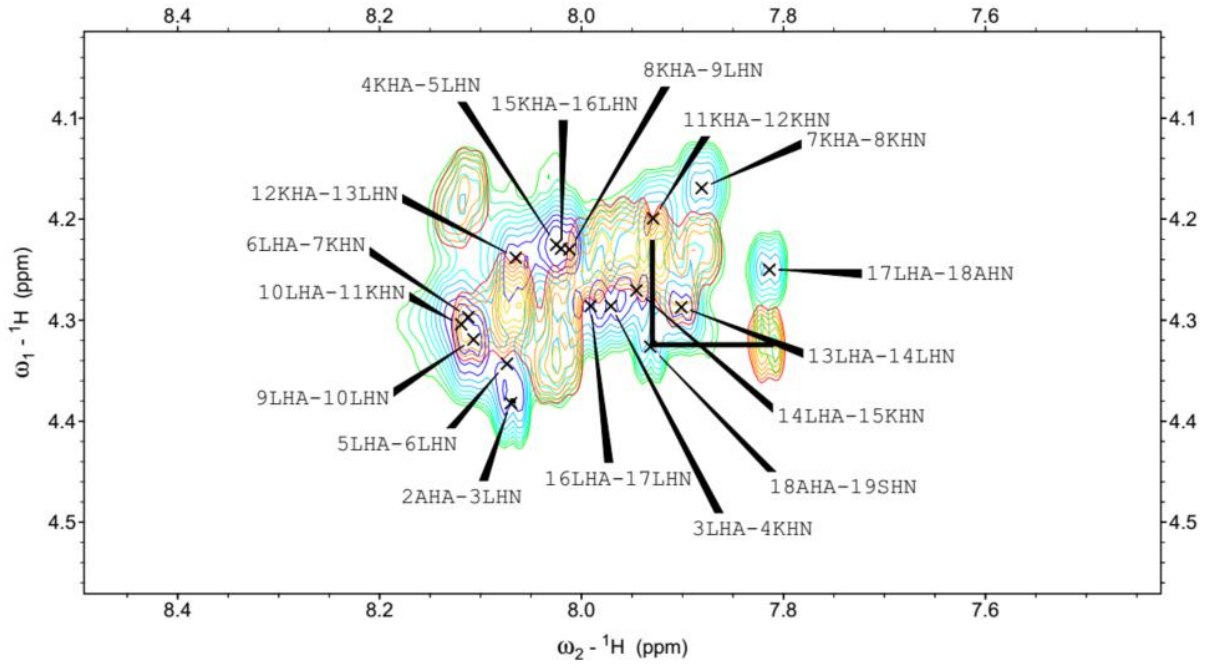

TOCSY-NOESY walk: residue 18-19.

Appendix B - Peptide structures generated by CNS

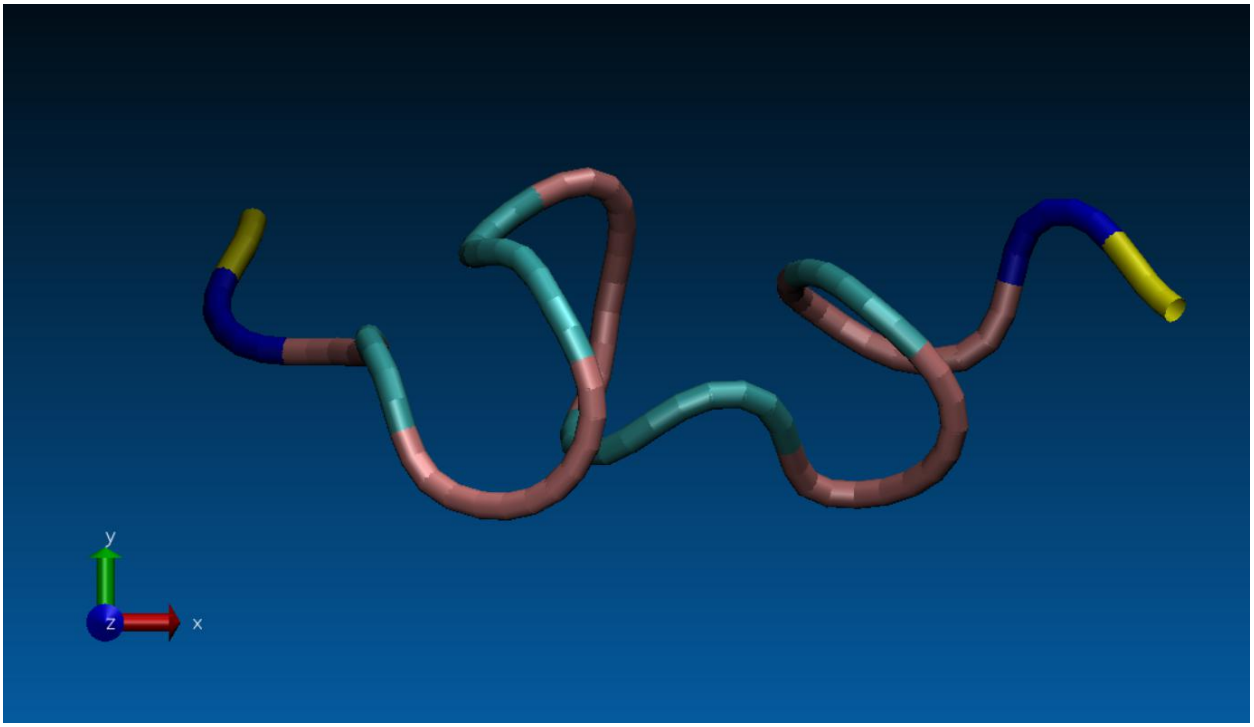

Structure 1

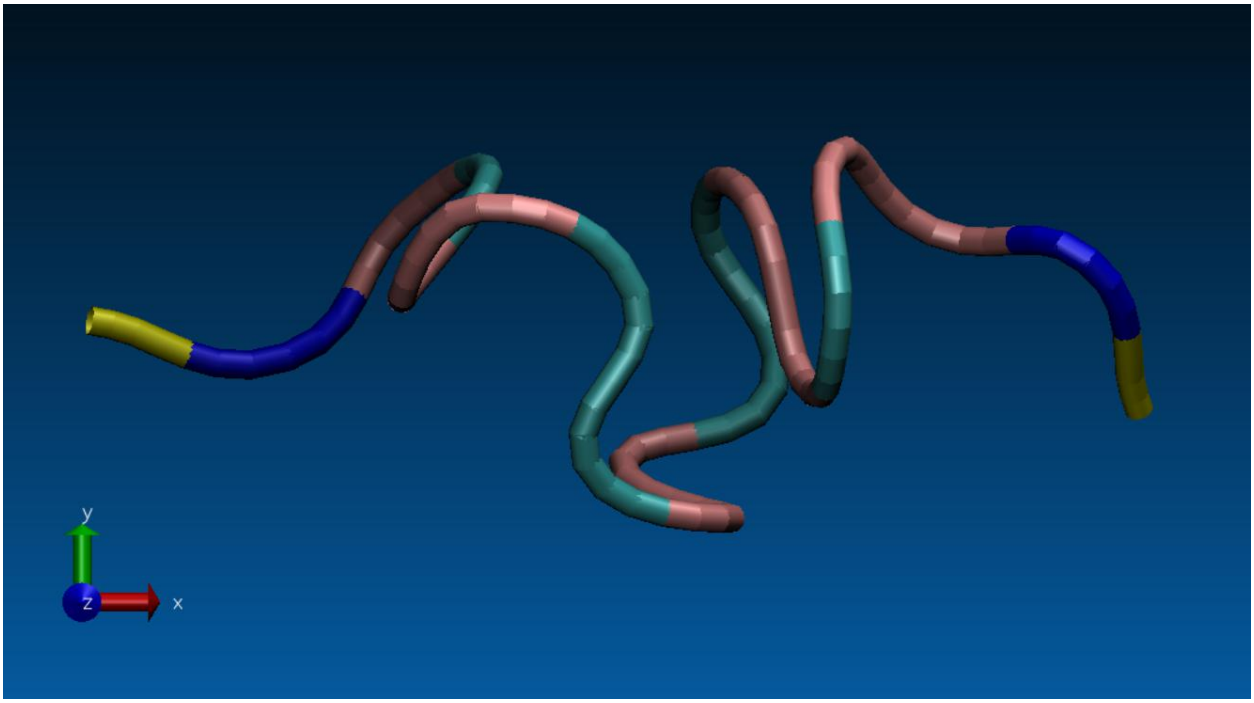

Structure 2

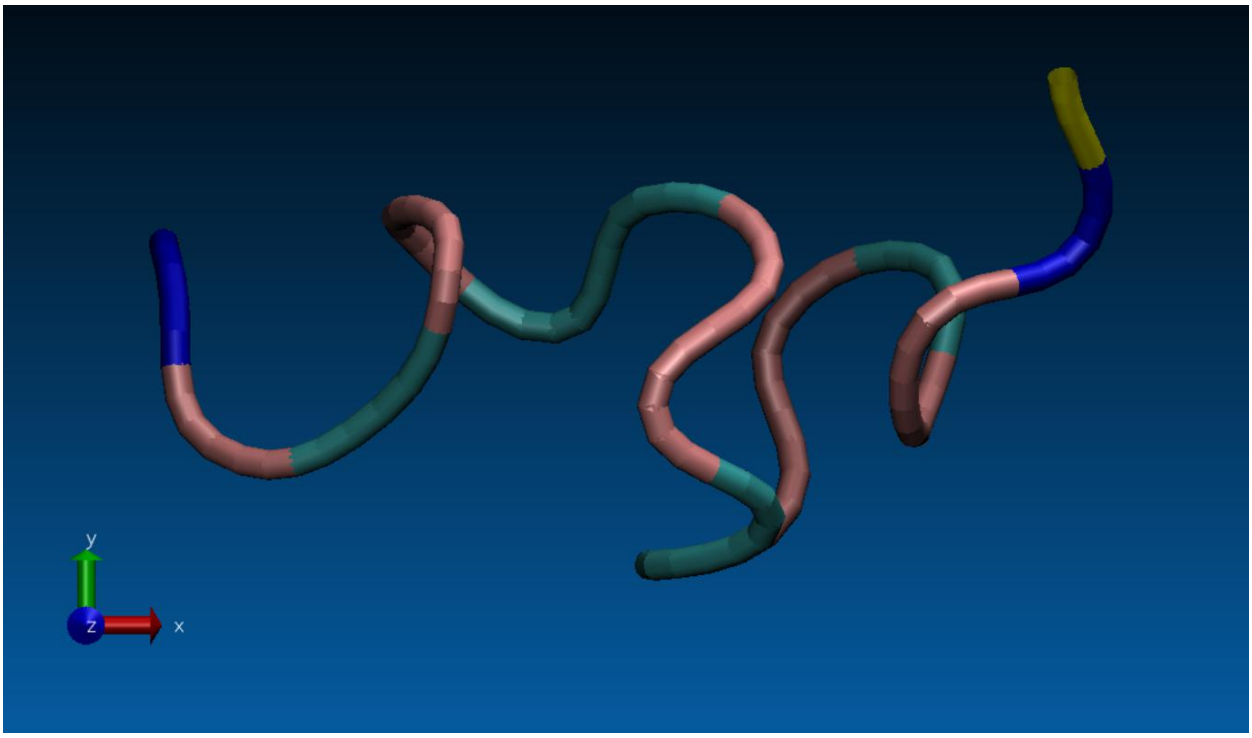

Structure 3

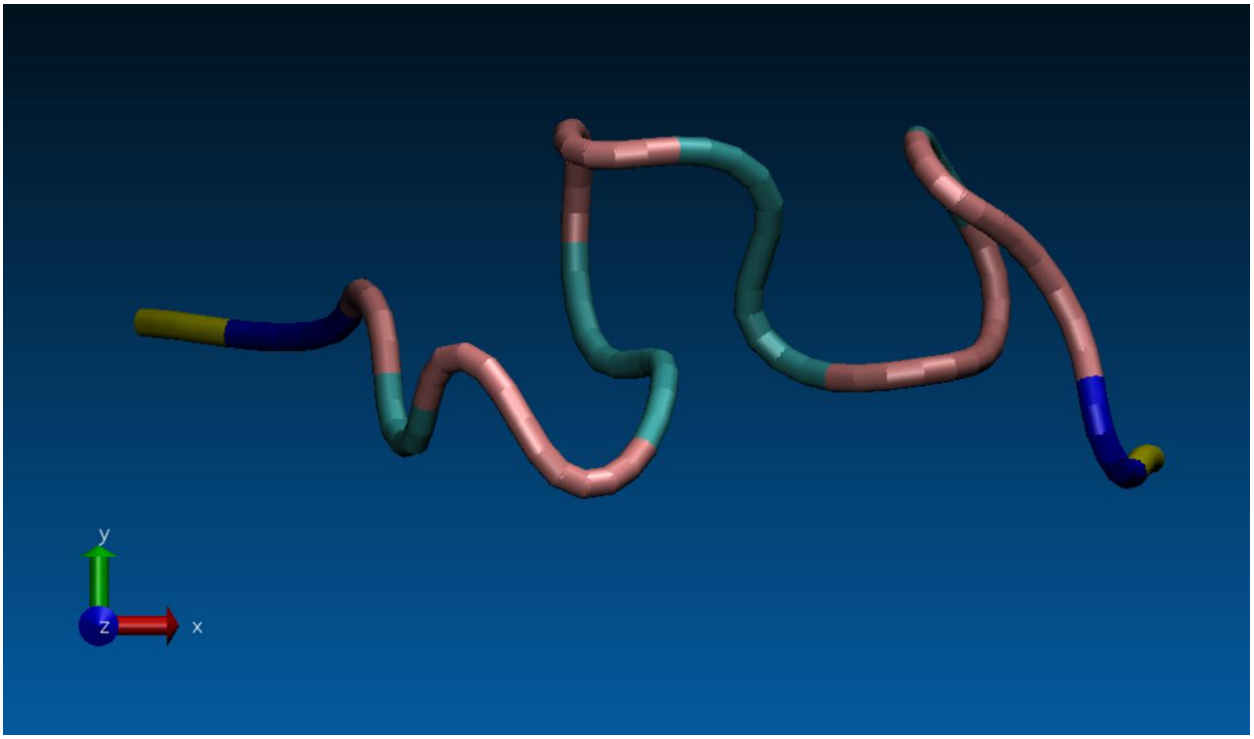

Structure 4

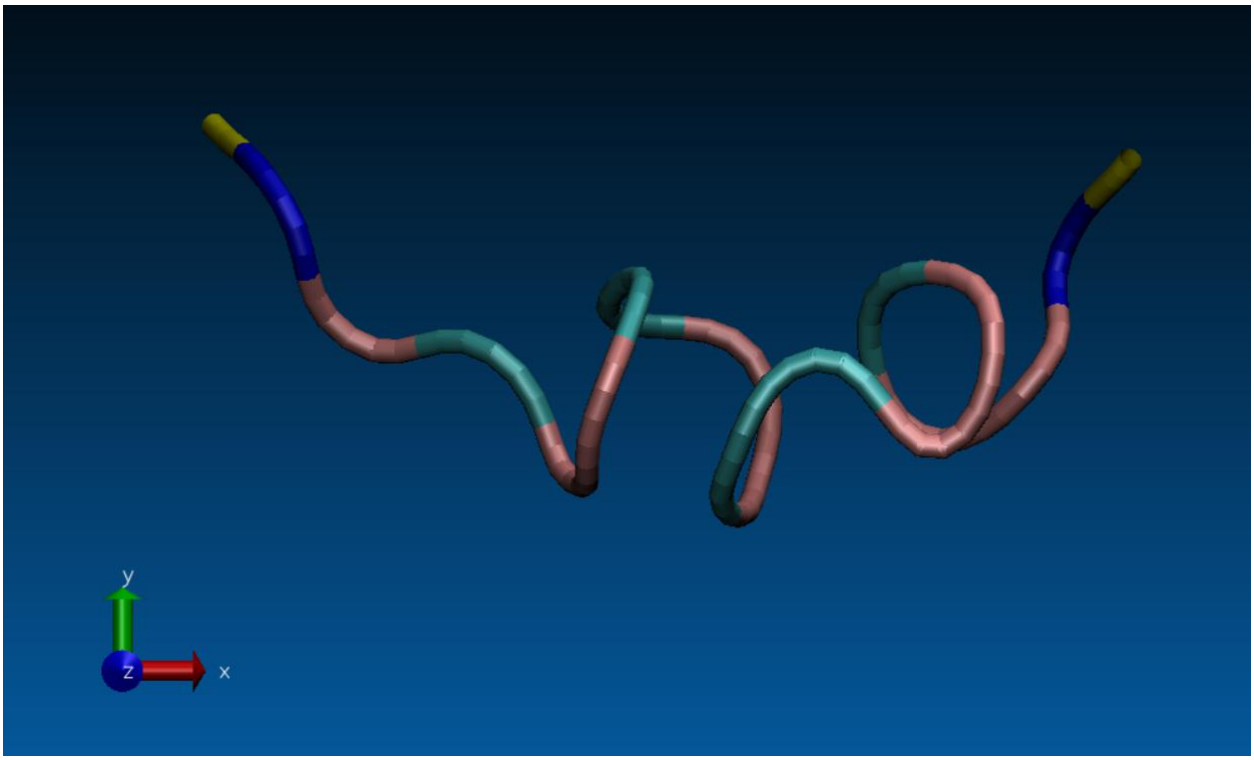

Structure 5

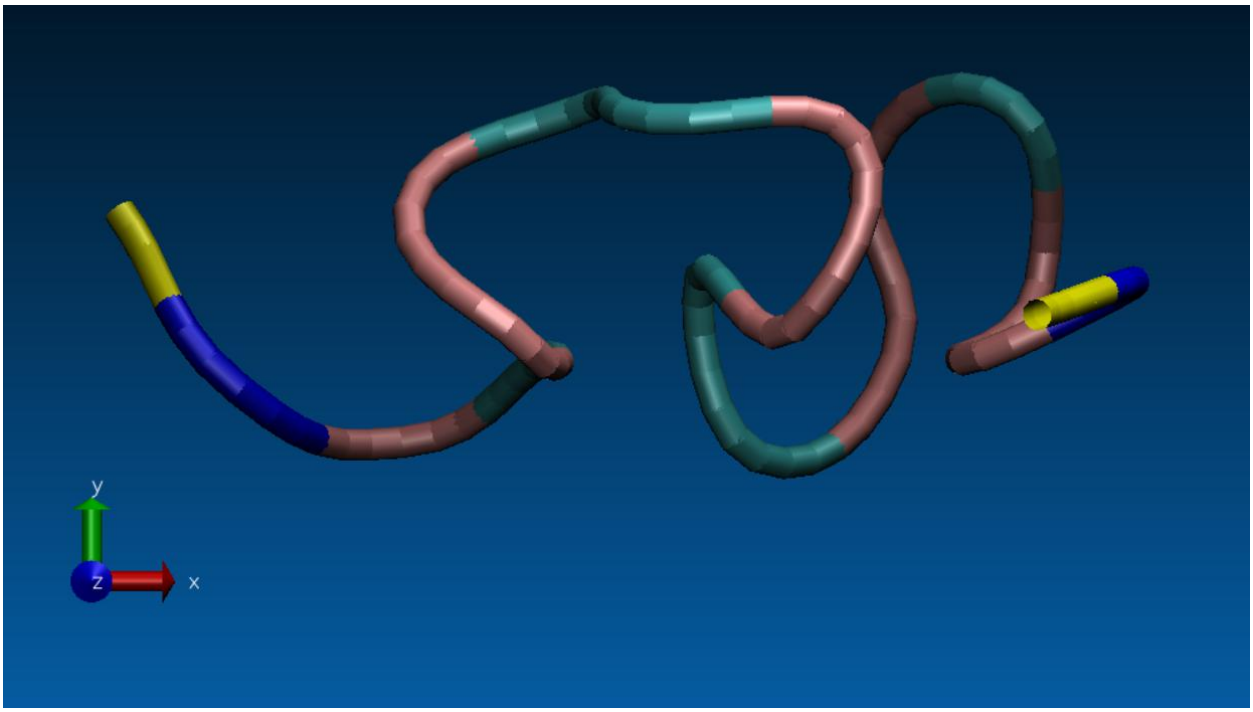

Structure 6

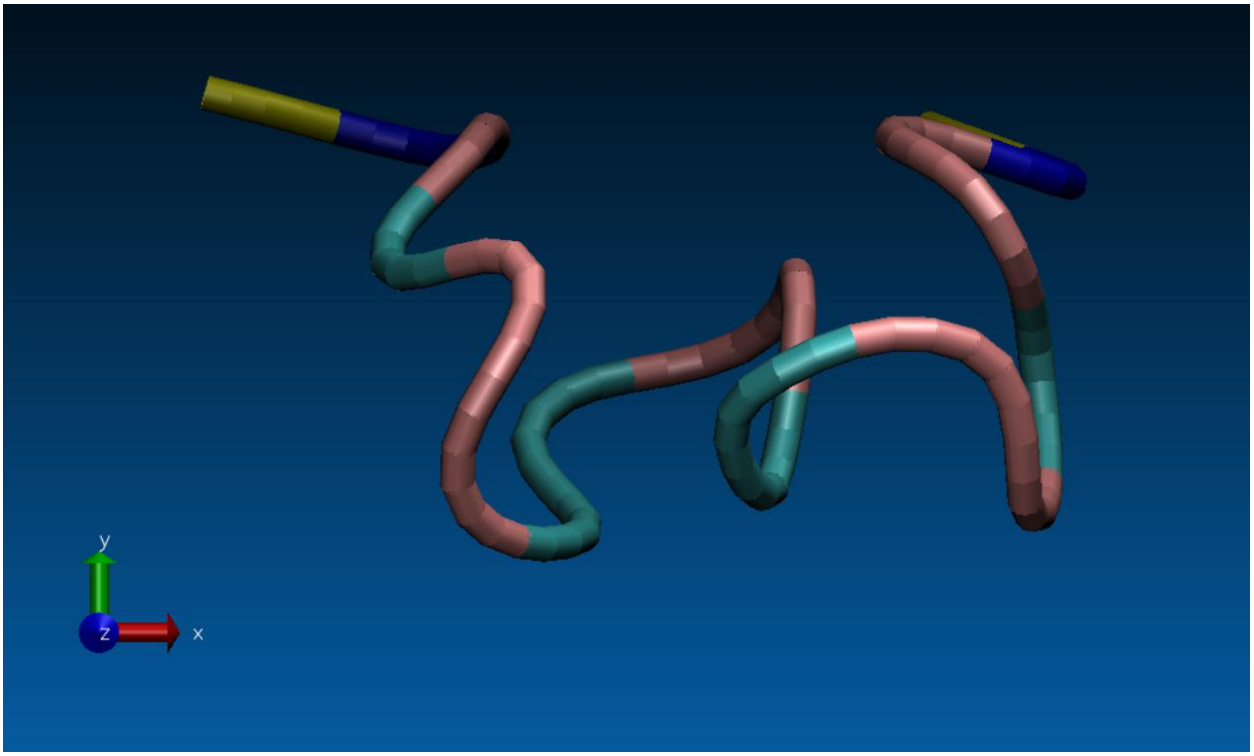

Structure 7

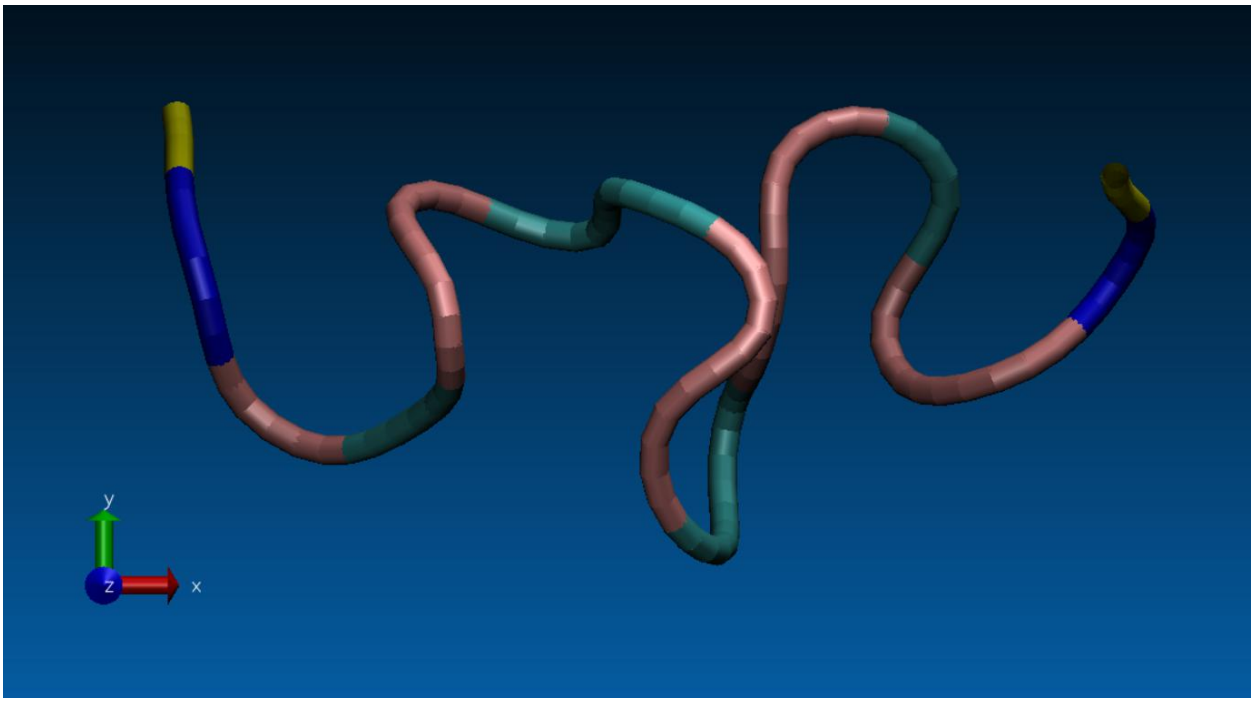

Structure 8

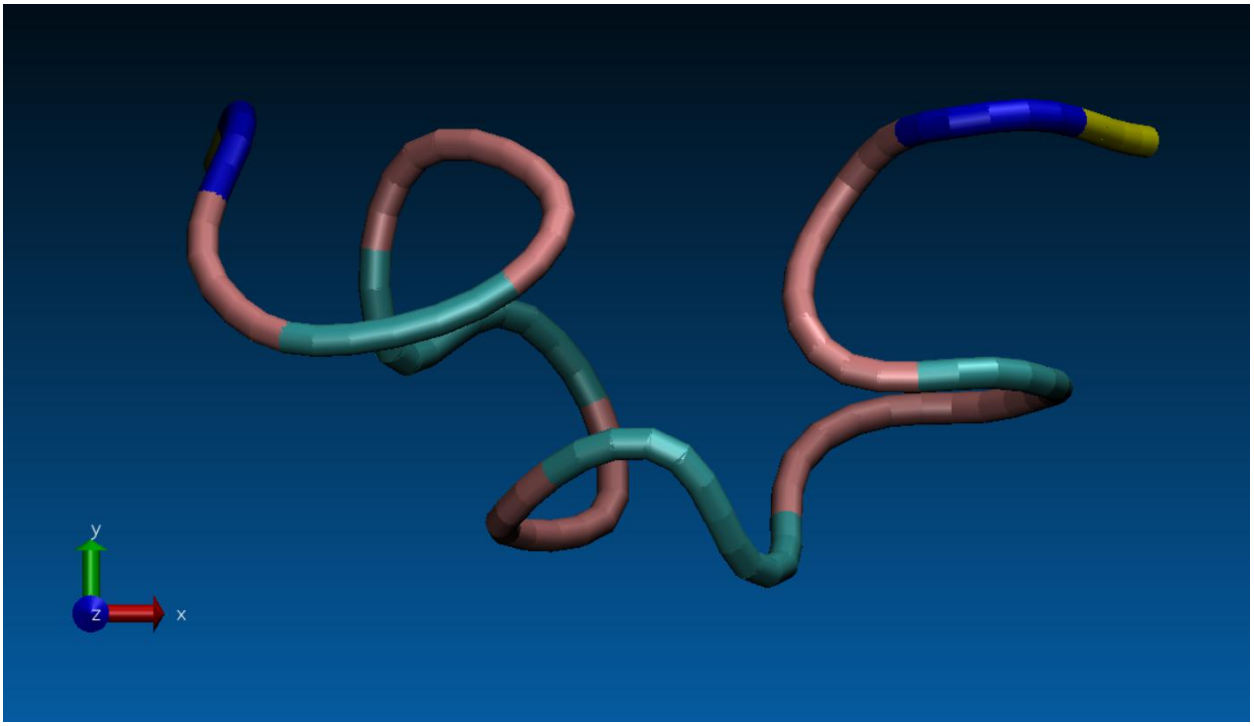

Structure 9

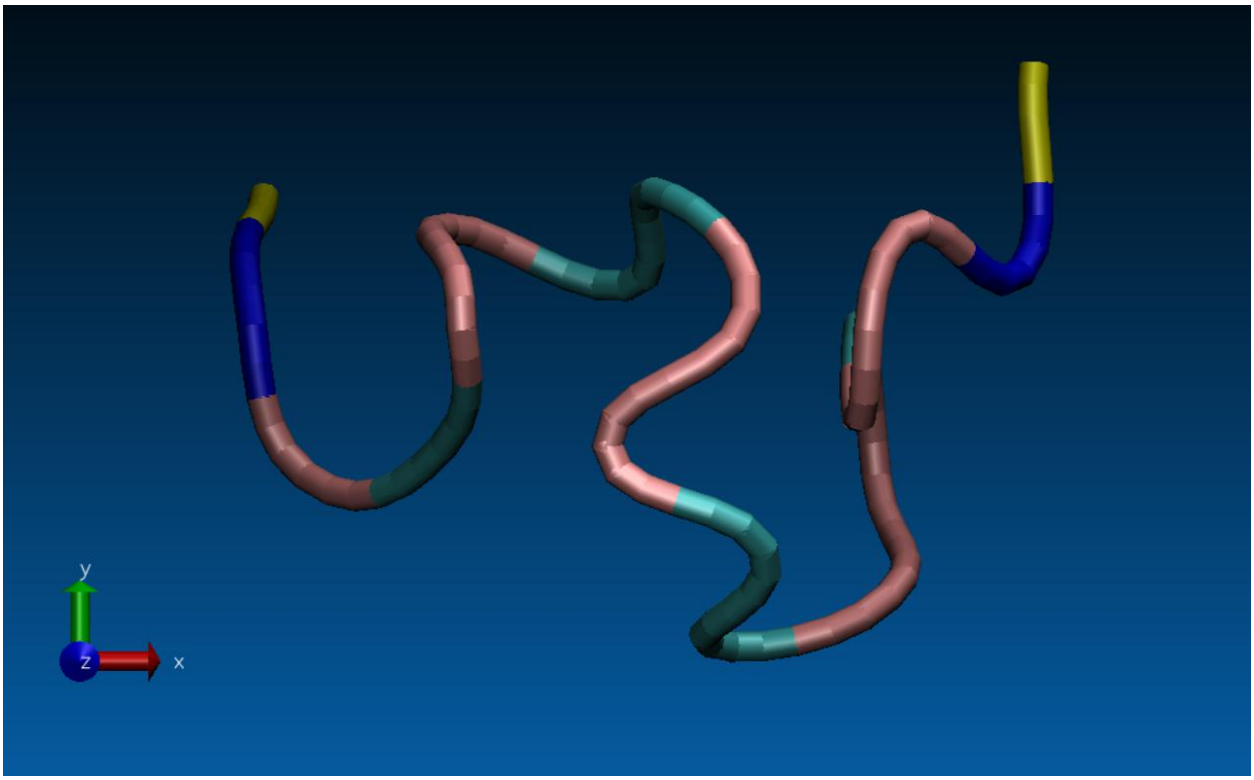

Structure 10